CONTROLLING PROPAGATION PROPERTIES OF SURFACE PLASMON POLARITON AT TERAHERTZ FREQUENCY

by

Barun Gupta

A dissertation submitted to the faculty of
The University of Utah
in partial fulfillment of the requirements for the degree of

Doctor of Philosophy

Department of Electrical and Computer Engineering

The University of Utah

May 2017

The University of Utah Graduate School

STATEMENT OF DISSERTATION APPROVAL

The dissertation of **Barun Gupta**

has been approved by the following supervisory committee members:

Ajay Nahata	Chair	**12/16/2016** Date Approved
Michael Bartl	Member	**02/02/2017** Date Approved
David Schurig	Member	**12/16/2016** Date Approved
Michael Scarpulla	Member	**02/22/2017** Date Approved
Sivaraman Guruswamy	Member	**12/16/2016** Date Approved

and by **Gianluca Lazzi**, Chair/Dean

of the Department/College/School of **Electrical and Computer Engineering**

and by David B. Kieda, Dean of The Graduate School.

ABSTRACT

Despite great scientific exploration since the 1900s, the terahertz range is one of the least explored regions of electromagnetic spectrum today. In the field of plasmonics, texturing and patterning allows for control over electromagnetic waves bound to the interface between a metal and the adjacent dielectric medium. The surface plasmon-polaritons (SPPs) display unique dispersion characteristics that depend upon the plasma frequency of the medium. In the long wavelength regime, where metals are highly conductive, such texturing can create an effective medium that can be characterized by an effective plasma frequency that is determined by the geometrical parameters of the surface structure. The terahertz (THz) spectral range offers unique opportunities to utilize such materials.

This thesis describes a number of terahertz plasmonic devices, both passive and active, fabricated using different techniques. As an example, inkjet printing is exploited for fabricating two-dimensional plasmonic devices. In this case, we demonstrated the terahertz plasmonic structures in which the conductivity of the metallic film is varied spatially in order to further control the plasmonic response. Using a commercially available inkjet printers, in which one cartridge is filled with conductive silver ink and a second cartridge is filled with resistive carbon ink, computer generated drawings of plasmonic structures are printed in which the individual printed dots can have differing amounts of the two inks, thereby creating a spatial variation in the conductivity. The

inkjet printing technique is limited to the two-dimensional structurers. In order to expand the capability of printing complex terahertz devices, which cannot otherwise be fabricated using standard fabricating techniques, we employed 3D printing techniques. 3D printing techniques using polymers to print out the complex structures.

In the realm of active plasmonic devices, a wide range of innovative approaches have been developed utilizing a variety of materials. We discuss the use of SMAs for terahertz (THz) plasmonics that allows for switching between different physical geometries corresponding to different electromagnetic responses.

TABLE OF CONTENTS

ACKNOWLEDGEMENTS

First, I would like to express my deepest gratitude to my advisor Prof. Ajay Nahata for his invaluable guidance, support and encouragement throughout the last four years. I have been very fortunate to have Dr. Nahata as a research supervisor who gave me the freedom to explore on my own, and at the same time kept me on research track when my steps faltered. During the last four years, I went through many downfalls, but he was there to keep me motivated. His patience and support helped me overcome the toughest phase of my life. He never ceased himself and was always available to provide directions and his thoughts on the projects of which I have been a part. Besides being a wonderful researcher, he is an excellent teacher. I have taken “Laser and Application”, “Ultrafast Optics” and “Nonlinear Optics” classes from him. I can without doubt say that those were the best classes I have ever taken. He not only cares about the progress in PhD research but he helps us prepare well for our future careers.

Prof. Sivaraman Guruswamy was very helpful and supportive on the projects of which I have been part. Without his discussions, I wouldn’t have been able to complete the inkjet printing project. He provided very insightful thoughts on the shape memory alloy which allowed me to complete the shape memory alloy project successfully and as a result, this project was published in one of the most reputable journals "Advanced Optical Materials". Professor Guruswamy was available to help us with discussion and he let us borrow the electromagnet whenever we needed it. I appreciate him from the

bottom of my heart.

Prof. Michael provided insightful comments and discussion on the magneto-optics project. He provided us with the ferromagnetic ink which was compatible with the silver ink. He provided us insightful comments and discussions with him on the magneto-optics project that were very helpful for understanding the project. Without his insightful discussion, I would not have been able to complete this project.

Prof. David Schurig is the one of the best teachers in my life. His vast knowledge in the field of physics is quite remarkable. He provided us tremendous insight into various projects, including the negative index project. His passion and dedication has served as a great motivation for me to learn and critically analyze physics. Besides being a great teacher and researcher, he is very athletic. I have been very inspired by him. It was due to his inspiration that I was able to complete a half marathon and learn to swim. I always wish I could be even ten percent as athletic as he is. He is a true inspiration for me as a researcher and as an athletic person.

Prof. Michael Scharpulla's insightful comments and constructive criticisms at different stages of my research were thought provoking and helped me focus on the project and explain the results clearly. I am so grateful to him for holding me to a high research standard and enforcing the strict validations for each research result, thus teaching me how to do systematic research.

I would like to thank my labmate and my dearest friend, Shashank Pandey, whose discussions on the various projects and his continuous motivation helped me to finish my dissertation. He is the one man who stood behind me in the most difficult time of my life. I greatly value his friendship and he is the one due to whom I was able

to finish my PhD in a joyful way. More importantly, none of this would have been possible without the support of my family, especially my elder brother, Arun Rauniyar.

It would be unfair on my part if I forget to mention and thank my friends, Namrata Handlon, Ashish Lamsal, Dr. Parsuram Budhathoki, Dr. Siddarth Kumar and Dr. Pankaj Kumar who constantly encouraged me to stay focused during the most difficult time of my life.

Finally, I would like to appreciate the financial support from MRSEC to finish my research projects.

CHAPTER 1

INTRODUCTION

1.1 Terahertz Technology

The terahertz (THz) range spans from 0.1 THz (wavelength = 3 mm) to 10 THz (wavelength = 0.03 mm) and lies in between the microwave and infrared frequency regions, as shown in Figure 1.1. Because terahertz radiation lies in between 30 ≒ m and 3 mm, it is also referred to as submillimeter wavelength radiation. Like infrared and microwave radiation, terahertz radiation is non-ionizing and can pass through a wide variety of dielectrics such as clothing, paper, cardboard, wood, plastic and ceramics. The penetration depth is typically less than that of the microwave radiation. Terahertz radiation has limited penetration through fog and clouds and cannot penetrate liquid water and metals. The THz frequency remained unexplored for many years due to the lack of practical sources and detectors. The THz frequency range is also commonly referred to as the "gap in the electromagnetic spectrum" due to the limited availability of coherent THz sources and detectors [1-3]. This is because it is too high in frequency for conventional electronics and too low in frequency for conventional optics. Nevertheless, since the 1970s, advancements in the fields of microwave and infrared have led us to new materials and devices that empowered an accelerated progress in the field of THz and started closing the THz gap. Based on these technical advances, a

number of practical THz sources and detectors currently exist. However, more research has to be done in order to create more compact and more efficient portable THz sources and detectors [3]. There are a number of attractive features of THz waves that can be summarized as follows [4-6]-

(a) Fingerprinting: Rotation and vibrational modes of many molecules, especially long-chain organic molecules, lie within the terahertz spectral range. The specific location and amplitude of these absorption peaks can be used to identify the molecules.

(b) Transparency and resolution: Most non-metallic materials or dielectrics are at least partially transparent to THz radiation, including dielectrics such as plastic, paper, cardboard, textiles and ceramics. This property of THz waves is extremely useful for inspecting samples that are hidden or inside non-optically-transparent containers. Dielectrics are also transparent to microwave radiation, but the larger wavelength compared to THz waves degrades the resolution in imaging applications. Infrared radiation has much better resolution than THz waves but is often opaque to dielectrics such as clothes, woods, papers, and plastics and thus cannot be used to image hidden objects.

(c) Safety: X-ray is extensively used in inspecting bone fractures and in airports for detecting weapons or prohibited items such as guns, illegal drugs, sharp objects, etc. Since X-rays are ionizing, repeated exposure can cause cancer and damage issues and cells. THz radiation is low-energy non-ionizing radiation that can provide an alternative technology, both for detecting bone fractures and for use in airport scanners. Nevertheless, x-ray provides much better spatial

resolution than THz radiation.

An enduring research direction in the THz community involved the generation of broadband THz radiation. There are a number of ways for generating coherent THz. Two of the most popular techniques used for generating THz radiation involve a photoconductive antenna and nonlinear mixing, and both techniques rely on a high power ultrafast laser.

A photoconductive antenna (PCA) consists of two gold electrodes that are fabricated onto a semiconducting substrate, as shown in Figure 1.2. A variety of different semiconductor materials have been examined for this application over the last several decades. Based on these studies, low-temperature grown GaAs has become the medium of choice because of its short carrier recombination lifetime, reasonably high mobility and high surface breakdown voltage. When a bias voltage is applied between the two electrodes, photo-generated charge carriers can be rapidly accelerated, which provides the basic physical mechanism for generating THz radiation.

Using pulses lasers, the amplitude of the generated current generally follows the temporal properties of the optical excitation. The generated THz pulse corresponds to the temporal derivative of the current pulse. The polarization of the generated THz radiation is parallel to the applied bias field, which is perpendicular to the gap between the two electrodes. The incident photon energy of the laser pulse must have greater energy than the bandgap of the low-temperature grown GaAs substrate. The amplitude of the generated THz field can be given by

$$E_{THz} = \frac{Ae}{4\pi\varepsilon_0 c^2 z} \frac{\delta N(t)}{\delta t} \mu E_b \qquad (1)$$

where A is the area of illumination, ε_o is the permittivity in vacuum, c is the speed of

light, e is the electron charge, z is the penetration of the laser pulse into the semiconductor, μ is the mobility of the carriers, E_b is the bias field and N the density of photo-carriers. The majority of the current contribution comes from electrons [7-9].

The other popular method for generating THz radiation is via optical rectification in a nonlinear crystal, as shown in Figure 1.3.

Optical rectification is a second-order nonlinear optical effect in which THz waves are generated by a difference-frequency mixing process between the different frequency components of the incident femtosecond laser pulse.

Difference frequency generation (DFG) occurs in a material with sufficiently high second-order susceptibilities. Mathematically, the polarization induced by the electric field in a nonlinear medium can be expressed as a power series:

$$P_2{}^{NL} = (\chi_1 + \chi_2 E + \chi_3 E^2 + \cdots) E \qquad (2)$$

If we consider the applied electric fields are $E_1=E_0 \cos(\omega_1 t)$ and $E_1=E_0 \cos(\omega_2 t)$, then the second-order polarization can be expressed as

$$P_2{}^{NL}(t) = \chi_2 E_1 E_2 = \chi_2 \frac{E_0{}^2}{2} [\cos(\omega_1 - \omega_2) t + \cos(\omega_1 + \omega_2) t] \qquad (3)$$

The generation of the THz radiation by optical radiation relies on difference frequency generation and is described by the first term of Eq. (3). The radiated electric field caused by the electro-optic-induced polarization is proportional to the second derivative with respect to the time.

$$E_{THz} = \frac{\delta^2 P_2{}^{NL}(t)}{\delta t^2} \qquad (4)$$

For a given material, the radiation efficiency and bandwidth of the generated THz radiation are affected by a number of factors, including crystal thickness, pulse

duration, absorption and dispersion, crystal orientation and phase matching [10-12].

1.2 Theory: Surface Plasmon Polaritons

This chapter provides a mathematical description of surface plasmon polaritons (SPPs). Surface plasmon polaritons were first observed by Wood in 1902 when he shined p-polarized light onto the metal-backed diffraction grating, and he observed bright and dark bands in the reflected light [13-14]. Since then, fundamental research and development based on SPP structures and devices has received tremendous interest due to their unique properties in controlling propagation properties of light coupled at the interface between metal and dielectrics. In recent years, SPPs are utilized for application in optics, surface-enhanced Raman spectroscopy (SERS), data storage, solar cells, biosensors and near-field imaging with a high lateral resolution of ($\lambda/200$) [15-16].

1.2.1 Surface Plasmon Polaritons (SPPs)

SPPs are the coherent oscillations of electrons (surface electromagnetic waves) that propagate along the interface between a metal and a dielectric material. Consider a TM wave (also called p-polarized wave) that is incident on the interface between a metal a dielectric at an angle of incident θ_1, as shown in Figure 1.4. The incident wave has a wavelength of λ, so the momentum of the incident photon is $k_d = 2\pi n_d/\lambda$, where n_d is the refractive index of the dielectric. The reflected wave propagates with the angle θ_1 while the the refracted wave travels inside the metal with an angle θ_2.

The momentum of the refracted photon is $k_m = 2\pi n_m/\lambda$, where n_m is the refractive index of the metal. The boundary matching condition along the x-axis is $k_{dx} = k_{mx}$. From

Snell's Law, we have $n_d \sin\theta_1 = n_m \sin\theta_2$. Since $n_d > n_m$, $\theta_2 > \theta_1$. The maximum value of θ_2 can be 90^0 at a certain value of θ_1. If we further increase the angle θ_1, the wave cannot propagate through metal beyond this limiting angle of incidence θ_1 and is reflected back into the dielectric. This limiting angle of incidence, also called the critical angle, is given by

$$sin\theta_c = \frac{n_m}{n_d}$$

With the TM- polarized incident radiation, the oscillations of the charges occur at the interface between the metal and the dielectric surface. Beyond the critical angle, although the wave is totally reflected back into the dielectric medium, there are oscillating charges that have associated radiation fields penetrating into the metal.

These penetrating fields are spatially decaying fields called evanescent fields and are normal to the interface, as shown in Figure 1.5. In order to couple the incident wave into the SPPs, the evanescent waves play a crucial role. At the interface, the horizontal component of the electric field E_x is continuous, whereas it is not the case for the E_z field. Along the z direction, the electric displacement D_z is continuous. Applying the boundary condition that D_z is continuous across the interface, $D_z = \varepsilon_d\varepsilon_0 E_{zd} = \varepsilon_m\varepsilon_0 E_{zm}$, where ε_d and ε_m are the relative permittivities of the dielectric and the metal, and ε_0 is the permittivity of the free space. There is discontinuity in the electric field along z direction E_z. This discontinuity results in time-dependent polarization change at the interface. From this, it is also evident that an s- polarized (TE) wave will not create oscillation of charges at the interface between metal and the dielectric. If the x–y plane is the interface plane, for wave propagation in the x direction only, when $z > 0$, one has [17-18]

$$E_d = (E_{xd}, 0, E_{zd}) \exp(-k_{zd}z) \exp[i(k_x x - \omega t)] \quad (1)$$

$$H_d = (0, H_{yd}, 0) \exp(-k_{zd} z) \exp[i(k_x x - \omega t)], \quad (2)$$

when $z < 0$, one has

$$E_m = (E_{xm}, 0, E_{zm}) \exp(k_{zm} z) \exp[i(k_x x - \omega t)] \quad (3)$$

$$H_m = (0, H_{ym}, 0) \exp(k_{zm} z) \exp[i(k_x x - \omega t)]. \quad (4)$$

Using the Maxwell equation $\nabla \cdot E = 0$, the electric field components take the form

$$E_{zd} = i \frac{k_x}{kzd} E_{xd} \quad (5)$$

$$E_{zm} = -i \frac{k_x}{kzm} E_{xm} \quad (6)$$

The Maxwell- Faraday equation is

$$\nabla \times E = -\frac{1}{c} \frac{\partial H}{\partial t} \quad (7)$$

Applying Eq. (7) to Eqs. (1) and (2), we get

$$k_{zd} E_{xd} - i k_x E_{zd} = i k H_{yd} \quad (8)$$

where $k = \omega/c$ is the wavevector in free space.

Similarly applying Eq. (7) to Eqs. (3) and (4), we get

$$k_{zm} E_{xm} - i k_x E_{zm} = i k H_{ym} \quad (9)$$

Using simple algebra, we can obtain following Eqs. from Eqs. (5), (6), (8) and (9)

$$\varepsilon_d k E_{xd} = i k_{zd} H_{yd} \quad (10)$$

$$\varepsilon_m k E_{xm} = -i k_{zm} H_{ym} \quad (11)$$

where $$k_{zd}^2 = k_x^2 - \varepsilon_d k^2 \quad (12)$$

$$k_{zm}^2 = k_x^2 - \varepsilon_m k^2 \quad (13)$$

The tangential components of E and H are continuous at the interface $z = 0$. This means

$$E_{xd} = E_{xm} \text{ and } H_{yd} = H_{ym}$$

Using these two relations, we can deduce from Eqs. (10) and (11)

$$\frac{k_{zd}}{k_{zm}} = -\frac{\varepsilon_d}{\varepsilon_m} \tag{14}$$

Using Eqs. (12), (13) and (14), we can easily deduce the following expression

$$k_x = k\sqrt{\frac{\varepsilon_d\,\varepsilon_m}{\varepsilon_d + \varepsilon_m}} \tag{15}$$

where k_x is basically the propagation vector along the interface. This is the surface plasmon wavevector. Therefore, we can write

$$k_{spp} = k\sqrt{\frac{\varepsilon_d\,\varepsilon_m}{\varepsilon_d + \varepsilon_m}} \tag{16}$$

This expression is valid for both real and complex values of ε_d and ε_m.

1.2.2 Dispersion Relation for SPPs

In Figure 1.6, we show the dispersion relation for the SPPs. It is evident that the momentum $\hbar k_{SPP}$ of the SPP is larger than the free space momentum $\hbar k$ which results in momentum mismatch between free space momentum and SPP momentum. In order to couple incident light into propagating surface plasmon, additional momentum has to be provided. The mismatch must be overcome by coupling light and SPP modes at the interface when

$$\varepsilon_d + \varepsilon_m = 0. \tag{17}$$

The dielectric constant of the metal at a certain frequency can be given by the Drude model

$$\varepsilon_m = 1 - \frac{{\omega_p}^2}{\omega^2} \tag{18}$$

where ω_p is the plasma frequency. For most of the metals, the plasma frequency lies in the ultraviolet range. Above the plasma frequency, the metal becomes dielectric. Using Eqs. (16)- (18), the surface plasmon polariton frequency can be expressed in terms of

plasma frequency as

$$\omega_{SPP} = \frac{\omega_p}{\sqrt{1+\varepsilon_d}} \tag{19}$$

As ε_d is always greater than 1, ω_{SPP} is always lower than the bulk plasma frequency. As SPPs propagate along the interface, the transverse components of the field are evanescent in nature and are spatially decaying into the metal and the dielectric. The penetration depth or the decay length of the electric field into the metal and the dielectric is given by $\delta_m = 1/k_{zm}$ and $\delta_d = 1/k_{zd}$. Using equations (12) and (13), the penetration depth in terms of permittivities can be expressed as

$$\delta_d = \frac{1}{k}\sqrt{\frac{\varepsilon_d + \varepsilon_m}{-\varepsilon_d{}^2}} \tag{20}$$

Similarly, the penetration depth into the metal is given by

$$\delta_m = \frac{1}{k}\sqrt{\frac{\varepsilon_d + \varepsilon_m}{-\varepsilon_m{}^2}} \tag{21}$$

Since ε_m is greater than ε_d, the penetration depth into the dielectric is greater than into the metal. The electric fields into the dielectric and the metal can be written as $E_d \propto \exp(-k_{zd}z)$ for $z > 0$, $E_m \propto \exp(k_{zm}z)$ for $z < 0$. It can be seen that the electric fields of SPP wave decay exponentially with distance $|z|$ from the interface. Based on the short penetration depths of the electric fields of SPP wave in the dielectric and the metal, the electric fields of SPP are concentrated mainly near the interface, and the field concentration is strongly enhanced at the interface. Nevertheless, the field concentration of SPP decays rapidly away from the interface along the z direction.

1.3 Extraordinary Optical Transmission

1.3.1 Transmission Through a Single Aperture

One of the simplest optical elements is a hole in a slab of metal. Bethe theoretically analyzed the diffraction of light through a small hole as a function of the wavelength, λ. Bethe assumed that the metal was an infinitely thin perfect electrical conductor, in which the hole diameter is much smaller than the wavelength of the incident light. With these idealized assumptions, he derived a mathematical description for the transmission efficiency, η, which is normalized to the aperture area [19, 20].

$$\eta = 4\,\frac{(kd)^4}{27\,\pi^4} = \frac{2^5}{3^3}\,\left(\frac{d}{\lambda}\right)^4 \qquad (22)$$

Here, $k = 2\pi/\lambda$ is the wavevector of the incident light having wavelength λ and d is the diameter of the hole. From Eq. (22), it is evident that the transmission efficiency η varies as $(d/\lambda)^4$. Thus, if the wavelength λ of the incident light is larger than the hole radius r, the transmission efficiency will decrease rapidly.

As the light passes through a single hole, as shown in Figure 1.7, it diffracts. The details of the diffraction process depend upon the polarization of the incident light, if the hole is not circular [19]. Bethe predicted that if the diffraction pattern is scanned along the incoming polarization, the intensity would be a constant like a spherical wave in a plane. However, if it is scanned along the perpendicular direction, the intensity would decrease with the increasing angle. The intensity dependence on the angle varies as $\cos^2\theta$, which is consistent with a dipole emission pattern. Bethe had assumed the idealized condition of infinitely thin metal film with high conductivity while deriving the transmission efficiency through a single hole. If a real hole aperture is taken into account, it has depth and therefore has waveguide properties. The transmission through such a

hole with real depth is very different from the propagation of light in empty space. The diameter of the hole or the lateral dimension of the waveguide defines the wavelength at which light can no longer propagate through the aperture.

This wavelength is known as the cutoff wavelength λ_c. If the incident light wavelength $\lambda > \lambda_{c,}$ the transmission is further attenuated exponentially, as shown in Figure 1.8. With the real metals, the cutoff wavelength cannot be sharply defined because one goes continuously from a propagative to evanescent regime as the wavelength increases.

1.3.2 Single Aperture Surrounded by Periodic Corrugations

The transmission spectrum through a single aperture can be greatly modified if the single hole aperture is surrounded by corrugations that are on the order of the wavelength [21-27]. These corrugations surrounding the hole aperture give rise to extraordinary transmission when compared to a single hole. Figure 1.9 shows a single aperture surrounded by periodic circular corrugations. The hole diameter is 300 nm and the periodicity is 650 nm. Here the periodic structures provide the necessary momentum matching conditions to couple the incident light into propagating SPPs. As each corrugation acts as a scattering medium, the electromagnetic field above the surface becomes intense and is finally transmitted through the hole at a well-defined wavelength.

The position of the resonance peak is mainly determined by the periodicity of the corrugations and the dielectric medium in which it is placed. The transmission efficiency in this case can be orders of magnitude greater than the predicated by classical Bethe theory. If the output surface of the single hole aperture is also surrounded with the

circular corrugation with the same periodicity and at the same locations, the transmitted beam is very narrow with the angle of divergence less than a few degrees, which is much smaller than that of the single aperture with corrugation on only one side [21, 28].

Figure 1.10 shows a single aperture flanked by a number of periodically spaced circular grooves, also referred to as a bullseye structure. The measured temporal waveforms corresponding to the transmitted THz pulses through 2, 4 and 6 groove patterns are shown in Fig. 1.10(c). For completeness, the temporal waveform for the reference bare aperture is shown at the bottom of Figure 1.10(c). As discussed above, each groove couples a fraction of the incident THz pulse to a surface wave that propagates both towards and away from the aperture.

In the present geometry, only surface waves that propagate towards the aperture contribute to the transmitted THz waveform. From Figure. 1.9(c), it is apparent that there are a number of low-amplitude oscillations following the primary oscillations. These secondary oscillations are believed to be caused by in-plane scattering from adjacent grooves. Since the linewidth of any transmission resonance associated with these bullseye structures is much narrower than the bandwidth of the incident or coupled THz pulses, we do not expect to observe any significant formation of standing wave patterns [29].

1.3.3 Enhanced Optical Transmission Through Periodic Hole Arrays

As discussed earlier, light cannot be directly coupled into surface plasmon modes on an unstructured metal film. This is because the momentum of incident free space radiation is smaller than the surface plasmon momentum. One way of coupling light into surface plasmon mode is by creating a periodic array of holes, as shown in Figure 1.11.

These arrays give rise to the enhanced optical transmission phenomenon [30]. The transmission spectrum contains multiple transmission resonances and, at the peak of the resonance, the transmission efficiency η is much larger than for a single aperture. The mechanism for this process can be understood by considering three processes - the coupling of incident light into SPPs by the periodic hole arrays, transmission through the holes to the second surface and then re-emission from the second surface. The necessary momentum matching condition in the case of a rectangular periodic hole array can be written as

$$k_{SPP} = k_x \pm i\, G_x \pm j\, G_y \qquad (23)$$

where $k_x = (2\pi/\lambda) \sin\theta$ is the component of the incident photon's wavevector in the plane of the grating, θ is the angle between propagation wavevector and the sample surface normal, and i and j are the integers and gives the different modes (both i and j cannot be zero simultaneously). Here, $G_x = \frac{2\pi}{a} and\ G_y = \frac{2\pi}{b}$ are the grating momentum wavevectors for the rectangular array, and a and b are the periodicities along x and y directions, respectively. For a square array, $G_x = G_y = \frac{2\pi}{a}$. If the angle of incidence θ is varied, the incident radiation excites different SPP modes. If the angle θ is not zero, the resonance peak is split into two components.

The resonance wavelength for the square array at normal incidence is given by

$$\nu_{Dip} = \frac{c}{a\sqrt{\varepsilon_d}} \sqrt{i^2 + j^2} \qquad (24)$$

where ν_{Dip} is the position of the resonance frequency, and ε_d is the permittivity of the dielectric. We have previously shown that it is the resonance dip on the higher frequency side that determines the location of the resonance given by Eq. (24) [31-33]. Periodic

hole arrays have many applications in optics, chemistry and biology [34-37].

Equation (24) clearly shows that the transmission resonances can be altered by simply changing the periodicity and the medium in which the hole array has been fabricated. As an example, Figure 1.12 shows that the hole array on the dimpled surface acts as a tunable filter because the wavelength selectivity of the array transmission can be adjusted by changing the period. The letter "hν" are obtained by fabricating a periodic array in which some of the dimples are milled through to film holes that, in turn, reveal the spectral signature of the array. The periodicity for the hole array with letter "h" is 550 nm while that for the letter "ν" is 450 nm.

1.4 Outlines

In the following chapters, I will discuss the integration of fundamentals and applications related to controlling the propagation properties of SPPs through various plasmonic structures. These structures are fabricated using a variety of different conventional and unconventional approaches.

In Chapter 2, we discuss device fabrication through an inkjet printing technique. Inkjet printing provides a simple approach for creating terahertz plasmonic devices with a spatial variation of conductivity. This method also provides for the ability to create complex plasmonic devices rapidly that are otherwise very challenging to achieve using standard microfabrication techniques. The one limitation of inkjet printing technique is that it can only be applied to two-dimensional structures. In addition to a discussion on the fabrication methodology, we discuss the characterization techniques, including terahertz imaging using CW and pulsed terahertz waves.

In Chapter 3, we discuss terahertz plasmonic structures that have a spatially varying conductivity. This spatial variation allows us to control and study the enhance plasmonic response. The spatial variation is achieved by using a commercially available inkjet printer, in which one cartridge is filled with conductive silver ink and a second cartridge is filled with resistive carbon ink. The spatial variations are designed using Adobe Illustrator and printed with an inkjet printer. In the printed structures, the individual printed dots can have differing amounts of the two inks, thereby creating a spatial variation of the conductivity. The silver ink has a DC conductivity that is only factors of six lower than bulk silver, while the carbon ink acts as a lossy dielectric. Both inks sinter at room temperature immediately after contact with the plastic film. Using a periodic array of subwavelength apertures as a test structure, patterns printed with fractional amounts of the two show dramatically different enhanced optical transmission properties. These differences arise from changes in the propagation loss properties as a function of conductivity. These data are used to design and fabricate aperture arrays in which the conductivity varies spatially. The resulting plasmonic effect is found to dramatically alter the spatial beam profile of the transmitted THz radiation, as measured by THz imaging.

In Chapter 4, we discuss the ability to create complex three-dimensional (3D) THz waveguide structures using 3D printing. Professional grade 3D printers are capable of printing a variety of plastics with a resolution of 600 dpi along the x- and y-axes and 1600 dpi along the z-axis. In the work presented here, we print devices using a Vero-White polymer, which we subsequently sputter coat with ~300 nm of Au. We have previously shown that when a metal layer of >150 nm is deposited on any substrate,

SPPs do not interact with the underlying substrate medium. Therefore, almost any underlying substrate medium can be used to create THz plasmonic devices.

In Chapter 5, we describe a family of symmetric and asymmetric T-shaped structures that act as a plasmonic THz waveguide and experimentally and numerically investigate the THz propagation properties of these devices. The waveguides were made using a commercially available professional grade 3D printer (Object EDEN 260V), which has a printing resolution of 600 dpi in the x-y plane and 1600 dpi along z-axis. We have recently shown that this approach allows for the fabrication of plasmonic devices with complex 3D shapes. The devices were printed using a polymer resin (Vero White) on a support platform. After the resin solidified, the devices were detached from the support and sputter deposited the device with Au. Sputter deposition typically allows for more film thicknesses on non-planar geometries. In order to help ensure the bottom surfaces of the T or inverted-L structures were coated with Au, we turned the samples multiple times between deposition runs. On the upper (planar) surfaces of the waveguide, the measured Au film thickness was ~500 nm. Once the deposited Au thickness is more than twice the skin depth, propagating SPP does not see the underlying substrate. Using THz time-domain spectroscopy, we measure the transmission spectrum and other guided-wave properties of the devices as a function of the structure height, lateral width, asymmetry and periodicity. We also perform numerical finite difference time-domain (FDTD) simulations to validate our observations.

In Chapter 6, we discuss the use of shape memory alloys for (THz) plasmonics. Nitinol, which is an alloy of nickel and titanium, has a DC conductivity that is similar to that of stainless steel. This level of conductivity is more than sufficient for THz

plasmonics applications, as we have previously shown in multiple publications. These materials are interesting because they allow for thermal switching between two different physical geometries using only moderate temperature changes. There are, of course, numerous examples of shape memory alloys in industrial applications. Overwhelmingly, these are based on shape memory alloy-based wires and involve one-way changes (a deformed alloy that reverts to its original shape upon heating only one time and does not return to another shape upon cooling). We use large (5 cm x 5 cm) foils that can be trained to thermally switch between a corrugated geometry (either a 1D corrugation or a 2D corrugation) simply by cycling the temperature over ~20° C range. This type of change is similar, in general terms, to the conductivity change that occurs with VO2 as the temperature is varied.

In Chapter 7, we discuss the first experimental observation of Anderson localization in the terahertz frequency range using plasmonic structures. This is accomplished using THz waveguides consisting of a one-dimensional array of rectangular apertures that are fabricated in a freestanding metal foil. Disorder is introduced into the waveguide by offsetting the position of each aperture spaced by 250 microns in a periodic waveguide; 10% disorder would correspond. We observe that for disorder levels below 25%, there was only an increase in the propagation loss along the device. However, for two specific waveguides with 25% disorder, we observe a spatially localized mode within the stopband of the device and exhibited a double-sided exponential spatial decay away from the maximum.

1.5 References

1. R. Köhler et al., “Terahertz semiconductor-heterostructure laser,” Nature, vol. 417, no. 6885, pp. 156–159, May 2002.

2. P. H. Siegel, “Terahertz technology,” IEEE Transactions on Microwave Theory and Techniques, vol. 50, no. 3, pp. 910–928, Mar. 2002.

3. B. Ferguson and X.-C. Zhang, “Materials for terahertz science and technology,” Nat Mater, vol. 1, no. 1, pp. 26–33, Sep. 2002.

4. Zomega Terahertz Corporation, “The Terahertz Wave Ebook”, Edition June 2012.

5. D.Mittleman, “Sensing with Terahertz Radiation”, ISBN 978-3-540-45601-8, Volume 85 2003.

6. A. Dobroiu, C. Otani, and K. Kawase, “Terahertz-wave sources and imaging applications,” Meas. Sci. Technol., vol. 17, no. 11, p. R161, 2006.

7. S. Kono, M. Tani, and K. Sakai, “Coherent detection of mid-infrared radiation up to 60 THz with an LT-GaAs photoconductive antenna,” IEE Proceedings - Optoelectronics, vol. 149, no. 3, pp. 105–109, Jun. 2002.

8. D. H. Auston , K. P. Cheung and P. R. Smith, “Picosecond photoconducting Hertzian dipoles”, Appl. Phys. Lett. 45, 284, Aug. 1984.

9. M. Tani, S. Matsuura, K. Sakai, and S. Nakashima, “Emission characteristics of photoconductive antennas based on low-temperature-grown GaAs and semi-insulating GaAs,” Appl. Opt., AO, vol. 36, no. 30, pp. 7853–7859, Oct. 1997.

10. A. Nahata, A.S. Weling and T.F. Heinz, “A wideband coherent terahertz spectroscopy system using optical rectification and electro-optic sampling”, Appl. Phys. Lett. 69, 2321-2323, Oct. 1996.

11. Zhang, X C, and Xu, J, "Introduction to THz wave photonics". Springer, New York, 2010.

12. Wu, Q., and X-C. Zhang. "Free-space electro-optic sampling of terahertz beams." Applied Physics Letters 67.24 (1995): 3523-3525, Dec. 1995.

13. R. W. Wood, “On a remarkable case of uneven distribution of light in a diffraction grating spectrum,” Proc. Phys. Soc. London, vol. 18, no. 1, p. 269, 1902.

14. R. W. Wood, "Diffraction gratings with controlled groove form and abnormal distribution of intensity". Philysophical magazine 23: 310-317; (1912).

15. W. L. Barnes, A. Dereux, and T. W. Ebbesen, “Surface plasmon subwavelength optics,” Nature, vol. 424, no. 6950, pp. 824–830, Aug. 2003.

16. M. Specht, J. D. Pedarnig, W. M. Heckl, and T. W. Hänsch, “Scanning plasmon near-field microscope,” Phys. Rev. Lett., vol. 68, no. 4, pp. 476–479, Jan. 1992.

17. U. Fano, “Atomic theory of electromagnetic interactions in dense materials,” Phys. Rev., vol. 103, no. 5, pp. 1202–1218, Sep. 1956.

18. U. Fano, “Atomic theory of electromagnetic interactions in dense materials,” Phys. Rev., vol. 103, no. 5, pp. 1202–1218, Sep. 1956.

19. H. A. Bethe, “Theory of diffraction by small holes,” Phys. Rev., vol. 66, no. 7–8, pp. 163–182, Oct. 1944.

20. C. Genet and T. W. Ebbesen, “Light in tiny holes,” Nature, vol. 445, no. 7123, pp. 39–46, Jan. 2007.

21. H. J. Lezec et al., “Beaming light from a subwavelength aperture,” Science, vol. 297, no. 5582, pp. 820–822, Aug. 2002.

22. T. Thio, K. M. Pellerin, R. A. Linke, H. J. Lezec, and T. W. Ebbesen, “Enhanced light transmission through a single subwavelength aperture,” Opt. Lett., OL, vol. 26, no. 24, pp. 1972–1974, Dec. 2001.

23. A. Degiron and T. W. Ebbesen, “Analysis of the transmission process through single apertures surrounded by periodic corrugations,” Opt. Express, OE, vol. 12, no. 16, pp. 3694–3700, Aug. 2004.

24. L. Martín-Moreno, F. J. García-Vidal, H. J. Lezec, A. Degiron, and T. W. Ebbesen, “Theory of highly directional emission from a single subwavelength aperture surrounded by surface corrugations,” Phys. Rev. Lett., vol. 90, no. 16, p. 167401, Apr. 2003.

25. F. J. García-Vidal, H. J. Lezec, T. W. Ebbesen, and L. Martín-Moreno, “Multiple paths to enhance optical transmission through a single subwavelength slit,” Phys. Rev. Lett., vol. 90, no. 21, p. 213901, May 2003.

26. G.Vidal, F. J., Martin-Moreno, L., Lezec, H. J. & Ebbesen, T. W. Focusing light with a single subwavelength aperture flanked by surface corrugations. Appl. Phys. Lett. 83, 4500–4502, Nov. 2003.

27. L.-B. Yu et al., “Physical origin of directional beaming emitted from a subwavelength slit,” Phys. Rev. B, vol. 71, no. 4, p. 041405, Jan. 2005.

28. C. Genet and T. W. Ebbesen, “Light in tiny holes,” Nature, vol. 445, no. 7123, pp. 39–46, Jan. 2007.

29. A. Agrawal, H. Cao, and A. Nahata, “Time-domain analysis of enhanced

transmission through a single subwavelength aperture," Opt. Express, OE, vol. 13, no. 9, pp. 3535–3542, May 2005.

30. T. W. Ebbesen, H. J. Lezec, H. F. Ghaemi, T. Thio, and P. A. Wolff, "Extraordinary optical transmission through sub-wavelength hole arrays," Nature, vol. 391, no. 6668, pp. 667–669, Feb. 1998.

31. S. Pandey, B. Gupta, and A. Nahata, "Terahertz plasmonic waveguides created via 3D printing," Opt. Express, vol. 21, no. 21, pp. 24422–24430, Oct. 2013.

32. B. Gupta, S. Pandey, and A. Nahata, "Plasmonic waveguides based on symmetric and asymmetric T-shaped structures," Opt. Express, vol. 22, no. 3, pp. 2868–2880, Feb. 2014.

33. B. Gupta, S. Pandey, S. Guruswamy, and A. Nahata, "Terahertz plasmonic structures based on spatially varying conductivities," Advanced Optical Materials, vol. 2, no. 6, pp. 565–571, Jun. 2014.

34. A. G. Brolo, R. Gordon, B. Leathem, and K. L. Kavanagh, "Surface plasmon sensor based on the enhanced light transmission through arrays of nanoholes in gold films," Langmuir, vol. 20, no. 12, pp. 4813–4815, Jun. 2004.

35. J. Henzie, J. Lee, M. H. Lee, W. Hasan, and T. W. Odom, "Nanofabrication of plasmonic structures," Annu Rev Phys Chem, vol. 60, pp. 147–165, 2009.

36. R. Gordon, A. G. Brolo, D. Sinton, and K. l. Kavanagh, "Resonant optical transmission through hole-arrays in metal films: physics and applications," Laser & Photon. Rev., vol. 4, no. 2, pp. 311–335, Feb. 2010.

37. B. Gupta, S. Pandey, A. Nahata, T. Zhang, and A. Nahata, "Bistable physical geometries for terahertz plasmonic structures using shape memory alloys," Advanced Optical Materials, Feb. 2017.

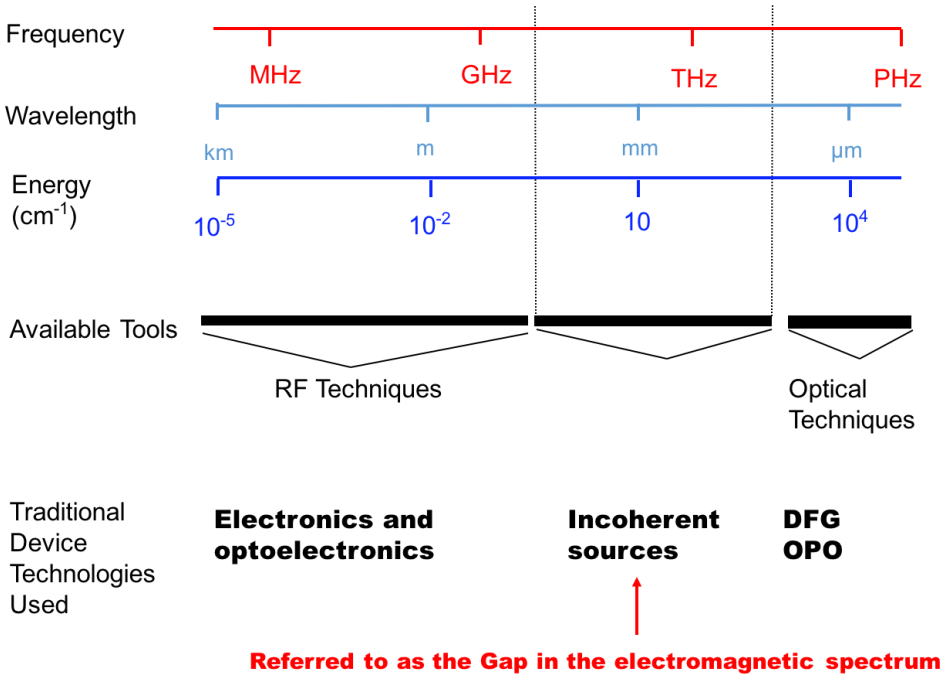

Figure 1.1: Terahertz electromagnetic spectrum

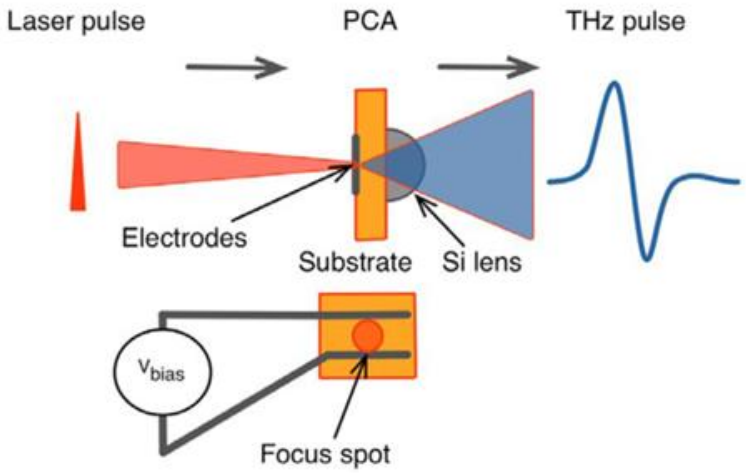

Figure 1.2. Photoconductive antenna for generating THz radiation.

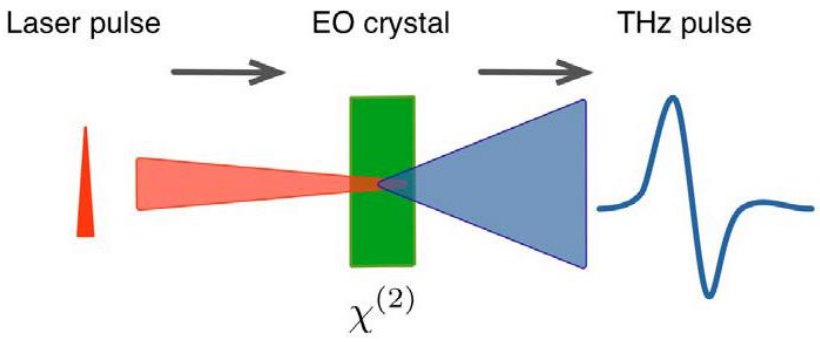

Figure 1.3. Optical rectification for generating THz radiation.

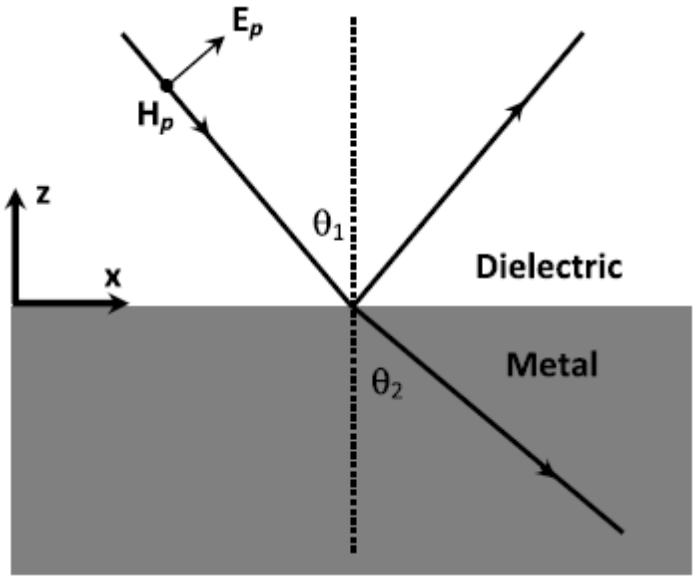

Figure 1.4: Schematic diagram of TM polarized wave incident upon a metal and dielectric interface.

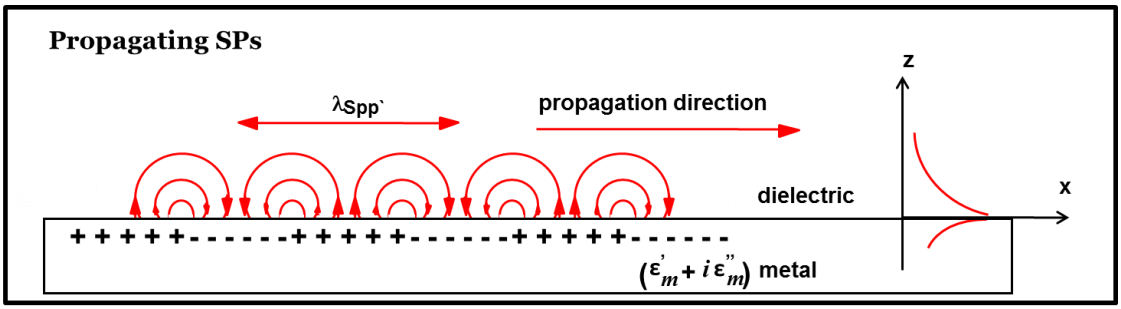

Figure 1.5: Schematic illustration of the electromagnetic wave and the surface charges at the interface between metal and dielectric for the TM polarized wave.

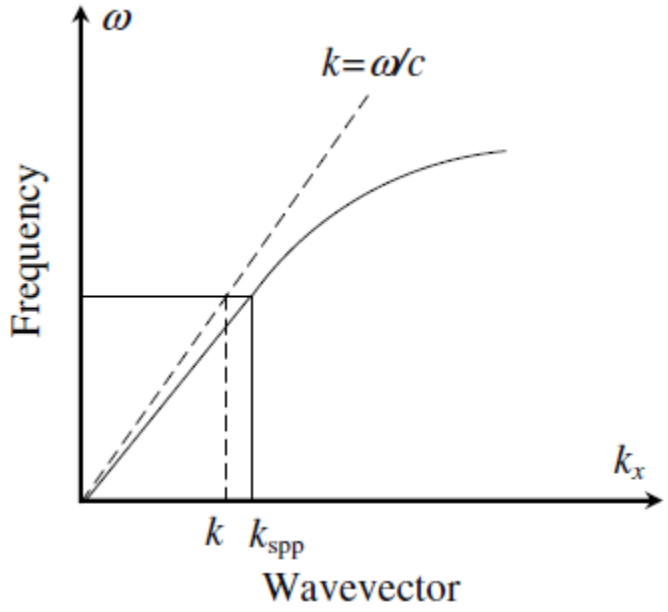

Figure 1.6: Dispersion curve of SPPs wave.

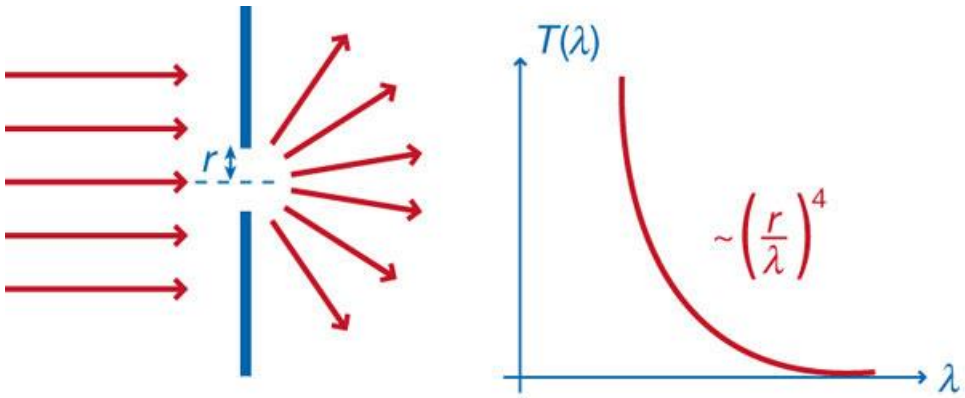

Figure 1.7: Diffraction through a single hole of radius r (Left). Transmission spectrum of light through a single hole on an infinitely thin metal film as a function of wavelength (Right).

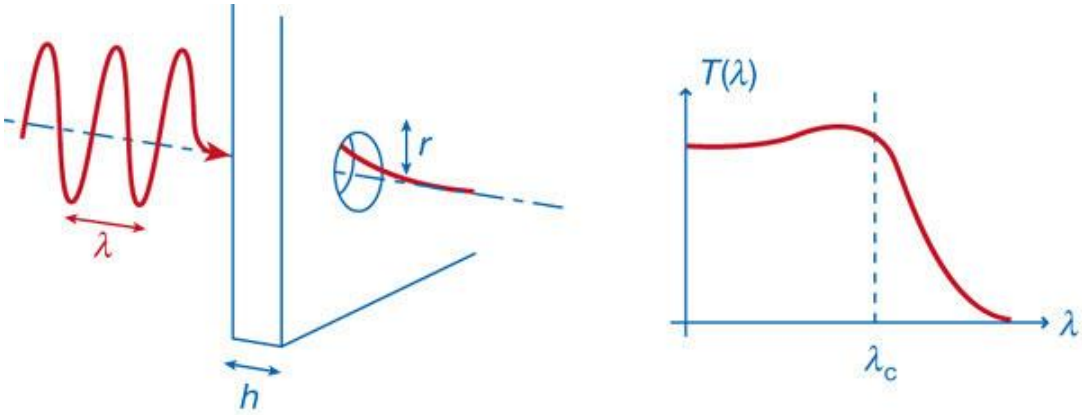

Figure 1.8: A single hole aperture on a real metal having thickness h (Left). A transmission spectrum through a single hole aperture for the real metal (Right).

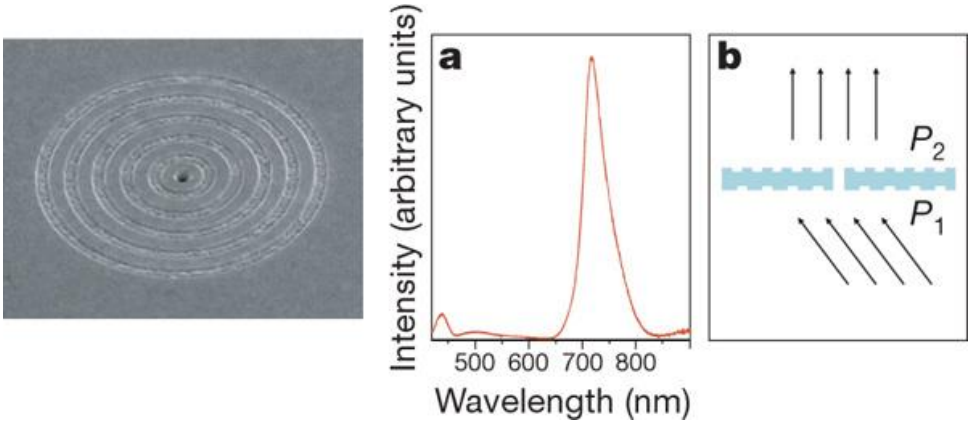

Figure 1.9: Photograph of a single aperture surrounded by periodic circular corrugations. (a) Transmission spectrum through a single aperture surrounded by periodic circular corrugations. (b) Schematic diagram of single hole aperture surrounded by circular corrugations on both sides [28].

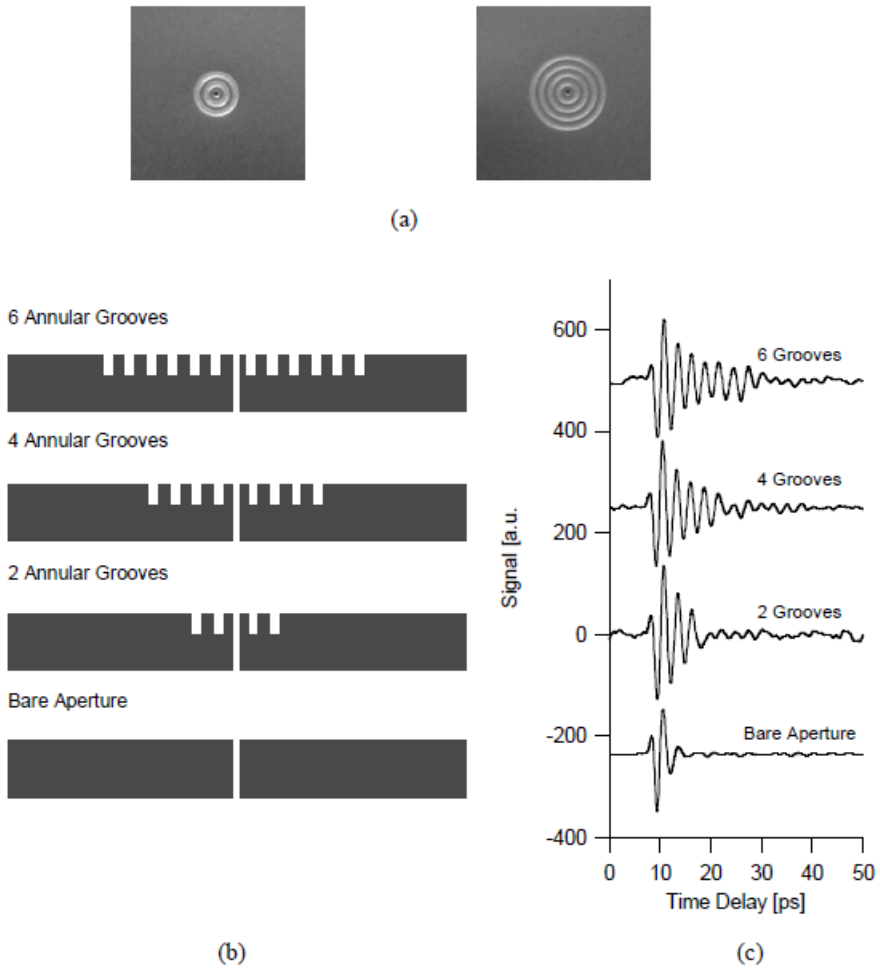

Fig. 1.10. Time domain waveform through bullseye structure. (a) Photographs of typical bullseye structures consisting of periodic multiple annular grooves (b) Cross-sectional line diagrams of the structures used (c) Five experimentally observed time-domain waveforms for the structures shown in part (b). The temporal waveforms have been offset from the origin for clarity. The number of oscillations, after the initial bipolar waveform, matches the number of annular grooves.

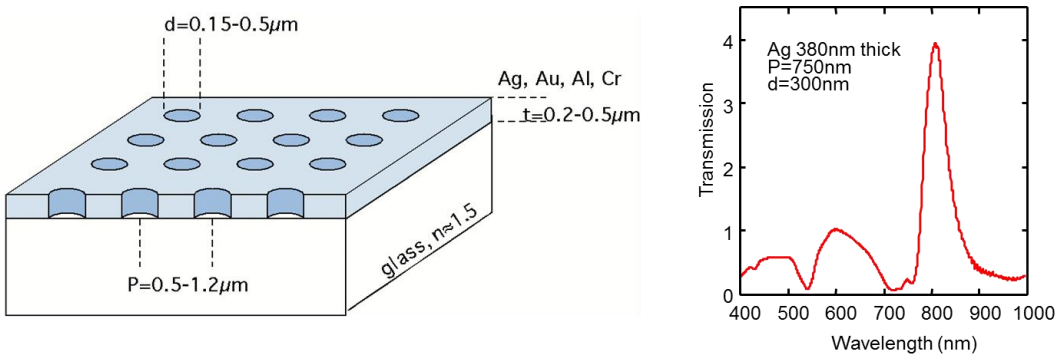

Figure 1.11: Schematic diagram of periodic hole array and the transmission spectrum through such hole array.

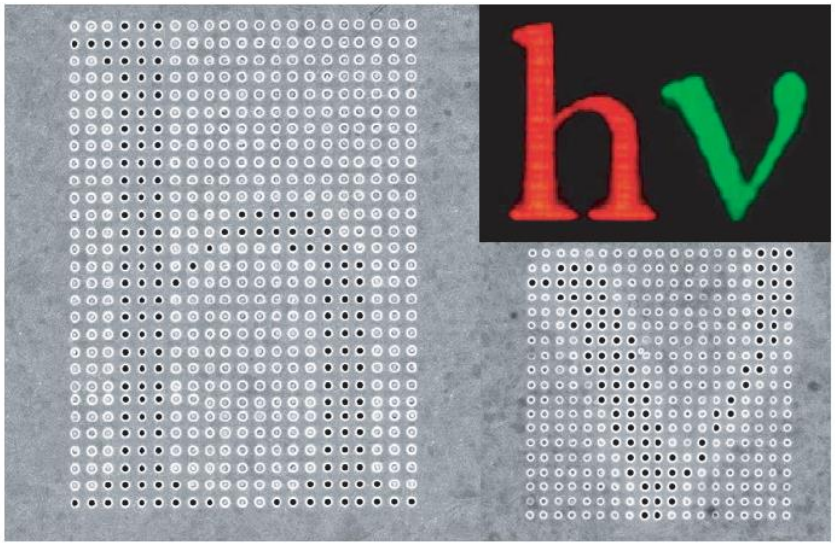

Figure 1.12: Holes in a dimple array generating the letter "hν".

CHAPTER 2

DEVICE FABRICATION AND MEASUREMENT

2.1 Inkjet Printing Techniques with Spatial Variation of Conductivity

Inkjet printing is a type of computer printing that recreates a digital image by propelling droplets of ink onto paper, plastic or other substrates [1]. An inkjet printer uses cyan, magenta, yellow and black cartridges (CMYK). In order to print a color image, different fractions of ink from each cartridge are dropped onto the substrate. The computer monitors radiate light whereas inked or printed paper absorbs or reflects light of certain wavelengths. The CMYK color model is a subtractive color model and serves as filters, subtracting varying degrees of red, green and blue light from white light to produce a selective gamut of spectral colors. Like monitors, printing inks also produce a color gamut that is only a subset of the visible spectrum, although the range is not the same for both. Consequently, the same art displayed on a computer monitor may not match to that printed in a publication. Also, because printing processes such as offset lithography use CMYK (cyan, magenta, yellow, black) inks, digital art must be converted to CMYK color for print. Some printers prefer digital art files be supplied in the RGB color space with ICC profiles attached. Images can then be converted to the CMYK color space by the printer using color management methods that honor profiles if present; this helps preserve the best possible detail and vibrancy. A subtractive color model white

RGB (red, green and blue) is an additive color model [2]. The color model for RGB and CMYK is shown in Figure 2.1 [2]. Printing with the metallic ink is the same as printing with the pigmented colors as described above.

In this case, instead of using the pigmented inks, the empty cartridges are filled with metallic inks with the help of syringes. The remaining cartridges are filled with aqueous ammonia solution. The plasmonic structures are designed with Adobe Illustrator and saved in pdf format. The structures are printed on a Polyethylene Terephthalate (PET) substrate and are chemically treated to avoid smearing the inks onto the substrate. The printer used in this case is an Epson Workforce 30, which is shown in Figure 2.2. In order to print the spatial variation of conductivity, two types of inks are used- one is silver and the other is carbon. Both inks are commercially available at methode.com. Silver ink is filled in the cyan cartridge while carbon is filled in the magenta cartridge. Designs are drawn using Adobe Illustrator. One of the designs is shown in Figure2.3.

In Figure 2.3, on the left side, the value of magenta is 100 % and it is decreasing as we move towards the right, but the value of cyan is increasing towards the right. On the right-most side, the value of cyan is 100 %. Once the structures are printed with silver and metallic ink, we get spatial variation of conductivity. In this case, magenta represents silver ink and cyan represents carbon ink. The content of silver ink is decreasing in discrete steps from left to right. The conductivity of the silver ink is 8.6 x 10^6 S/m, which is about 6 times smaller than the bulk silver conductivity. The carbon ink acts as a lossy dielectric ink and the conductivity of the carbon ink is 800 S/m. The resolution of the printer with these inks is about ~75 µm. An inkjet printer prints the structures line by line. The linewidth of the printed structure is ~100 µm. Once the

structures are printed, it does not require further processing [3]. The printed structure is shown in Figure 2.4. The printed structures show the same plasmonic response and do not change even after 3 months.

We have used two types of ink-silver and carbon to create spatial variation of conductivity. This spatial variation of conductivity allows us to control the propagation properties of surface plasmon. In order to have a greater control on the propagation properties of surface plasmon polarition, different types of inks can be used such as ferromagnetic ink. Multiple cartridges with varieties of inks can also be used to have greater control on the propagation properties of surface plasmon. The spatial resolution of the Epson workforce 30 printer is ~ 75 μm. Better resolutions and hence smaller features can be printed with expensive printers such as Epson 4800. With the dimatrix printer, much better resolution of up to 1 μm can be achieved [4]. However, the disadvantage of dimatrix printer is that it uses only one cartridge at a time. Hence, creating spatial variation of conductivity is very challenging with the dimatrix printer.

2.2. 3D Printing of Plasmonic Devices

3D printing is an additive manufacturing technique that is used to fabricate a three-dimensional object [5]. The term "additive manufacturing" accurately describes how this technology works to create objects. "Additive" refers to the successive addition of thin layers ~ 20 μm or greater to create an object. Almost any complex object can be created by this additive manufacturing technique. There are 4 main steps in creating plasmonic devices by 3D printing techniques- the first step is the designing the 3D file of the structures. The 3D file can be created by using CAD software or with SolidWorks.

The second step is the actual printing process. The materials used in 3D printing are very broad. It includes plastics, ceramics, resins, metals, textiles, biomaterials and glass, etc. [6]. While printing the actual object, support materials are used to support the hanging structures or it is the materials that are filled between the actual structures. The third process is removing the support materials. This is done by using the water jet. Once the supporting materials are removed, the fourth and final process is sputter coating of the 3D structures with gold. In order to make the plastic printed structures behave as a plasmonic device, it is sputter coated with gold. Once the structures are coated with more than twice the skin depth of gold in all directions, they become plasmonic devices. In order to ensure that the 3D structures are coated everywhere with the gold, the sample is turned each side and coated with the gold [7-9].

The 3D printing utilized for the purpose of printing our structure is Object EDEN260V. The materials used for the printing structure are VeroWhite polymer. The horizontal build layers are as fine as 16 micron. The build resolution of the printer is 600 dpi along the x and y axis, whereas along the z axis, it is 1600 dpi. The accuracy of the printer is about 60 microns [10]. The 3D printer Object EDEN260V is shown in Figure 2.5. The time required to print out a 3D geometry is volume dependent. For a waveguide with the length of 8 cm, width of 2 cm and thickness of 0.5 cm, the time required for the 3D printing is about an hour.

2.3 Terahertz Time Domain Spectroscopy and Terahertz Imaging

Figure 2.6 is a schematic diagram of the standard terahertz time domain spectroscopy (THz-TDS). In this case, a femtosecond laser emits a train of femtosecond

laser pulses at near infrared frequencies centered at 800 nm. The bandwidth of the infrared laser is around 100 nm. That means the incident infrared wavelength spans from 750 nm to 850 nm. The initial laser beam after passing through a beam splitter is split into two components in the ratio of 80:20. The initial power of the laser before the beam splitter is 1W. The beam having the power of 800 mw is called a pump beam whereas the lower power beam having the power of 200 mw is called the probe beam. The beam is passed through an optical chopper. After being modulated by the optical chopper, the beam is allowed to incident onto a second-order nonlinear crystal, ZnTe. When the optical beam (near infrared) passes through this nonlinear crystal, terahertz frequency spanning from 0 to 1.5 THz is generated through the optical rectification process, which is described in the Section 1.1. By using two off axis parabolic mirrors, the generated THz wave is focused onto another nonlinear ZnTe crystal as shown in Figure 2.7.

The detector crystal is an electro-optic crystal. The probe beam gates the detector and the response is proportional to the sign and amplitude of the terahertz electric field [11-16]. The amplitude of the THz pulse is measured for a particular time difference between the probe and pump. The output signal is typically proportional to the convolution of the probe beam and the THz pulse. Because the probe beam duration is much shorter than the THz pulse, at first order, the probe can be considered as a delta function, thus, the output is proportional to the amplitude of the THz pulse for that particular time delay between the probe and pump.

2.3.1 Electro-Optic Sampling (EO Sampling)

The Pockels effect is a change in the refractive index or birefringence that corresponds linearly with the electric field. However, Pockels effect only appears in crystals that have no inversion symmetry, for example, in zincblende crystals such as the ZnTe. Electro-optical sampling is based on the Pockels effect. In the EO sampling method, the THz field is measured by the change it causes on the birefringence properties of an EO crystal. Such changes in the birefringence of the EO crystal can be measured by analyzing the polarization properties of an optical probe beam going through the crystal. The most common setup to measure the THz waveform with EO sampling is with a balanced measurement approach (Figure 2.8). In this approach, a linearly polarized optical probe beam goes through a polarizer and then travels through the EO crystal. A quarter wave plate (QWP) located after the EO crystal changes the ellipticity of the probe beam and a Wollaston prism separates the two perpendicular components of the elliptical polarization. Each polarization intensity is detected by a photo-diode. The photo-diodes are conFigured in differential mode so common laser noise is cancelled. When no THz wave is illuminating the EO crystal, the ellipticity of the probe beam can be set so that both polarizations are equal and therefore, the net current from the photo-diodes assembly is zero. When a THz wave illuminates the EO crystal, the electric field associated with the THz wave changes the birefringence of the material and, thus, it changes the ellipticity of the probe beam. This change in ellipticity breaks the balance between the two polarizations and, therefore, a net current is generated at the photodiodes assembly that is proportional to the amplitude of the electric field of the THz wave [17-20].

2.3.2 Terahertz Imaging (TI)

The terahertz imaging system has an inherent advantage over millimeter waves (30 GHz-300GHz) due to its short wavelength, which gives better spatial resolution. The main features of terahertz imaging are – (a) THz waves are transparent through most of the dielectrics which allows imaging samples that are wrapped or covered with the dielectrics; (b) gives much better resolution than the mm waves; (c) with a pulsed laser system, not only the structural information but the chemical information can be achieved; (d) THz waves are non-ionizing radiation due to the low energy of photons and can be used in security scanners instead of X-rays. Terahertz imaging can be realized using both continuous (CW) and pulsed laser systems. In our lab, we have the capability of both THz imaging using both CW and pulsed laser systems. A commercially available continuous terahertz imaging camera is available. We have two CW terahertz cameras that work at 100 GHz and 300 GHz from Terasense as shown in Figure 2.9. The output power of the CW THz is 80 mw. As CW-THz takes images at a single frequency, it can reveal the shapes of the hidden objects but cannot give the spectral information about the objects. However, if the images are taken at different discrete frequencies and algorithmically combined, it is possible to distinguish substances spectroscopically. The other capability of THz imaging technique in our lab is based on electro-optic sampling for real-time THz imaging. The schematic diagram of real-time terahertz imaging is shown in Figure 2.5. The imaging setup is the same as the THz-TDS setup except the photodiode, quarter wave plate and the Wollaston prism in the THz-TDS are replaced by the CCD camera. The CCD camera we have used in this case is a thermoelectrically cooled CCD camera that has a high wide spectral range, a high dynamic rage, and high

thermal and temporal stability. The spectral range for the TE/CCD camera is from 400-1100 nm [21-22]. The procedure for obtaining the real-time imaging with the TE/CCD camera is described below.

In the THz-TDS, the temporal waveform is obtained by moving the delay stage. As the delay stage moves, we measure the convolution of the terahertz wave and the optical probe beam. The entire temporal waveform can be obtained by moving the delay stage sufficiently long. When the path length between the pump and probe beam is exactly the same, we see the signal peak in the time domain. In the terahertz imaging system, we obtained the terahertz signal by taking the two images- one with the pump beam and one without the pump beam. When the path length between the pump and the probe beam is exactly the same, the difference between these two images give the terahertz signal. The camera has the pixel resolution of 512 X 512. The pixels were binned to form a 128 X 128 pixel array, which allowed for greater dynamic range in the measurements. This corresponds to taking 16384 independent time-domain waveforms simultaneously. The waveforms obtained for each effective pixel were then Fourier transformed and the magnitude of the amplitude spectra at the desired frequency was recorded and plotted to form the false color beam profiles.

2.4 References

1. "Ink-jet - Definition of ink-jet by Merriam-Webster". Merriam-webster.com.
2. http://www.printernational.org/rgb-versus-cmyk.php.
3. B. Gupta, S. Pandey, S. Guruswamy, and A. Nahata, “Terahertz plasmonic structures based on spatially varying conductivities,” Advanced Optical Materials, vol. 2, no. 6, pp. 565–571, Jun. 2014.

4. http://www.fujifilmusa.com/products/industrial_inkjet_printheads/deposition-products/dmp-2800/index.html.

5. Excell, Jon. "The rise of additive manufacturing". The Engineer. Retrieved 2013-10-30.

6. http://www.shapeways.com/materials.

7. http://www.stratasys.com/3d-printers/design-series/objet-eden260vs.

8. S. Pandey, B. Gupta, and A. Nahata, "Terahertz plasmonic waveguides created via 3D printing," Opt. Express, vol. 21, no. 21, pp. 24422–24430, Oct. 2013.

9. B. Gupta, S. Pandey, and A. Nahata, "Plasmonic waveguides based on symmetric and asymmetric T-shaped structures," Opt. Express, vol. 22, no. 3, pp. 2868–2880, Feb. 2014.

10. G. Gallot and D. Grischkowsky, "Electro-optic detection of terahertz radiation," J. Opt. Soc. Am. B, JOSAB, vol. 16, no. 8, pp. 1204–1212, Aug. 1999.

11. Q. Wu and X.-C. Zhang, "Free-space electro-optic sampling of terahertz beams", Appl. Phys. Lett. 67, 3523, Dec (1995).

12. Nahata, Ajay and Yardley, James T. and Heinz, Tony F, "Free-space electro-optic detection of continuous-wave terahertz radiation", Applied Physics Letters, 75, 2524-2526, Oct. (1999).

13. Zomega Terahertz Corporation, "The Terahertz Wave Ebook", Edition June 2012.

14. D. Grischkowsky, S. Keiding, M. van Exter, and C. Fattinger, "Far-infrared time-domain spectroscopy with terahertz beams of dielectrics and semiconductors," *J. Opt. Soc. Am. B, JOSAB*, vol. 7, no. 10, pp. 2006–2015, Oct. 1990.

15. B. Gupta, S. Pandey, S. Guruswamy, and A. Nahata, "Terahertz plasmonic structures based on spatially varying conductivities," Advanced Optical Materials, vol. 2, no. 6, pp. 565–571, Jun. 2014.

16. J. Valdmanis, G. Mourou, and C. Gabel, "Subpicosecond electrical sampling," IEEE Journal of Quantum Electronics, vol. 19, no. 4, pp. 664–667, Apr. 1983.

17. F. Friederich et al., "THz active imaging systems with real-time capabilities," IEEE transactions on terahertz science and technology, vol. 1, no. 1, pp. 183–200, Sep. 2011.

18. Q. Song, Y. Zhao, A. Redo-Sanchez, C. Zhang, and X. Liu, "Fast continuous terahertz wave imaging system for security," Optics Communications, vol. 282, no.

10, pp. 2019–2022, May 2009.

19. X.-C. Zhang, “Three-dimensional terahertz wave imaging,” Philosophical Transactions of the Royal Society of London A: Mathematical, Physical and Engineering Sciences, vol. 362, no. 1815, pp. 283–299, Feb. 2004.

20. Z. Jiang and X.-C. Zhang, “Terahertz imaging via electrooptic effect,” IEEE Transactions on Microwave Theory and Techniques, vol. 47, no. 12, pp. 2644–2650, Dec. 1999.

21. Two-dimensional imaging of continuous-wave terahertz radiation using electro-optic detection,” Appl. Phys. Lett., vol. 81, no. 6, pp. 963–965, Jul. 2002.

22. http://www.teraview.com/products/terahertz-continuous-wave-cw400/imaging.html.

23. ftp://ftp.princetoninstruments.com/Public/Manuals/Old%20Catalogs/imagcat (d).pdf.

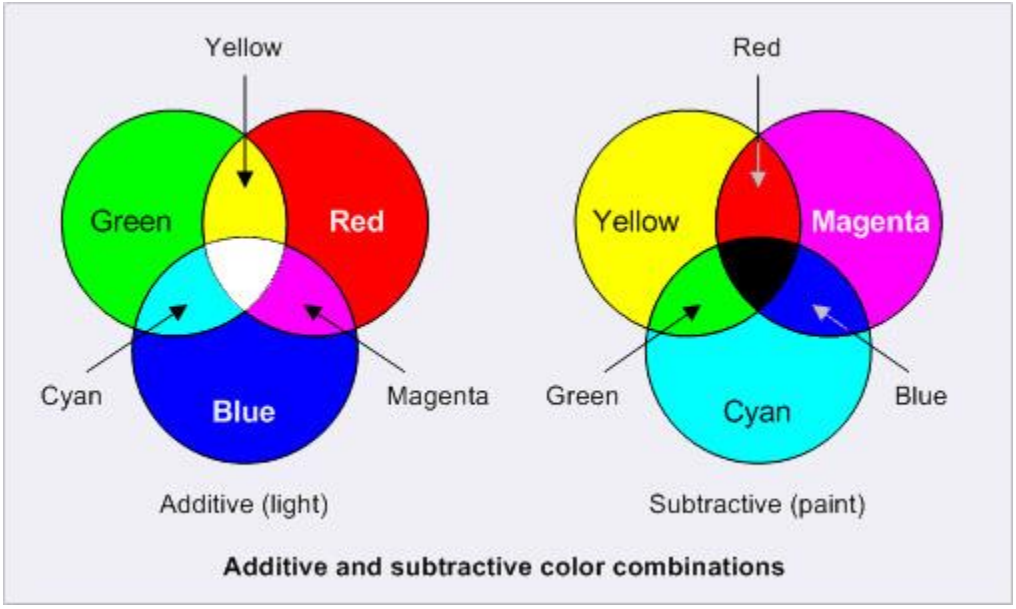

Figure 2.1: RGB color vs. CMYK color model

Figure 2.2: Epson Workforce 30 printer and the empty cartridges.

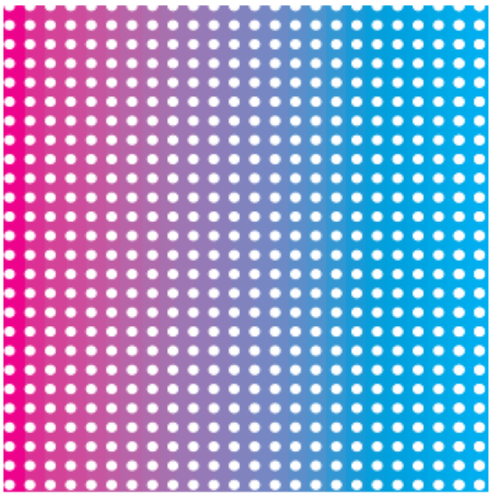

Figure 2.3: Spatial variation of conductivity designed using Adobe Illustrator.

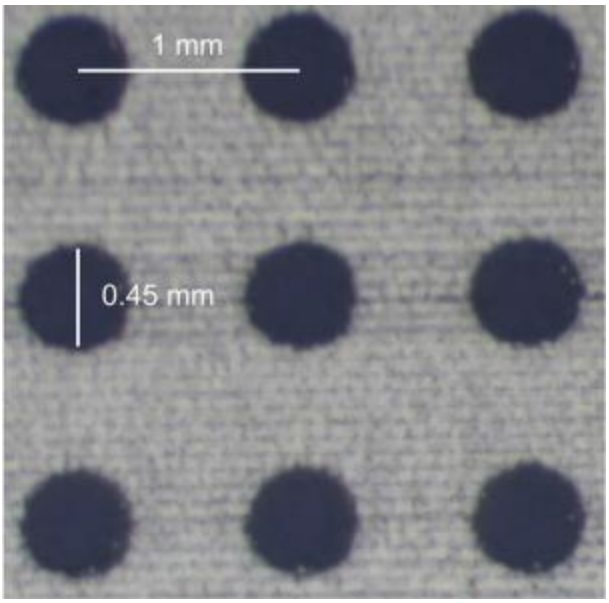

Figure 2.4: Photograph of the hole array with 100 % silver ink.

Figure 2.5: Photograph of Object EDEN260V 3D printer.

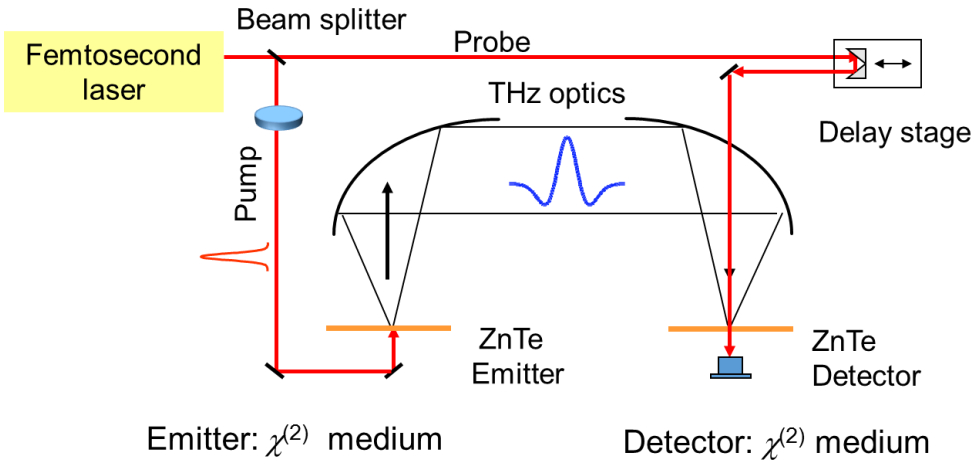

Figure 2.6: Schematic diagram of terahertz time domain spectroscopy.

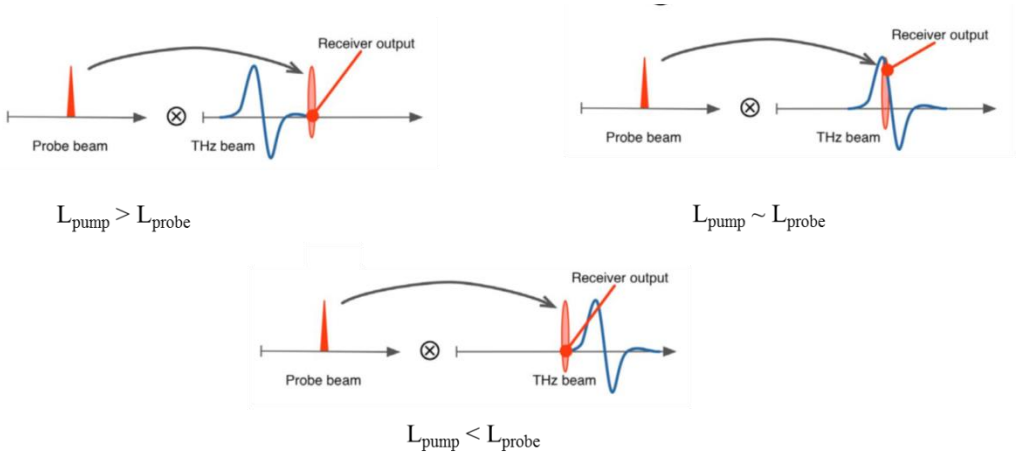

Figure 2.7: Convolution between probe beam and the pump beam with different times.

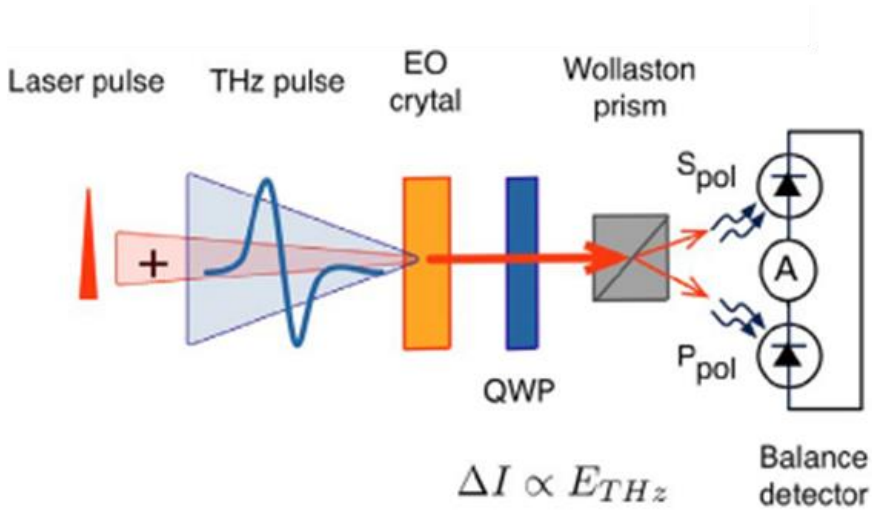

Figure 2.8: Electro-optical sampling schematic diagram.

Figure 2.9: Continuous THz source and THz detector.

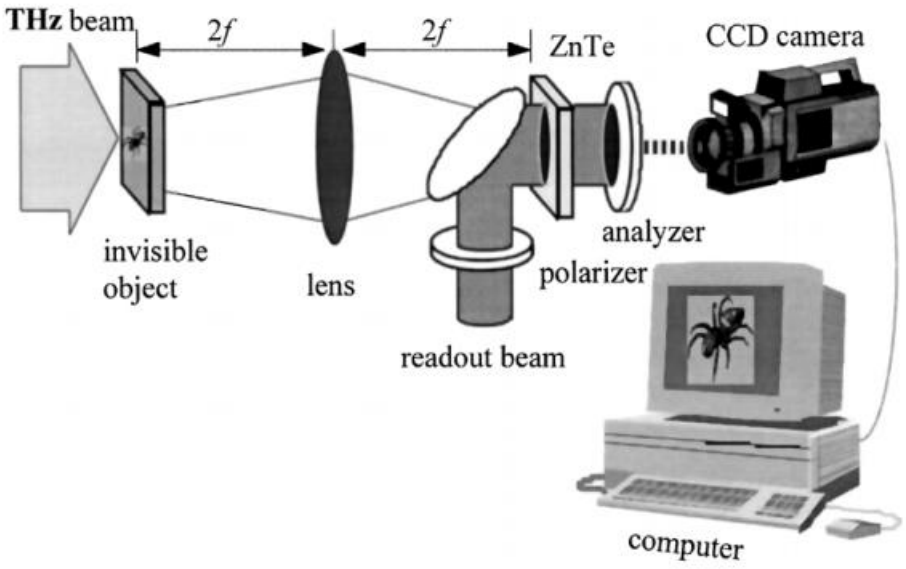

Figure 2.10: 2-D real-time terahertz imaging system via EO effect. (Z. Jiang and X.-C. Zhang, "Terahertz imaging via electrooptic effect," IEEE Transactions on Microwave Theory and Techniques, vol. 47, no. 12, pp. 2644–2650, Dec. 1999).

CHAPTER 3

TERAHERTZ PLASMONIC STRUCTURES BASED ON SPATIALLY VARYING CONDUCTIVITIES

www.MaterialsViews.com

ADVANCED OPTICAL MATERIALS
www.advopticalmat.de

Terahertz Plasmonic Structures Based on Spatially Varying Conductivities

*Barun Gupta, Shashank Pandey, Sivaraman Guruswamy, and Ajay Nahata**

Terahertz plasmonic structures are demonstrated in which the conductivity of the metallic film is varied spatially in order to further enhance the response. Using a commercially available inkjet printer, in which one cartridge is filled with conductive silver ink and a second cartridge is filled with resistive carbon ink, computer generated drawings of plasmonic structures are printed in which the individual printed dots can have differing amounts of the two inks, thereby creating a spatial variation in the conductivity. The silver ink has a DC conductivity that is only a factor of six lower than bulk silver, while the carbon ink acts as a lossy dielectric at THz frequencies. Both inks sinter at room temperature immediately after contact with the plastic film. Using a periodic array of subwavelength apertures as a test structure, patterns printed with different fractional amounts of the two inks show dramatically different enhanced optical transmission properties. These differences arise from changes in the propagation loss properties as a function of conductivity. This data is used to design and fabricate aperture arrays in which the conductivity varies spatially. The resulting plasmonic effect is found to dramatically alter the spatial beam profile of the transmitted THz radiation, as measured by THz imaging.

1. Introduction

Plasmonic devices offer unique capabilities for controlling the propagation properties of electromagnetic radiation, because the dispersion properties of surface plasmon-polaritons (SPPs) differ dramatically from that of freely propagating radiation.[1] A standard approach used to fabricate such structures typically begins with a homogeneous metal film that is patterned to yield the desired plasmonic response. Such structuring can allow for enhanced optical transmission through subwavelength apertures,[2,3] subwavelength confinement of radiation[4,5] and the development of unique device technologies.[6–9] At optical frequencies, the most common metals used for such structures are Au and Ag, since most other metals exhibit unacceptably high losses. As one moves to longer wavelengths, a broader range of materials has been shown to support relatively low loss propagation of surface plasmon-polaritons (SPPs), including not only all conventional metals[10] and superconductors,[11] but also more exotic metals such as doped semiconductors,[12,13] graphene,[7,8] conducting polymers[14] and liquid metals.[9] In the terahertz (THz) spectral range, for example, all conventional metals exhibit very large conductivities, corresponding to long propagation lengths, while many exotic metals exhibit lower conductivities, corresponding to higher propagation losses and therefore shorter propagation lengths.

In an effort to expand the parameter space for the development of new and unique plasmonic device capabilities, it would be beneficial to be able to pattern multiple plasmonic materials, with different conductivities, as an example, within a single two-dimensional (2D) structured film. Such patterning would enable an additional level of control over the propagation properties of optical radiation. A variety of different deposition and patterning techniques exist to create the requisite pattern. Among these, the use of conventional microfabrication techniques involving vacuum deposition of the plasmonic material and a subsequent etching or lift-off step to create the final device is the most common. Using this approach, creating a pattern with multiple materials is certainly possible using conventional microfabrication techniques, although each material would typically require the addition of multiple deposition and patterning steps. Thus, such an approach would usually be limited to the inclusion of only a few different materials or material variations. An alternate approach that is promising requires the use of an inkjet printer. Such printers have shown great success in printing antennas,[15] organic electronics,[16] thin film transistors[17] and metamaterials.[18,19] This is often accomplished using sophisticated MEMS-based printers, which allow for the fabrication of high resolution patterns. However, such printers also typically allow for only one type of ink to be printed at a time.

In this letter, we report the demonstration of THz plasmonic structures in which the conductivity of the metallic film can be spatially varied widely using low cost, commercially available

B. Gupta, S. Pandey, Prof. A. Nahata
Department of Electrical and Computer Engineering
University of Utah
50 S. Central Campus Dr.
Salt Lake City, UT 84112, USA
E-mail: nahata@ece.utah.edu
Prof. S. Guruswamy
Department of Metallurgical Engineering
University of Utah
135 S 1460 East
Salt Lake City, UT 84112, USA

DOI: 10.1002/adom.201400018

ADVANCED OPTICAL MATERIALS
www.advopticalmat.de

www.MaterialsViews.com

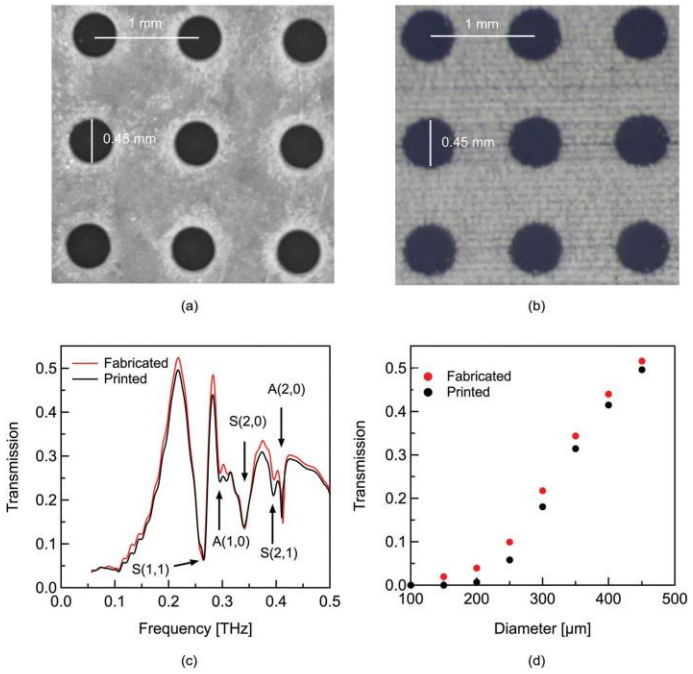

Figure 1. Properties of microfabricated and printed aperture arrays. (a) Image of a portion of an aperture array fabricated using a 1 μm thick sputtered silver film and then etched to yield the final pattern with the relevant dimensions shown (a) Image of a portion of an aperture array printed using conductive silver ink with the relevant dimensions shown. (c) Amplitude transmission spectra for the two arrays normalized using the transmission properties of a bare PET sheet. The Bragg indices for each resonance are given by A(i,j), corresponding to the (i,j) resonance for the metal-air interface, and S(i,j), corresponding to the (i,j) resonance for the metal-substrate interface. (d) The magnitude of the lowest order resonance at 0.22 THz as a function of the aperture diameter keeping the periodicity fixed at 1 mm.

color inkjet printers. For the present demonstrations, we use one color cartridge filled with conductive silver ink and a second color cartridge filled with resistive carbon ink. Using a periodic array of subwavelength apertures[2] as a test structure, we initially investigate the enhanced THz transmission properties as a function of the (homogeneous) printed layer conductivity, by varying the fractional content of silver and carbon ink in each printed image. Using this information, we create aperture arrays imprinted with different spatial conductivity patterns and investigate the effect of the resulting structures on the spatial profile of a broadband THz beam using THz imaging.

2. Results and Discussion

In order to demonstrate the utility of inkjet printing for this application, we first compared equivalent devices: one fabricated via inkjet printing and the other fabricated using conventional microfabrication techniques. For printing purposes, we used an Epson Workforce 30 color inkjet printer with a conductive silver ink and printed a 5 cm × 5 cm array of subwavelength apertures on surface treated PET (polyethylene terephthalate) sheets. The array consisted of 450 μm diameter apertures on a square lattice with a center-to-center spacing of 1 mm. We also fabricated an identical aperture array on the same PET sheet using a 1 μm thick sputter deposited Ag film that was subsequently etched to yield the desired pattern. Expanded views of a portion of the two arrays are shown in **Figure 1**a and b. In contrast to the microfabricated structure, the inkjet printed pattern consists of silver lines that are ~100 μm wide, corresponding to the resolution of the printer. The Ag ink sintered at room temperature immediately upon printing, and required the use of the surface treated PET sheets, so no additional processing was required to yield the final device. We used a four point probe technique to measure the dc conductivity of the two samples and found that it was 5×10^7 S/m for the sputter deposited Ag and 8.6×10^6 S/m for the sintered Ag ink. The conductivity value for the sputter deposited Ag is nearly identical to that of published values for bulk silver,[20] while that for the sintered Ag ink is only a factor of six smaller.

www.MaterialsViews.com

ADVANCED OPTICAL MATERIALS
www.advopticalmat.de

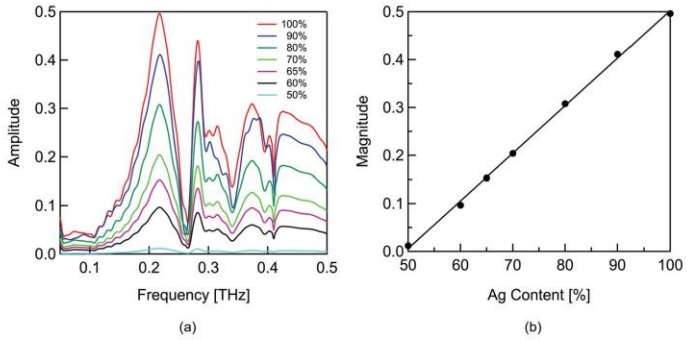

Figure 2. THz transmission properties as a function of the Ag content. (a) Normalized amplitude spectra for periodic aperture arrays (450 μm aperture diameter, 1 mm periodicity) as a function of the silver content, when silver and carbon ink are printed simultaneously. For each array, the entire printed layer has the same Ag content. (b) The magnitude of the transmission resonance at 0.22 THz as a function of the Ag content. The line is a linear least-squares fit to the data.

In Figure 1c, we show the normalized THz transmission spectra for both devices, using a bare surface treated PET sheet as the reference. The fact that the two spectra are nearly identical is consistent with the fact that high conductivities of conventional metals, including that of the Ag ink, in the THz regime corresponds to propagation lengths that are much larger than the spatial extent of the array.[21] There are several prominent resonances visible in the spectrum. As we have previously shown, it is the dips on the high frequency side of each resonance that are fixed, for a given periodicity, and that correspond to the k-space representation of the geometry.[3] For the metal-air interface, we would expect transmission minima at 0.3 THz [(±1, 0) resonance] and 0.42 THz [(±1, ±1) resonance]. The THz refractive index of the PET substrate was found to be 1.72 across the measured THz window, consistent with published data,[22] corresponding to additional transmission minima at 0.25 THz [(±1, ±1) resonance], 0.35 THz [(±2, 0) resonance], and 0.39 THz [(±2, ±1) resonance] for the metal-plastic substrate interface. The lowest order (±1, 0) resonance at 0.175 THz for the metal-plastic interface is not visible. These values are in excellent agreement with the experimentally observed transmission minima frequencies in Figure 1c.

In order to understand how well the printed arrays compare to more conventionally fabricated arrays, we printed a series of structures using silver ink and fabricated a series of arrays using conventional microfabrication techniques and sputter deposited silver films, leaving the periodicity at 1 mm and progressively reducing the aperture diameter. In Figure 1d, we show the magnitude of the metal-plastic interface (±1, ±1) resonance peak at 0.22 THz, as a function of the aperture diameter. As expected, the transmission properties of both arrays decrease with decreasing aperture size. Importantly, the transmission of that peak goes to nearly zero as the aperture diameter is reduced to ~200 μm. While the printer has an optimized print resolution of 5760 × 1440 dpi, corresponding to printed dots that are less than 20 μm along each axis, the apertures printed using these types of inks become poorly defined for diameters less than ~250 μm and beginning filling in for smaller diameters. In all of the work that follows, we use only 5 cm × 5 cm arrays with 450 μm diameter apertures with a 1 mm periodic spacing.

With the basic properties of the silver ink and the printing process established, we now investigate the properties of plasmonic structures when two different inks are simultaneously printed (i.e. the ink conductivity is varied). In **Figure 2**a, we show the THz transmission properties for a series of periodic aperture arrays printed with varying fractions of silver and carbon ink. The patterns were first drawn using conventional presentation software and uniformly colored, using a mixture of two colors (magenta and cyan), where the magenta cartridge was filled with pure silver ink and cyan cartridge was filled with pure carbon ink. We printed a total of 10 different arrays, each with a different amount of Ag ink that varied between 0% and 100% (only data between 50% and 100% is shown).

There are a number of interesting features present in these spectra. The array printed using pure Ag ink shows the greatest level of enhanced THz transmission, as expected given that it has the highest conductivity. As the Ag content is decreased, so is the magnitude of the transmission resonances. In fact, while the shape of the spectrum remains largely unchanged, the overall transmission decreases with decreasing silver content. This is consistent with the fact that a lower conductivity leads to increased propagation losses for SPPs. When the silver content dropped below ~40% in the printed film, the overall transmission began to rise, although no transmission resonances were apparent in the corresponding spectra. This occurs because pure carbon acts as a lossy dielectric and the low silver content (<40%) does not enable the printed layer to support the propagation of SPPs over distances sufficient to allow for the formation of resonances. This is more clearly exemplified in Figure 2b, where we show the magnitude of the lowest order transmission resonance at 0.22 THz as a function of the

ADVANCED OPTICAL MATERIALS
www.advopticalmat.de

www.MaterialsViews.com

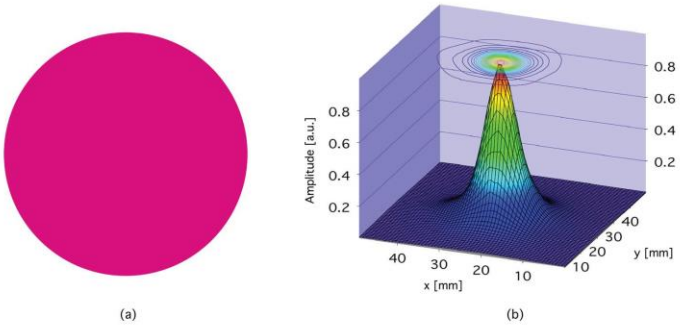

Figure 3. Beam properties for an aperture array printed using a homogeneous ink layer. (a) Schematic drawing of the 25.4 mm diameter aperture array printed using only 100% Ag ink (magenta corresponds to pure silver ink). The periodic aperture array (not shown) is fabricated within this printed disk and consists of 450 μm diameter apertures on a square lattice with 1 mm periodicity. (b) Measured THz beam profile at 0.22 THz (frequency of the lowest order transmission resonance). The beam profile was Gaussian with a 1/e beam width of 11.5 mm along both the x- and y-axes.

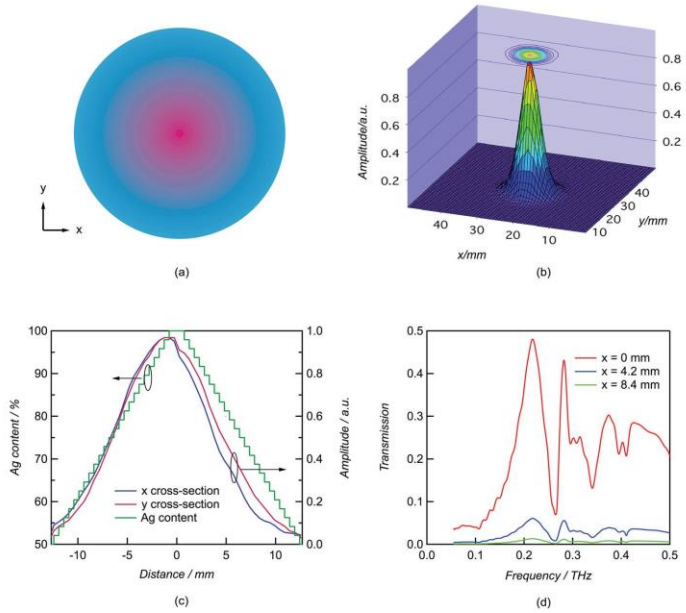

Figure 4. Beam properties for an aperture array printed with outwardly decreasing conductivity. (a) Schematic drawing of the 25.4 mm diameter aperture array in which the conductivity was varied such that the Ag content decreased from 100% to 50% in 25 discrete steps moving radially outward from the center (for clarity, magenta corresponds to 100% Ag ink, cyan corresponds to 50% Ag ink and 50% carbon ink in this image). The periodic aperture array (not shown) is fabricated within this printed disk and consists of 450 μm diameter apertures on a square lattice with 1 mm periodicity. (b) Measured THz beam profile at 0.22 THz (frequency of the lowest order transmission resonance). The beam profile was Gaussian with a 1/e beam width of 7.8 mm along both the x-axis and 7.6 mm along the y-axis. (c) Left axis – Ag content in the printed structure along the x and y-axes. Right Axis – ratio of the measured beam profile in (b) with that of the reference beam profile in Figure 3b along the x and y axes. The origin lies at the center of the pattern. (d) Amplitude spectra measured at 3 points along the x-axis.

www.MaterialsViews.com

ADVANCED OPTICAL MATERIALS
www.advopticalmat.de

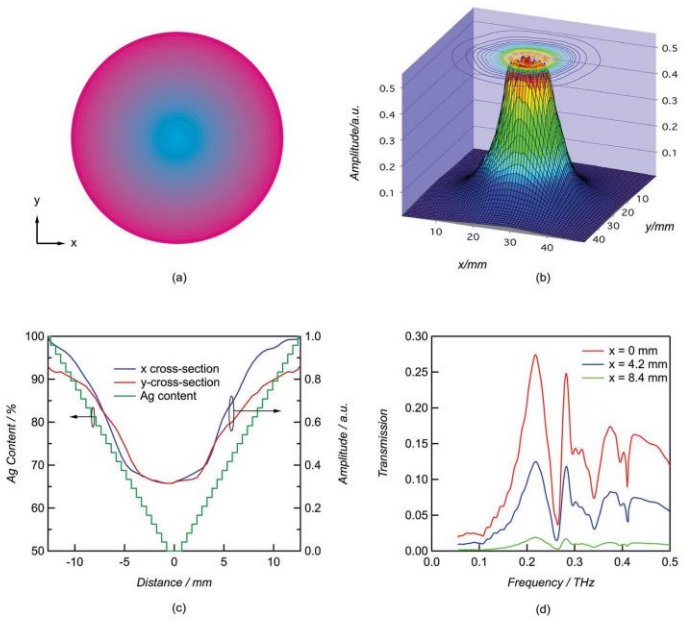

Figure 5. Beam properties for an aperture array printed with outwardly increasing conductivity. (a) Schematic drawing of the 25.4 mm diameter aperture array in which the conductivity was varied such that the Ag content increased from 50% to 100% in 25 discrete steps moving radially outward from the center (for clarity, magenta corresponds to 100% Ag ink, cyan corresponds to 50% Ag ink and 50% carbon ink in this image). The periodic aperture array (not shown) is fabricated within this printed disk and consists of 450 μm diameter apertures on a square lattice with 1 mm periodicity. (b) Measured THz beam profile at 0.22 THz (frequency of the lowest order transmission resonance). The beam profile was Gaussian with a 1/e beam width of 19.1 mm along both the x-axis and 19.4 mm along the y-axis. (c) Left axis – Ag content in the printed structure along the x and y-axes. Right Axis – ratio of the measured beam profile in (b) with that of the reference beam profile in Figure 3b along the x and y axes. The beam profile was scaled by an additional factor of 0.575 to allow for comparison between the figures. The origin lies at the center of the pattern. (d) Amplitude spectra measured at 3 points along the x-axis.

fractional Ag content in the printed ink (above 50%). Over this range, the magnitude of the resonance appears to scale linearly with the Ag content. Thus, for the purposes of plasmonics applications discussed below, we only consider printing areas with Ag content between 50–100%.

The ability to vary the propagation losses for SPPs suggests a range of new device possibilities. We discuss one embodiment of this concept to shape the beam profile of freely propagating THz radiation by analyzing four separate aperture arrays that have identical geometrical properties (450 μm aperture diameter with a 1 mm periodicity), but different conductivity variations. The spatial beam properties are measured using conventional THz imaging. In the first sample, used as a reference for subsequent demonstrations, we printed a 25 mm diameter array using pure silver ink, as depicted in **Figure 3**a, where we show a solid magenta circle (magenta corresponds to 100% Ag). In Figure 3b, we show the measured THz beam profile at 0.22 THz, which corresponds to the frequency of the lowest order transmission resonance peak. The beam profile is approximately Gaussian and has a 1/e beam width of 11.5 mm along both the x- and y-axes.

In the next printed aperture array, the conductivity of the 25 mm diameter aperture array was varied such that the Ag content decreased from 100% to 50% in 25 discrete steps moving radially outward from the center, as shown in **Figure 4**a. The corresponding measured spatial beam profile, measured at 0.22 THz, is shown in Figure 4b. The measured 1/e beam width, in this case, is 7.8 mm along the x-axis and 7.6 mm along the y-axis. The decrease in the beam width along both axes is consistent with the increasing propagation loss with increasing radial coordinate, which would lead to decreased transmission near the periphery of the array. In order to assess the correlation between the Ag content and beam cross-section, we take the ratio of the spatial beam profile, shown in Figure 4b, with the reference spatial beam profile shown in Figure 3b and show the resulting amplitude cross-sections along the x- and y-axes, as shown in Figure 4c. The excellent match between the two plots clearly demonstrates the utility of this printing

ADVANCED OPTICAL MATERIALS
www.advopticalmat.de

Materials Views
www.MaterialsViews.com

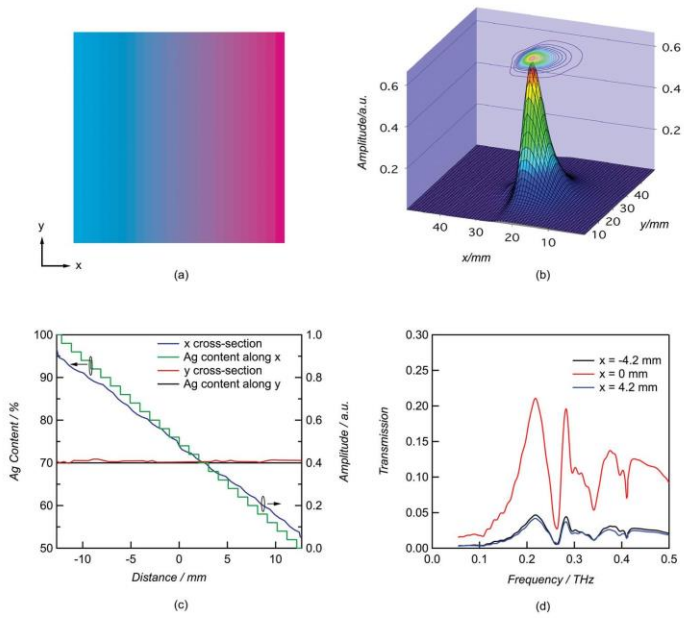

Figure 6. Beam properties for an aperture array printed with horizontally increasing conductivity. (a) Schematic drawing of the 25.4 mm × 25.4 mm aperture array in which the conductivity was varied such that the Ag content increased from 50% to 100% in 26 discrete steps moving horizontally (for clarity, magenta corresponds to 100% Ag ink, blue corresponds to 50% Ag ink and 50% carbon ink in this image). For each strip, the Ag content did not vary along the y-axis. The periodic aperture array (not shown) is fabricated within this printed disk and consists of 450 μm diameter apertures on a square lattice with 1 mm periodicity. (b) Measured THz beam profile at 0.22 THz (frequency of the lowest order transmission resonance). The beam profile was Gaussian with a 1/e beam width of 11.5 mm along the x-axis and 7.4 mm along the y-axis. (c) Left axis – Ag content in the printed structure along the x and y-axes. Right Axis – ratio of the measured beam profile in (b) with that of the reference beam profile in Figure 3b along the x and y axes. The origin lies at the center of the pattern. (d) Amplitude spectra measured at 3 points along the x-axis.

approach. Using THz imaging, we simultaneously measure 16,324 amplitude spectra (128 × 128 pixels). In Figure 4d, we show three representative spectra for positions along the x-axis (the center of the image corresponds to the origin). As expected from the data in Figure 2, the spectra appear to simply be scaled versions of one another. Indeed, all of the spectra have the same basic form, but are scaled according to the Ag ink content and location in the pattern.

Next, we printed an aperture array in which the conductivity was varied such that the Ag content increased radially from 50% to 100% in 25 discrete steps moving radially outward, as shown in **Figure 5**a. In Figure 5b, we show the measured spatial beam properties for the transmitted radiation from this array measured at 0.22 THz. The measured 1/e beam width, in this case, was 19.1 mm along the x-axis and 19.4 mm along the y-axis. Here, the spatial beam profile exhibits a flat top near the center and an overall increased beam width along both axes. This is generally consistent with the low transmission near the center of the array and decreasing propagation loss with increasing radial coordinate. In Figure 5c, we show both the Ag content as a function of the coordinate, along with the normalized amplitude cross-sections (ratio of the beam profile in Figure 5b with that in Figure 3b). Near the center of the array, the normalized beam profile does not match the conductivity change exactly. This may arise from the fact that while SPPs experience high propagation loss in that region, they can still propagate far enough to ensure that the transmission is not completely suppressed, but rather somewhat constant (i.e. a flat top). In Figure 5d, we show three representative spectra for positions along the x-axis (the center of the image corresponds to the origin). Once again, each of these spectra have the same form.

Finally, we printed a 25 mm x 25 mm aperture array, in which the Ag content increased along the x-axis from 50% to 100% in 26 discrete steps, as shown in **Figure 6**a. The Ag content along the y-axis was kept constant along each of the individual 26 strips. Once again, the measured spatial beam properties for the transmitted radiation from this array measured at 0.22 THz are shown in Figure 6b. The measured 1/e beam width, in this case, was 11.5 mm along the x-axis and 7.4 mm along the y-axis. The latter dimension is consistent with the fact that the Ag

content did not vary along the y-axis for each individual strip, while the x-axis beam profile clearly shows the asymmetric nature of the pattern. In Figure 6c, we show both the Ag content as a function of the coordinate, along with the normalized amplitude cross-sections (ratio of the beam profile in Figure 6b with that in Figure 3b). The data for the y-axis (Ag content and beam cross-section) is only shown for the strip that contains 70% Ag. As with the two previous structures, we find that the agreement is excellent between the two plots. In Figure 6d, we show three representative spectra for positions along the x-axis (the center of the image corresponds to the origin), with spectra from both sides of the origin because of the asymmetry of the pattern. We note that the asymmetry causes a shift in the location of the peak. Therefore, the beam maximum does not occur at the origin (i.e. x = 0 mm).

3. Conclusion

We have demonstrated that inkjet printing of plasmonic structures, using conventional color inkjet printers, offers greater control over the propagation properties of SPPs by allowing for the inclusion of a spatially varying conductivity. To demonstrate this, we first showed that in homogeneous printed aperture arrays, we could scale the transmission spectrum, without changing the shape of the spectrum noticeably, by simply changing the fractional levels of Ag and carbon inks in the printed layer. Using this information, we imprinted several different spatial variations in the conductivity of the printed aperture arrays and showed that we could alter the beam profile of the transmitted THz radiation in a controlled manner. In the present demonstration, this was shown using only two types of ink: a conductive Ag ink and a lossy carbon ink. More generally, up to four different types of ink, in a CMYK color inkjet printer, can be handled at once. Furthermore, other types of ink, such as magnetic materials, can be printed to control the properties of magneto-plasmons. Finally, this process can be extended beyond the THz spectral range by using printers and inks that allow for appropriate scaling of the phenomenon.

4. Experimental Section

Characterization of Transmission Properties: We used an amplified ultrafast Ti:sapphire laser as the optical source for all of the THz time-domain spectroscopy measurements.[23] The output of the laser was split 80:20 to yield the optical pump and probe beams, respectively. Broadband THz radiation was generated using a 1 mm thick <110> ZnTe crystal. An off-axis paraboloidal mirror was used to collect and collimate the THz radiation as it propagated from the emitter to the sample, resulting in a beam that was normally incident onto the printed sample. A second off-axis paraboloidal mirror was used to refocus the transmitted THz radiation onto a 1 mm thick <110> ZnTe detection crystal, which allowed for coherent detection of the radiation via electro-optic sampling.[24]

THz Imaging: We used conventional THz imaging to measure the beam properties of the transmitted THz radiation.[25] Here the photodiode after the detection ZnTe crystal was replaced with a CCD camera (Princeton Instruments TE/CCD 512 BKM). The pixels were binned to form a 128 × 128 pixel array, which allowed for greater dynamic range in the measurements. This corresponds to taking 16,384 independent time-domain waveforms simultaneously. The waveforms obtained for each effective pixel were then Fourier transformed and the magnitudes of the amplitude spectra at 0.22 THz were recorded and plotted to form the false color beam profiles.

Acknowledgements

B. Gupta and S. Pandey contributed equally to this work. This work was supported by the NSF MRSEC program at the University of Utah under grant # DMR 1121252.

Received: January 16, 2014
Revised: February 14, 2014
Published online: March 7, 2014

[1] H. Raether, Surface Plasmons on Smooth and Rough Surfaces and on Gratings, Springer-Verlag, Berlin **1988**.
[2] T. W. Ebbesen, H. J. Lezec, H. F. Ghaemi, T. Thio, P. A. Wolff, *Nature* **1998**, *391*, 667.
[3] T. Matsui, A. Agrawal, A. Nahata, Z. V. Vardeny, *Nature* **2007**, *446*, 517.
[4] M. Stockman, *Phys. Rev. Lett.* **2004**, *93*, 137404.
[5] S. Maier, S. Andrews, L. Martín-Moreno, F. García-Vidal, *Phys. Rev. Lett.* **2006**, *97*, 176805.
[6] J. A. Dionne, K. Diest, L. A. Sweatlock, H. A. Atwater, *Nano Lett.* **2009**, *9*, 897.
[7] F. Rana, *IEEE Trans. Nanotechnol.* **2008**, *7*, 91.
[8] M. Liu, X. Yin, E. Ulin-Avila, B. Geng, T. Zentgraf, L. Ju, F. Wang, X. Zhang, *Nature* **2011**, *474*, 64.
[9] J. Wang, S. Liu, Z. V. Vardeny, A. Nahata, *Opt. Express* **2012**, *20*, 2346.
[10] R. Singh, A. K. Azad, J. F. O'Hara, A. J. Taylor, W. Zhang, *Opt. Lett.* **2008**, *33*, 1506.
[11] Z. Tian, R. Singh, J. Han, J. Gu, Q. Xing, J. Wu, W. Zhang, *Opt. Lett.* **2010**, *35*, 3586.
[12] J. Gómez Rivas, C. Schotsch, P. Haring Bolivar, H. Kurz, *Phys. Rev. B* **2003**, *68*, 201306.
[13] E. Hendry, F. Garcia-Vidal, L. Martin-Moreno, J. Rivas, M. Bonn, A. Hibbins, M. Lockyear, *Phys. Rev. Lett.* **2008**, *100*, 123901.
[14] T. Matsui, Z. V. Vardeny, A. Agrawal, A. Nahata, R. Menon, *Appl. Phys. Lett.* **2006**, *88*, 071101.
[15] L. Yang, A. Rida, R. Vyas, M. M. Tentzeris, *IEEE Trans. Microwave Theor. Tech.* **2007**, *55*, 2894.
[16] S. R. Forrest, *Nature* **2004**, *428*, 911.
[17] H. Sirringhaus, T. Kawase, R. H. Friend, T. Shimoda, M. Inbasekaran, W. Wu, E. P. Woo, *Science* **2000**, *290*, 2123.
[18] M. Walther, A. Ortner, H. Meier, U. Löffelmann, P. J. Smith, J. G. Korvink, *Appl. Phys. Lett.* **2009**, *95*, 251107.
[19] K. Takano, T. Kawabata, C.-F. Hsieh, K. Akiyama, F. Miyamaru, Y. Abe, Y. Tokuda, R.-P. Pan, C.-L. Pan, M. Hangyo, *Appl. Phys. Express* **2010**, *3*, 016701.
[20] D. J. Griffiths, Introduction to Electrodynamics, Prentice Hall, Upper Saddle River, NJ, USA **1999**.
[21] S. Pandey, S. Liu, B. Gupta, A. Nahata, *Photon. Res.* **2013**, *1*, 148.
[22] Y.-S. Jin, G.-J. Kim, S.-G. Jeon, *J. Kor. Phys. Soc.* **2006**, *49*, 513.
[23] D. Grischkowsky, S. Keiding, M. Van Exter, C. Fattinger, *J. Opt. Soc. Am. B* **1990**, *7*, 2006.
[24] A. Nahata, A. S. Weling, T. F. Heinz, *Appl. Phys. Lett.* **1996**, *69*, 2321.
[25] Q. Wu, T. D. Hewitt, X.-C. Zhang, *Appl. Phys. Lett.* **1996**, *69*, 1026.

CHAPTER 4

TERAHERTZ PLASMONIC WAVEGUIDES CREATED VIA 3D PRINTING

Terahertz plasmonic waveguides created via 3D printing

Shashank Pandey,[1] Barun Gupta,[2] and Ajay Nahata[1,*]

[1]*Department of Electrical and Computer Engineering, University of Utah, Salt Lake City, Utah 84112, USA*
[2]*Department of Physics and Astronomy, University of Utah, Salt Lake City, Utah 84112, USA*
[*]*nahata@ece.utah.edu*

Abstract: We demonstrate that 3D printing, commonly associated with the manufacture of large objects, allows for the fabrication of high quality terahertz (THz) plasmonic structures. Using a commercial 3D printer, we print a variety of structures that include abrupt out-of-plane bends and continuously varying bends. The waveguides are initially printed in a polymer resin and then sputter deposited with ~500 nm of Au. This thickness of Au is sufficient to support low loss propagation of surface plasmon-polaritons with minimal impact from the underlying layer, thereby demonstrating a useful approach for fabricating a broad range of plasmonic structures that incorporate complex geometries. Using THz time-domain spectroscopy, we measure the guided-wave properties of these devices. We find that the propagation properties of the guided-wave modes are similar to those obtained in similar conventional metal-based waveguides, albeit with slightly higher loss. This additional loss is attributed to roughness associated with limitations that currently exist in commercial 3D printers.

OCIS codes: (050.6624) Subwavelength structures; (130.2790) Guided waves; (240.6680) Surface plasmons; (300.6495) Spectroscopy, terahertz.

References and Links

1. E. Ozbay, "Plasmonics: Merging photonics and electronics at nanoscale dimensions," Science **311**(5758), 189–193 (2006).
2. J. A. Schuller, E. S. Barnard, W. Cai, Y. C. Jun, J. S. White, and M. L. Brongersma, "Plasmonics for extreme light concentration and manipulation," Nat. Mater. **9**(3), 193–204 (2010).
3. J. B. Pendry, L. Martín-Moreno, and F. J. Garcia-Vidal, "Mimicking surface plasmons with structured surfaces," Science **305**(5685), 847–848 (2004).
4. F. J. Garcia-Vidal, L. Martin-Moreno, and J. B. Pendry, "Surfaces with holes in them: new plasmonic metamaterials," J. Opt. A, Pure Appl. Opt. **7**(2), S97–S101 (2005).
5. S. A. Maier, S. R. Andrews, L. Martín-Moreno, and F. J. García-Vidal, "Terahertz surface plasmon-polariton propagation and focusing on periodically corrugated metal wires," Phys. Rev. Lett. **97**(17), 176805 (2006).
6. A. P. Hibbins, B. R. Evans, and J. R. Sambles, "Experimental verification of designer surface plasmons," Science **308**(5722), 670–672 (2005).
7. A. Agrawal, Z. V. Vardeny, and A. Nahata, "Engineering the dielectric function of plasmonic lattices," Opt. Express **16**(13), 9601–9613 (2008).
8. M. Tonouchi, "Cutting-edge terahertz technology," Nat. Photonics **1**(2), 97–105 (2007).
9. R. Mendis and D. Grischkowsky, "Undistorted guided-wave propagation of subpicosecond terahertz pulses," Opt. Lett. **26**(11), 846–848 (2001).
10. J. A. Harrington, R. George, P. Pedersen, and E. Mueller, "Hollow polycarbonate waveguides with inner Cu coatings for delivery of terahertz radiation," Opt. Express **12**(21), 5263–5268 (2004).
11. K. Wang and D. M. Mittleman, "Metal wires for terahertz wave guiding," Nature **432**(7015), 376–379 (2004).
12. W. Zhu, A. Agrawal, and A. Nahata, "Planar plasmonic terahertz guided-wave devices," Opt. Express **16**(9), 6216–6226 (2008).
13. D. Martin-Cano, M. L. Nesterov, A. I. Fernandez-Dominguez, F. J. Garcia-Vidal, L. Martin-Moreno, and E. Moreno, "Domino plasmons for subwavelength terahertz circuitry," Opt. Express **18**(2), 754–764 (2010).
14. W. Zhao, O. M. Eldaiki, R. Yang, and Z. Lu, "Deep subwavelength waveguiding and focusing based on designer surface plasmons," Opt. Express **18**(20), 21498–21503 (2010).
15. G. Kumar, S. Pandey, A. Cui, and A. Nahata, "Planar plasmonic terahertz waveguides based on periodically corrugated films," New J. Phys. **13**(3), 033024 (2011).

16. X. Gao, J. H. Shi, X. Shen, H. F. Ma, W. X. Jiang, L. Li, and T. J. Cui, "Ultrathin dual-band surface plasmonic polariton waveguide and frequency splitter in microwave frequencies," Appl. Phys. Lett. **102**(15), 151912 (2013).
17. Z. Wu, J. Kinast, M. E. Gehm, and H. Xin, "Rapid and inexpensive fabrication of terahertz electromagnetic bandgap structures," Opt. Express **16**(21), 16442–16451 (2008).
18. Z. Wu, W.-R. Ng, M. E. Gehm, and H. Xin, "Terahertz electromagnetic crystal waveguide fabricated by polymer jetting rapid prototyping," Opt. Express **19**(5), 3962–3972 (2011).
19. J. Liu, R. Mendis, and D. M. Mittleman, "A Maxwell's fish eye lens for the terahertz region," Appl. Phys. Lett. **103**(3), 031104 (2013).
20. X. Shou, A. Agrawal, and A. Nahata, "Role of metal film thickness on the enhanced transmission properties of a periodic array of subwavelength apertures," Opt. Express **13**(24), 9834–9840 (2005).
21. A. Nahata and W. Zhu, "Electric field vector characterization of terahertz surface plasmons," Opt. Express **15**(9), 5616–5624 (2007).
22. T. Matsui, A. Agrawal, A. Nahata, and Z. V. Vardeny, "Transmission resonances through aperiodic arrays of subwavelength apertures," Nature **446**(7135), 517–521 (2007).

1. Introduction

In contrast to naturally occurring materials, where the atomic and molecular substituents of the materials determine its physical properties, artificially structured materials offer the ability to engineer the physical properties of the resulting medium based on the geometrical properties of the imprinted pattern. In the field of plasmonics, such texturing allows for control over electromagnetic waves bound to the interface between a metal and the adjacent dielectric medium [1,2]. These surface plasmon-polaritons (SPPs) display unique dispersion characteristics that depend upon the plasma frequency of the medium. In the long wavelength regime, where metals are highly conductive, it has been shown, both theoretically [3–5] and experimentally [6,7], that such texturing can create an effective medium that can be characterized by an effective plasma frequency that is determined by the geometrical parameters of the surface structure.

The terahertz (THz) spectral range offers unique opportunities to utilize such materials. While there has been significant work on developing coherent sources and detectors, relatively few other device technologies currently exist [8]. A major issue that has constrained this development is the fact that most conventional dielectrics and semiconductors are highly lossy in this spectral range. Since metals are highly conductive, SPPs experience very low propagation loss when air acts as the adjacent dielectric medium. One representative device structure where this has been well demonstrated is in the area of THz waveguides. Over the last decade, a broad range of metal-based waveguides has been developed [9–16]. Recently, we showed that a one-dimensional array of rectangular apertures that either partially or completely perforate a planar metal film could be used to create a variety of guided-wave devices [12,15]. In fact, using this approach, we have fabricated not only straight and curved waveguides, but also y-splitters and 3 dB couplers. While the fabrication approach used in those implementations is promising for developing other types of guided-wave structures, it is a time-consuming process that is generally limited to planar geometries. As an example, in the case of blind aperture-based waveguides, the final structure requires the bonding of three separate layers, in which one layer requires laser ablation. Therefore, the development of relatively easy fabrication techniques to create non-planar guided-wave devices may create new opportunities in a variety of emerging THz applications.

In this submission, we demonstrate the use of conventional 3D printing to create both planar and non-planar THz plasmonic waveguides. While 3D printing has been used extensively to print large objects, the use of 3D printing for THz devices has not been well studied, although a few examples exist [17–19]. The devices discussed here are printed using a professional-grade commercially available 3D printer in a polymer resin and then subsequently overcoated with a thin layer of Au, allowing the structure to support SPPs. Using this approach, we fabricate and characterize a variety of geometries that cannot easily be fabricated using other conventional techniques. We use THz time-domain spectroscopy (THz-TDS) to fully characterize the propagation properties of the waveguides and compare them to devices that have previously been fabricated in conventional metals.

rectangular blind holes (rectangular holes that do not perforate the medium) as the basis for the device topology. These blind holes had design dimensions of s = 550 μm, a = 150 μm, h = 450 μm, and d = 250 μm. The devices were typically fabricated to have a total length of 10 cm. Compared to the wavelength (λ) of the lowest order mode, discussed below, the aperture width was ~λ/7 and the periodicity was ~λ/4, indicating that we were operating in the long wavelength limit.

We used a modified THz time-domain spectroscopy setup to characterize the propagation properties of SPPs on these devices. Although the details related to the experimental apparatus have been discussed elsewhere [21], we briefly present them here. We used a 1 mm thick <110> ZnTe crystal for generation of broadband THz pulses. This radiation was collected and collimated using an off axis parabolic mirror. We then used a 150 mm focal length TPX (polymethylpentene) lens to focus the THz radiation onto the input coupler at normal incidence. After propagation along the surface, the THz SPPs were measured using a second 1 mm thick <110> ZnTe crystal via electro-optic sampling [21]. Because of the crystal orientation and the polarization of both the optical probe and THz SPP beams, we were only sensitive to the E_z component of the surface field. By moving the optical probe beam and electro-optic crystal relative to the surface of the patterned structure, we were able to measure the spatial distribution and loss properties of the propagating modes.

3. Experimental results and discussion

We begin by describing the spectral and spatial properties of a planar straight waveguide fabricated using 3D printing. In Fig. 2(a), we show the experimentally measured waveguide transmission spectrum obtained at the end of a 10 cm long linear waveguide. There are several notable features in the spectrum. First, it is apparent that there are three separate modes, each with its own distinct dip (anti-resonance frequency). These appear at 0.27, 0.47 and 0.54 THz. As we have discussed earlier, these dips on the high frequency side of each resonance are the relevant parameter, not the frequencies associated with the resonance peaks [22]. Thus, the locations of the anti-resonant frequencies can be viewed as *effective* cavity resonance frequencies of the individual apertures. These frequencies are approximately given by [15]

$$\nu_{mnp} = \frac{c}{2\pi}\sqrt{\left(\frac{m\pi}{s}\right)^2 + \left(\frac{n\pi}{a}\right)^2 + \left(\frac{(p+0.25)\pi}{h}\right)^2} \qquad (1)$$

where, m, n, and p are integers (m = 1,2,3… and n,p = 0,1,2…) and c is the speed of light in vacuum.. In the case of blind holes, we previously showed that the conventional description for the cavity modes required that the value of p be offset by 0.25. This modification may be the result of having an asymmetric rectangular cavity (i.e. a bottom metal surface and open on top). With this refinement, the lowest order anti-resonance frequency can still be indexed as m = 1, n = 0, and p = 0. In order to fit the anti-resonance frequencies to Eq. (1), a slight adjustment in the blind hole dimensions is necessary to achieve good agreement. Specifically, we use s = 560 μm instead of the design value of s = 550 μm and h = 470 μm instead of the design value of h = 450 μm. Since n = 0 for all three modes, the exact value of blind hole width, a, is not critical. Given the details of the printing process, the need for making such small changes in the geometrical parameters is not surprising. With these modified values, the frequencies associated with the anti-resonance frequencies obtained from Eq. (1) are 0.28 THz for the (100) mode, 0.48 THz for the (101) mode and 0.54 THz for the (200) mode, which is in good agreement with the experimental data. Modes that operate beyond the Bragg frequency, $\nu_B = c/2d = 0.6$ THz are strongly damped, as demonstrated in the spectrum.

In all of the subsequent data, we describe only the propagation properties of the lowest order mode. Specifically, we show the magnitude of the E_z component of the THz electric field taken at the peak of the lowest order mode (0.27 THz). In Fig. 2(b), we show the loss properties for propagation along the waveguide. An exponential fit to the data yields a loss parameter of 0.17 cm^{-1}, corresponding to a 1/e propagation length of ~5.9 cm. In Fig. 2(c), we

2. Experimental details

We fabricated a variety of guided-wave structures using an Objet EDEN 260V 3D printer, including straight waveguides, 3D bends, 3D y-splitters and U-shaped structures. The printer had a resolution of 600 dpi along the x- and y-axes and 1600 dpi along the z-axis. The structures were printed using a Vero White polymer resin onto a plastic printing platform. After printing, the resin solidified as a rigid white opaque plastic. In general, the total printing time was volume dependent. However, for the structures described here, the printing time was typically on the order of an hour. After detaching the device from the support platform, we sputter deposited ~500 nm of Au. Sputter deposition allowed for metal deposition on all surfaces, including inside the blind holes. Nevertheless, there may be some non-uniformity in the Au thickness, particularly on the sidewalls of the rectangular blind holes. Based on measurements using larger equivalent structures, we estimate that the minimum Au thickness on any surface is at least 300 nm. We have previously shown that once the metal thickness is greater than approximately two skin depths (δ~150 nm at THz frequencies), the properties of the surface waves are determined by the properties of the top metal film [20]. Thus, SPPs launched on the metal surface have minimal interaction with the underlying medium, allowing for waveguide fabrication that is independent of the fabrication medium.

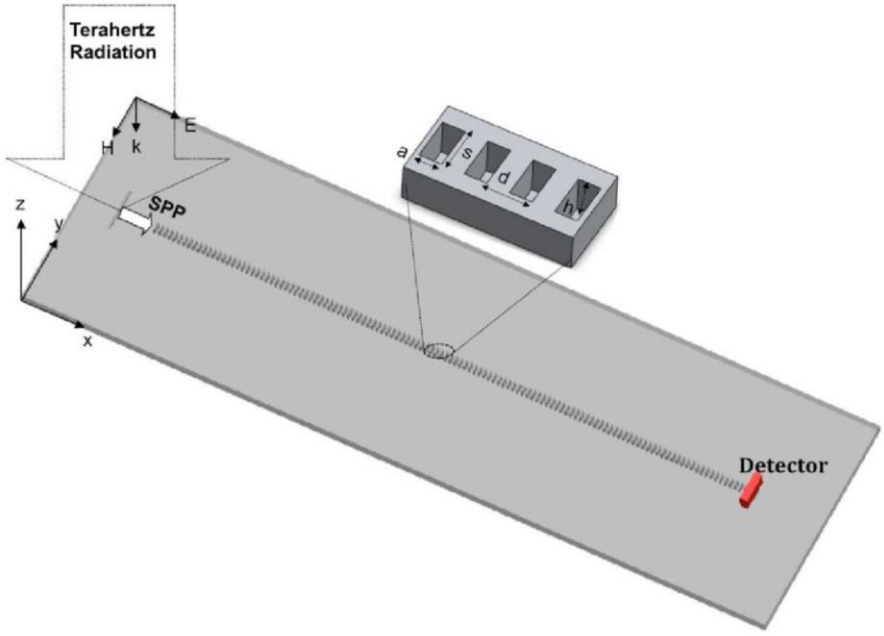

Fig. 1. Schematic drawing of the printed THz waveguide, including the excitation and detection scheme. The groove at the input end is used to couple normally incident broadband THz radiation to SPPs. For detection purposes, the optical probe beam propagates parallel to the THz guided-wave SPPs. A <110> ZnTe crystal is used for coherent detection of the E_z component of the guided-wave SPP. The design dimensions of the rectangular blind holes are: length s = 550 µm, width a = 150 µm, depth h = 450 µm, and periodicity d = 250 µm.

In Fig. 1, we show a schematic diagram of a planar guided-wave structure, along with the corresponding excitation and detection scheme and blind aperture dimensions. In order to couple freely propagating THz radiation into SPPs, we fabricated a 1 mm long, 300 µm wide by 100 µm deep straight groove into a 1 mm thick stainless steel metal piece. This groove was physically abutted against the waveguides and allowed for reproducible coupling from device to device (not shown). All of the waveguide devices described here utilized

show the magnitude of the E_z field component as a function of distance above the waveguide surface (along the z-axis). The field decays exponentially from the metal dielectric interface with a 1/e decay length of ~2.6 mm. Finally, in Fig. 2(d), we show the magnitude of the E_z field component measured along the y-axis of the waveguide, 5 cm from the waveguide input. The lateral field distribution at the cross-section exhibits a Gaussian mode profile with a full-width at half maximum (FWHM) mode size of ~3.4 mm, indicating reasonably tight confinement along the lateral direction. At this point, it is instructive to compare the properties of this printed waveguide, with one that was previously fabricated in stainless steel and using laser ablation to fabricate the blind holes [15]. In that device, the 1/e propagation length along the x-axis was ~12 cm, the 1/e out-of-plane spatial extent of the THz electric field was ~2.5 mm, and the FWHM lateral width of the lowest order guided-wave mode was 2.8 mm. These properties are generally consistent with the fact that the stainless steel waveguide exhibits lower loss.

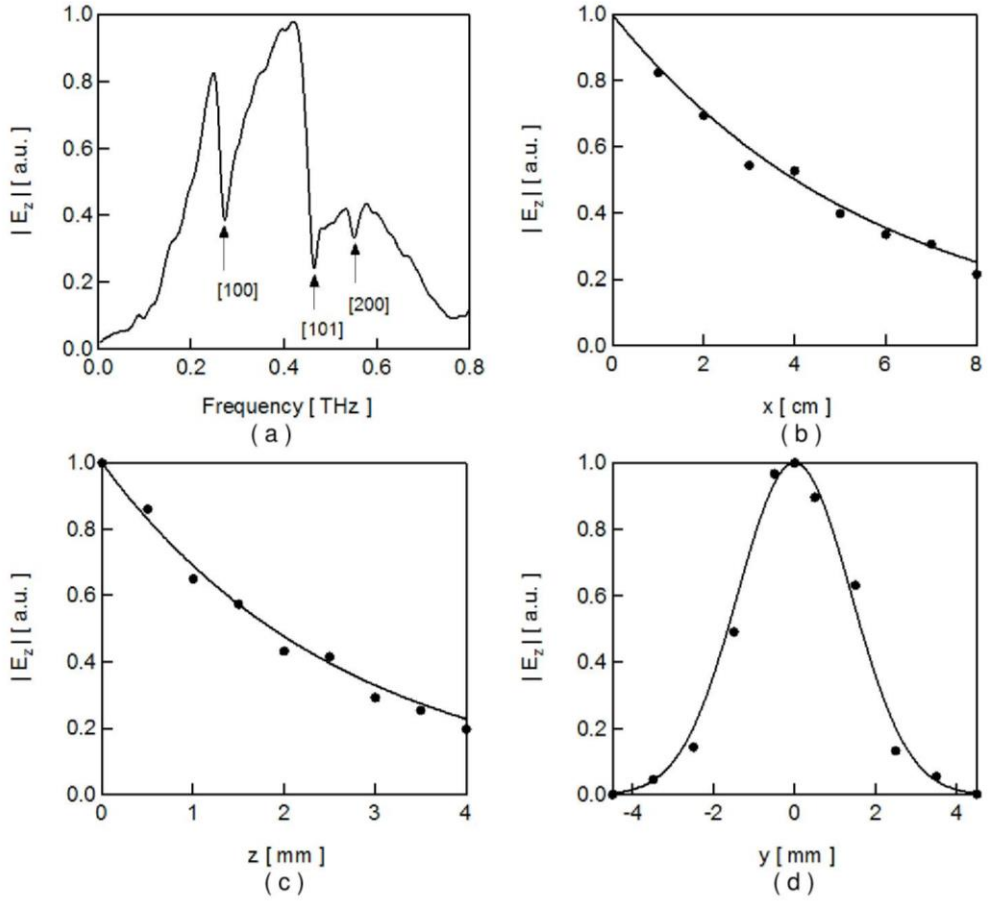

Fig. 2. Propagation properties for a planar straight waveguide with periodically spaced rectangular blind holes. (a) Measured transmission spectrum for the waveguide. The arrows show the anti-resonance frequencies associated with the different effective cavity modes. These dips occur at 0.27, 0.47 and 0.54 THz. (b) The field amplitude $|E_z|$ measured along the x-axis at different positions along the length of the waveguide. The dots represent the measured field value normalized to the value at the input. The black line is an exponential fit to the data, corresponding to a 1/e decay length of ~5.9 cm. (c) The $|E_z|$ component of the electric field measured along the z-axis at different heights above the sample surface. The dots represent the measured field value normalized to the value at the surface. The black line is an exponential fit to the data, corresponding to a 1/e decay length of 2.6 mm. (d) The $|E_z|$ component of the electric field measured along the y-axis 5 cm from the waveguide input. The dots represent the measured value, while the black trace is a Gaussian fit to the data, yielding a (FWHM) width of ~3.4 mm.

of-plane bends, the two output arms are vertically offset from one another by ~7 mm and horizontally offset from one another by 11 mm.

We measured $|E_z|$ along the output face of the device, as shown in Fig. 4(c). Because the two output arms are at different vertical heights, with the right arm lower than the input to the Y-splitter, we had to make two separate measurements to obtain the lateral guided-wave properties of the device. Since the left arm is vertically higher than the input, the measurement is straightforward, in terms of having the THz SPP and the optical probe beam co-propagate. For the right arm, the optical probe beam is made to co-propagate with the THz SPP only over the last 2 cm of the device. We use a thin (100 µm) sapphire slide that has a high reflection coating optimized for 800 nm. The THz data for the right arm is corrected for the reflection associated with the sapphire mirror. We fit the experimentally measured data for both arms to Gaussian functions and found that the FWHM widths were 3.53 and 3.48 mm, respectively, which is in good agreement with the mode size shown in Fig. 2(b).

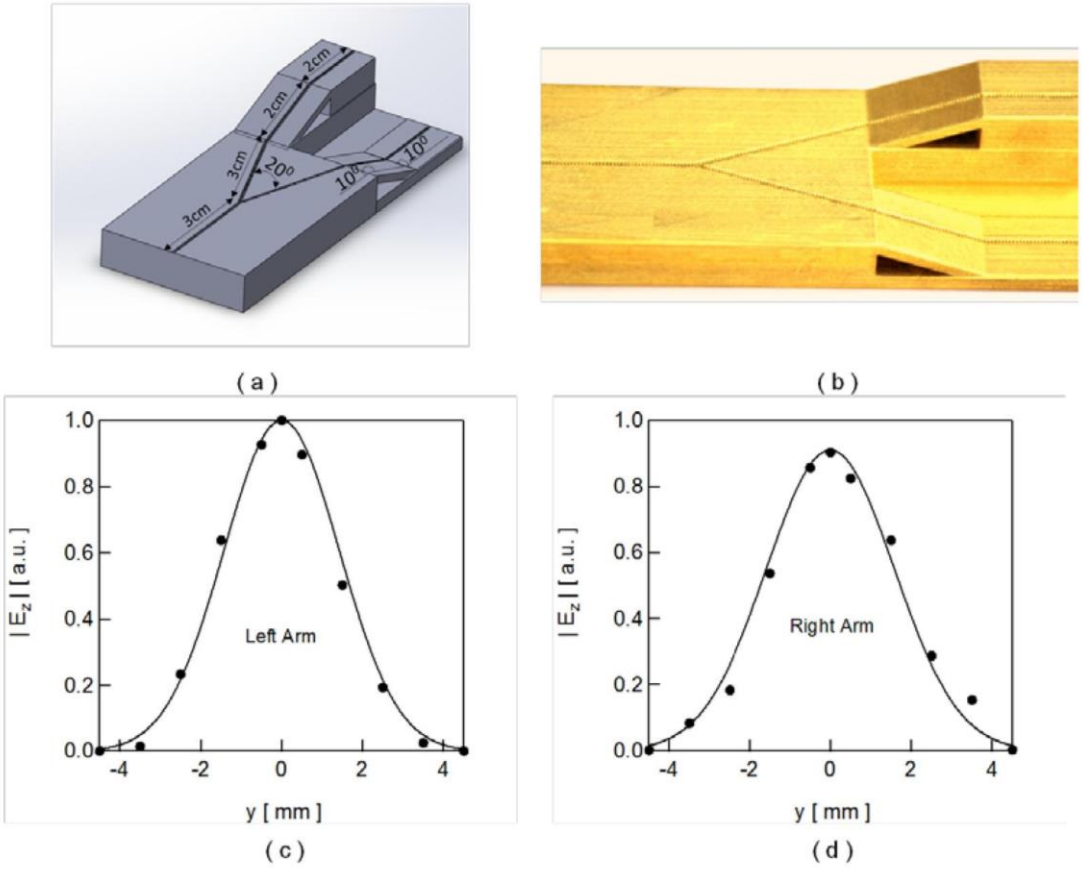

Fig. 4. Properties of a 3D Y-splitters. (a) Schematic diagram of a 10 cm long Y-splitter, in which the two arms branch off both in-plane and out-of-plane. In both cases, the branches are at ± 10 ° relative to the preceding waveguide. (b) Image of the Y splitter after sputter deposition with Au. (c) & (d) The field amplitude |Ez| along y-axis at the end of the Y-splitter for both arms of the waveguide. The black dots correspond to experimental data and the solid black traces are fits to the experimental data using Gaussian functions. The FWHM widths are ~3.5 mm for both arms.

Finally, in order to more fully demonstrate the utility of 3D printing for fabricating THz devices, we fabricated a series of curved waveguides that incorporate a U-shaped arc. In Figs. 5(a) and 5(b), we show a schematic diagram of the general structure and a photograph of several finished devices, respectively. Each of the devices is 60 mm in total length and includes 5 mm long planar sections (sections A-B and F-G in the schematic) on the input and output side that allow for coupling of THz radiation into the device and placement of the

detection crystal at the output. The central portion of the curve (section C-D-E) incorporates an arc that varies between 5 mm and 15 mm. In order to connect the arc (section C-D-E) with the planar sections (sections A-B and F-G), the intervening sections (B-C and E-F) are required to change geometry in order to maintain a smoothly varying curve. Thus, measurements are reported not in terms of radius of curvature, but rather the total vertical depth change, H. In Fig. 5(c), we show the excess loss for each structure, once the propagation loss associated with a 6 cm straight waveguide, found in Fig. 2, has been subtracted. As expected, the excess loss increases with increasing depth.

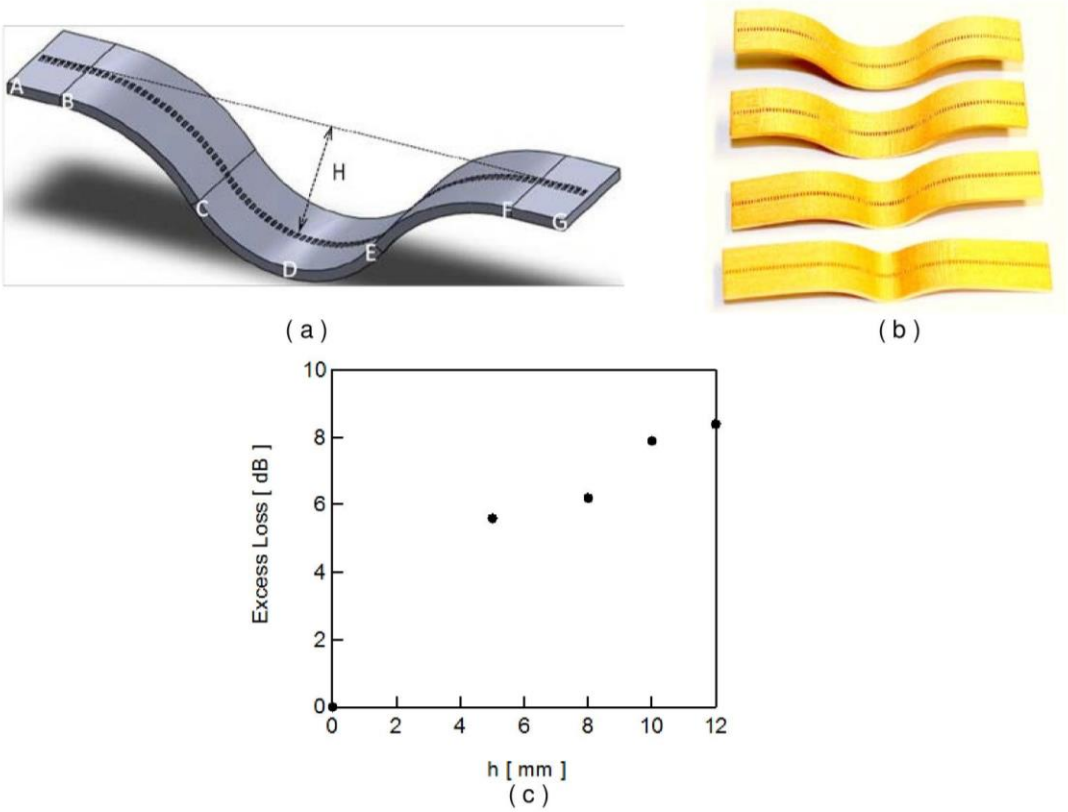

Fig. 5. Properties of 3D curved waveguides. (a) Schematic drawing of the 60 mm long curved waveguide with the various sections delineated. The input (A-B) and output (F-G) sections are 5 mm long planar waveguides used to facilitate input coupling and detection of the guided wave at the out put. The central arc (C-D-E) has a radius of curvature that varies between 5 mm and 15 mm. The connecting sections (B-C and E-F) are adjustable to ensure a smoothly varying curve. (b) Images of the four fabricated devices. (c) Measured excess loss as a function of the depth, H.

4. Conclusion

In conclusion, we have demonstrated experimentally that conventional 3D printing is well suited for fabricating THz plasmonic devices. We made a variety of different devices, including straight waveguides, 3D bends, 3D Y-splitters and curved waveguides. Although the basic structures described here were printed in a polymer resin, once they were coated with a metal layer that was sufficiently thick, they supported relatively low loss propagation of SPPs. In straight waveguides, we observed a propagation loss parameter of 0.17 cm^{-1}, corresponding to a 1/e propagation length of 5.9 cm. This loss is higher than was observed with waveguides fabricated using conventional metal foils [15]. We attribute the higher loss in the printed devices to greater surface roughness that results from the printing process. In devices that included abrupt out-of-plane bends and continuously varying bends, we measured an excess loss associated with those geometries that increases with increasing

angle. In the former case, for example, a 10° abrupt out-of-plane bend resulted in an excess loss of ~2 dB and increased with increasing angle. We have discussed only a few select geometries here. However, the fabrication approach can be used to make a broad range of artificially structured materials. Ongoing advances in printing technology are likely to have significant impact on the utilization of this technique.

Acknowledgments

This work was supported by the NSF MRSEC program at the University of Utah under grant # DMR 1121252.

CHAPTER 5

PLASMONIC WAVEGUIDES BASED ON SYMMETRIC AND ASYMMETRIC STRUCTURES

Plasmonic waveguides based on symmetric and asymmetric T-shaped structures

Barun Gupta, Shashank Pandey, and Ajay Nahata*

Department of Electrical and Computer Engineering, University of Utah, Salt Lake City, Utah 84112, USA
*nahata@ece.utah.edu

Abstract: We describe the fabrication and characterization of plasmonic waveguides based on a periodic one-dimensional array of symmetric and asymmetric T-shaped structures. The devices are fabricated in a polymer resin using conventional 3D printing and subsequently overcoated with ~500 nm of Au. Using terahertz (THz) time-domain spectroscopy, we systematically measure the guided-wave transmission properties of the devices as a function of the different geometrical parameters. Through these measurements, we find that the resonance frequency associated with the lowest order mode depends primarily on the structure height and the cap width and appears to be independent of its lateral width. We also perform numerical simulations using the same geometrical parameters and find excellent agreement between experiment and simulation. We fabricate a waveguide in which the lateral width of the T-shaped structures is tapered in a linear fashion. While the spectrum of this device is similar to one without tapering, we observe relatively little reduction in the mode size, even as the structure width is reduced by a factor of eight.

OCIS codes: (050.6624) Subwavelength structures; (130.2790) Guided waves; (240.6680) Surface plasmons; (300.6495) Spectroscopy, terahertz.

References and links

1. M. Tonouchi, "Cutting-edge terahertz technology," Nat. Photonics **1**(2), 97–105 (2007).
2. G. Gallot, S. P. Jamison, R. W. McGowan, and D. Grischkowsky, "Terahertz waveguides," J. Opt. Soc. Am. B **17**(5), 851–863 (2000).
3. R. Mendis and D. Grischkowsky, "Undistorted guided-wave propagation of subpicosecond terahertz pulses," Opt. Lett. **26**(11), 846–848 (2001).
4. M. Wächter, M. Nagel, and H. Kurz, "Metallic slit waveguide for dispersion-free low-loss terahertz signal transmission," Appl. Phys. Lett. **90**(6), 061111 (2007).
5. R. W. McGowan, G. Gallot, and D. Grischkowsky, "Propagation of ultrawideband short pulses of terahertz radiation through submillimeter-diameter circular waveguides," Opt. Lett. **24**(20), 1431–1433 (1999).
6. J. A. Harrington, R. George, P. Pedersen, and E. Mueller, "Hollow polycarbonate waveguides with inner Cu coatings for delivery of terahertz radiation," Opt. Express **12**(21), 5263–5268 (2004).
7. K. Wang and D. M. Mittleman, "Metal wires for terahertz wave guiding," Nature **432**(7015), 376–379 (2004).
8. S. P. Jamison, R. W. McGowan, and D. Grischkowsky, "Single-mode waveguide propagation and reshaping of sub-ps terahertz pulses in sapphire fibers," Appl. Phys. Lett. **76**(15), 1987–1989 (2000).
9. L. J. Chen, H. W. Chen, T. F. Kao, J. Y. Lu, and C. K. Sun, "Low-loss subwavelength plastic fiber for terahertz waveguiding," Opt. Lett. **31**(3), 308–310 (2006).
10. C. S. Ponseca, Jr., R. Pobre, E. Estacio, N. Sarukura, A. Argyros, M. C. Large, and M. A. van Eijkelenborg, "Transmission of terahertz radiation using a microstructured polymer optical fiber," Opt. Lett. **33**(9), 902–904 (2008).
11. H. Raether, *Surface Plasmons on Smooth and Rough Surfaces and on Gratings*, Vol. 111 of Springer Tracts in Modern Physics (Springer, 1988).
12. W. Zhu, A. Agrawal, and A. Nahata, "Planar plasmonic terahertz guided-wave devices," Opt. Express **16**(9), 6216–6226 (2008).
13. C. R. Williams, S. R. Andrews, S. A. Maier, A. I. Fernández-Domínguez, L. Martín-Moreno, and F. J. García-Vidal, "Highly confined guiding of terahertz surface plasmon polaritons on structured metal surfaces," Nat. Photonics **2**(3), 175–179 (2008).
14. J. B. Pendry, L. Martín-Moreno, and F. J. Garcia-Vidal, "Mimicking surface plasmons with structured surfaces," Science **305**(5685), 847–848 (2004).
15. A. P. Hibbins, B. R. Evans, and J. R. Sambles, "Experimental verification of designer surface plasmons," Science **308**(5722), 670–672 (2005).

16. G. Kumar, S. Pandey, A. Cui, and A. Nahata, "Planar plasmonic terahertz waveguides based on periodically corrugated metal films," New J. Phys. **13**(3), 033024 (2011).
17. G. Kumar, A. Cui, S. Pandey, and A. Nahata, "Planar terahertz waveguides based on complementary split ring resonators," Opt. Express **19**(2), 1072–1080 (2011).
18. A. I. Fernández-Domínguez, E. Moreno, L. Martín-Moreno, and F. J. García-Vidal, "Terahertz wedge plasmon polaritons," Opt. Lett. **34**(13), 2063–2065 (2009).
19. C. R. Williams, M. Misra, S. R. Andrews, S. A. Maier, S. Carretero-Palacios, S. G. Rodrigo, F. J. Garcia-Vidal, and L. Martin-Moreno, "Dual band terahertz waveguiding on a planar metal surface patterned with annular holes," Appl. Phys. Lett. **96**(1), 011101 (2010).
20. D. Martin-Cano, M. L. Nesterov, A. I. Fernandez-Dominguez, F. J. Garcia-Vidal, L. Martin-Moreno, and E. Moreno, "Domino plasmons for subwavelength terahertz circuitry," Opt. Express **18**(2), 754–764 (2010).
21. Z. Gao, X. Zhang, and L. Shen, "Wedge mode of spoof surface plasmon polaritons at terahertz frequencies," J. Appl. Phys. **108**(11), 113104 (2010).
22. D. Martin-Cano, O. Quevedo-Teruel, E. Moreno, L. Martin-Moreno, and F. J. Garcia-Vidal, "Waveguided spoof surface plasmons with deep-subwavelength lateral confinement," Opt. Lett. **36**(23), 4635–4637 (2011).
23. G. Kumar, S. Li, M. M. Jadidi, and T. E. Murphy, "Terahertz surface plasmon waveguide based on a one-dimensional array of silicon pillars," New J. Phys. **15**(8), 085031 (2013).
24. X. Shen and T. J. Cui, "Planar plasmonic metamaterial on a thin film with nearly zero thickness," Appl. Phys. Lett. **102**(21), 211909 (2013).
25. W. Zhao, O. M. Eldaiki, R. Yang, and Z. Lu, "Deep subwavelength waveguiding and focusing based on designer surface plasmons," Opt. Express **18**(20), 21498–21503 (2010).
26. S. Pandey, B. Gupta, and A. Nahata, "Terahertz plasmonic waveguides created via 3D printing," Opt. Express **21**(21), 24422–24430 (2013).
27. X. Shou, A. Agrawal, and A. Nahata, "Role of metal film thickness on the enhanced transmission properties of a periodic array of subwavelength apertures," Opt. Express **13**(24), 9834–9840 (2005).
28. A. Nahata, A. S. Weling, and T. F. Heinz, "A wideband coherent terahertz spectroscopy system using optical rectification and electro-optic sampling," Appl. Phys. Lett. **69**(16), 2321–2323 (1996).
29. A. Nahata and W. Zhu, "Electric field vector characterization of terahertz surface plasmons," Opt. Express **15**(9), 5616–5624 (2007).
30. T. Matsui, A. Agrawal, A. Nahata, and Z. V. Vardeny, "Transmission resonances through aperiodic arrays of subwavelength apertures," Nature **446**(7135), 517–521 (2007).

1. Introduction

The ability to control the propagation properties of optical radiation is one of the fundamental goals of optics. Waveguides offer a powerful solution to this goal, since they allow for point-to-point transport across potentially complex geometries. In the terahertz (THz) spectral range, defined as extending from 100 GHz to 30 THz [1], the progress in developing such devices has been dramatically slower. The difficulty, in large part, lies in the fact that many conventional dielectrics and semiconductors are highly lossy in this frequency regime. Nevertheless, a number of interesting implementations have been developed [2]. Many of these device geometries have been inspired by existing microwave and optical waveguides. In the former category, for example, a variety of metal-based waveguides, including parallel plate waveguides [3], slot waveguides [4], hollow cylindrical waveguides [5,6] and single metal wires [7] have been shown to allow for low loss and, in some cases, low dispersion [3,4,7] propagation. In the latter category, a number of different dielectric-based waveguide implementations have been described, including solid core dielectric waveguides [8,9] and plastic microstructured waveguides [10].

In recent years, an alternative approach based on guiding surface plasmon-polaritons (SPPs) [11] on structured metal films has been pursued. In the earliest implementations, the metal was etched with rectangular holes to form either one-dimensional [12] or two-dimensional [13] structured surfaces. In general, tailoring the surface structure of a metal can dramatically alter the dispersion properties of propagating bound electromagnetic waves [12,14,15]. In the case of waveguides that are based on holes that either partially [13,16] or completely perforate the metal film [12,17], the longest aperture dimension, usually transverse to the propagation direction, determines the frequency of the lowest order propagating mode. Subsequently, a number of interesting theoretical and experimental studies have examined a variety of other geometries that allow for low loss THz guided-wave propagation [18–24]. Among these, there are a number of proposals that rely on building different metallic shapes on a metal surface. A unique aspect of two of these geometries is the fact that the in-plane transverse dimension does not affect which frequencies are guided

[20,22]. Waveguides based on such architectures may allow for focusing of radiation, by simply tapering the transverse dimension of the structures along the propagation axis. Of the two geometries, only the domino structure has been examined experimentally at microwave [25] and THz [23] frequencies. While the domino structures are interesting, waveguides based on inverse-L shaped structures [21], and variations of that geometry, have been predicted to allow for tighter confinement of the propagating wave. This may be useful for tightly focusing the guided mode, as mentioned above, and allow for better performance on curved geometries.

In this submission, we fabricate and characterize a family of waveguides that have been predicted to allow for higher lateral confinement than all other predicted geometries. The devices consist of one-dimensional arrays of symmetric or asymmetric metallic T-shaped structures fabricated on a metalized substrate. Given the significant complexity in fabricating such structures using conventional lithographic techniques, we extend our recent work on 3D printing of plasmonic structures to fabricate these devices [26]. The symmetric structures are T-shaped, while the most extreme asymmetric structures have the shape of an inverted L. Using THz time-domain spectroscopy, we measure the transmission spectrum and other guided-wave properties of the devices as a function of the structure height, lateral width, asymmetry and periodicity. We also perform 3D numerical finite-difference time-domain (FDTD) simulations to validate our observations. Experimentally and numerically, we find that the lowest order resonance is defined only by the height and longitudinal overhang in the individual structures, thus confirming that the resonance frequencies are independent of the lateral width. Such a finding would suggest that laterally tapered waveguides based on these structures would be well suited to strongly focus the guided THz radiation. However, in contrast to theory and numerical simulations, we find that tapered waveguides do not concentrate THz radiation very strongly. We discuss the reasons for this.

2. Experimental details

In Fig. 1(a), we show a schematic diagram of a representative T-shaped waveguide. The individual structures are composed of two parts: a lower support that has a height of h_1 and a width of g and an upper structure that has a height of h_2 and total width, along the waveguide axis, of w + g, where $w = w_1 + w_2$. Thus, for a symmetric T-structure, $w_1 = w_2 = w/2$, while for the most asymmetric L-shaped structure, $w_1 = 0$ and $w_2 = w$ or $w_1 = w$ and $w_2 = 0$. Each of the individual structures has a lateral width, L, with the spacing between structures given by p, the periodicity. All of the fabricated devices are 7 cm long. Experimentally, the waveguides were made using a commercially available professional grade 3D printer (Object EDEN 260V), which had a printing resolution of 600 dpi in the x-y plane and 1600 dpi along z-axis. The devices were printed using a polymer resin (Vero White) on a support platform. After the resin solidified, the devices were detached from the support and sputter deposited with Au. The measured surface roughness of the printed device was ~3 μm rms, which was substantially larger that the ~50 nm rms surface roughness associated with metal foils that have previously been used to fabricate other plasmonic waveguides [12,16,17]. Among the various deposition techniques, sputtering is the most omnidirectional and allows for more uniform metal coatings on complex non-planar geometries. To ensure that the bottom surfaces of the T or inverted-L structures were coated with Au, we turned the samples multiple times between deposition runs. On the upper (planar) surfaces of the waveguide, the measured Au film thickness was ~500 nm. We have previously shown that the properties of the propagating SPP are determined by the surface metal layer and are independent of the underlying material once the metal thickness is greater than approximately twice the skin depth (δ~150 nm at 0.3 THz frequency) [27]. We do not know the thickness of the Au on the bottom surfaces. However, based on the transmission properties, we do not believe that the metal thickness is sufficiently thin anywhere that it plays a detrimental role in the guided-wave properties. In Figs. 1(b) and 1(c), we present images of the metalized symmetric T and asymmetric inverted-L structures, respectively.

In Fig. 1(a), we also show a simplified excitation and detection scheme to measure the guided-wave properties. We used an amplified ultrafast Ti: Sapphire laser as the optical source for generation and coherent detection of broadband THz radiation using nonlinear optical crystals [28,29]. The output of the laser was split 80:20 to yield the optical pump and probe beams, respectively. Broadband THz radiation was generated using a 1 mm thick <110> ZnTe crystal. This THz radiation was collected using a parabolic mirror and focused onto one end of the waveguide using a 150 mm focal length TPX (polymethyl-pentene) lens. In contrast to earlier work where we used a common input groove to couple freely propagating THz radiation to SPPs, here the (corrugated) structures acted as the input coupler to the waveguide. Regardless of whether we used a groove fabricated into the substrate of the device or the T-shaped structures that sat above the substrate surface, the structured geometry acted to scatter a fraction of the normally incident radiation into SPPs that propagated along the direction of the waveguide. We used a second 1mm thick <110> ZnTe crystal to measure the properties of the propagating SPPs via electro-optic sampling [28,29]. By moving the ZnTe detection crystal to different points along x, y and z-axes, we could measure the propagation properties of the E_z component of the SPP wave anywhere above the surface of the waveguide. While the phase information is important, in the results that follow, we present only the spectral amplitude of E_z, $|E_z|$.

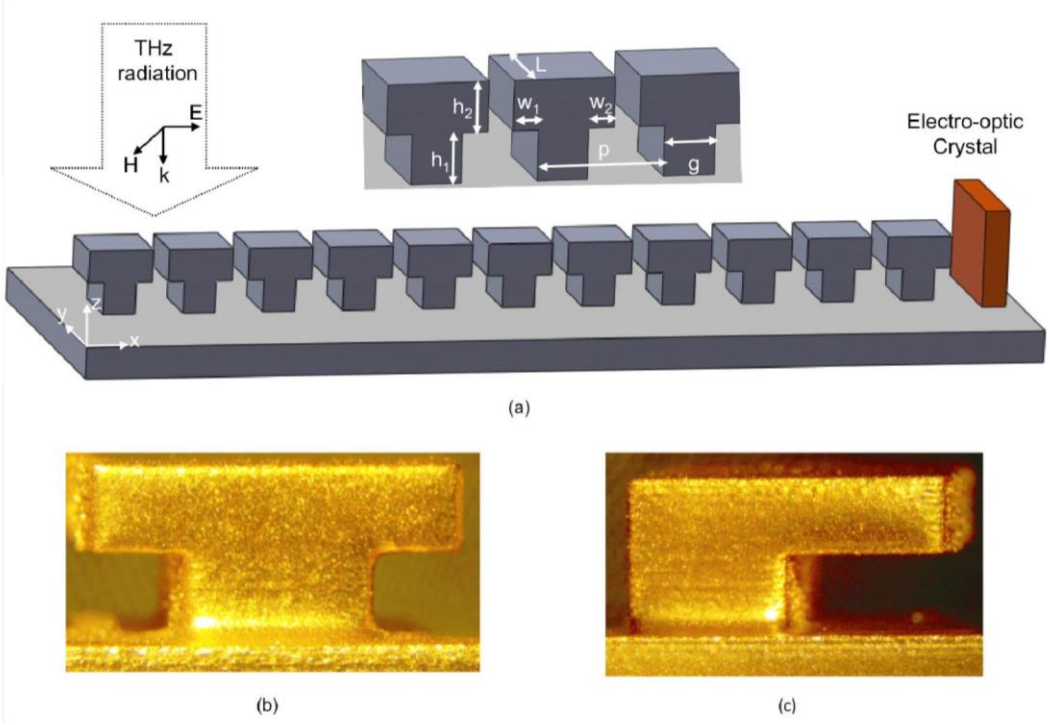

Fig. 1. Waveguide design properties and characterization scheme. (a) Schematic diagram of the waveguide based on symmetric and asymmetric T-shaped structures. The expanded view shows the relevant geometrical parameters. THz radiation, polarized along the x-axis, is normally incident on the device and coupled to SPPs. The properties of the guided-wave THz electric field are measured via electro-optic sampling using a 1 mm thick <110> ZnTe crystal. (b) Image of a symmetric T-shaped structure with w_1 = 100 µm, w2 = 100 µm, $h_1 = h_2$ = 100 µm, g = 200 µm, L = 800 µm and p = 500 µm. (c) Image of a completely asymmetric inverted-L structure with w_1 = 0 µm and w_2 = 200 µm. The other parameters are the same as in (b).

We performed 3D numerical finite-difference time-domain (FDTD) simulations using a commercial software program XFDTD (Remcom Inc.) to model the propagation properties of the different waveguide geometries. The metal was modeled as a perfect electrical conductor. While such an approximation was certainly not strictly valid, it appeared to model the resonance frequencies well, since they were determined by the geometrical parameters of the

device. However, such an assumption underestimated the resonance linewidths, since metal losses were not taken into account. The surrounding dielectric medium was assumed to be air. We used a spatial grid size of 25 μm, which was sufficient to ensure convergence of the numerical calculations, and perfectly matched layer absorbing boundary conditions for all boundaries. For the input electric field, we used a dipole source placed just above the substrate surface with a temporal profile determined by the derivative of a Gaussian pulse that had the same bandwidth (and similar pulse shape) as was available in the experimental work. All simulated results were obtained by recording the field properties at specific spatial points, typically centered on the waveguide (except for y-axis data) in order to match the experimental measurements.

3. Experimental results, simulation and discussion

We begin by first considering the role of symmetry on the guided-wave properties of the devices. In Fig. 2(a), we show the experimentally measured transmission spectra for five separate 7 cm long waveguides, in which the values of w_1 and w_2 were varied, but where $w = w_1 + w_2 = 200$ μm was kept constant. For all five waveguides, the other device parameters – $g = 200$ μm, $h_1 = h_2 = 150$ μm, $p = 500$ μm, $L = 800$ μm – were kept constant. In comparing the spectra, the frequencies associated with the resonance peaks appear to shift slightly relative to one another. However, all of the dips on the high frequency side of the resonance occur at the same frequency, 0.126 THz. This is consistent with our earlier finding that the dips (minima) on the high frequency side of each resonance are the relevant parameter, not the frequencies associated with the resonance peaks [30].

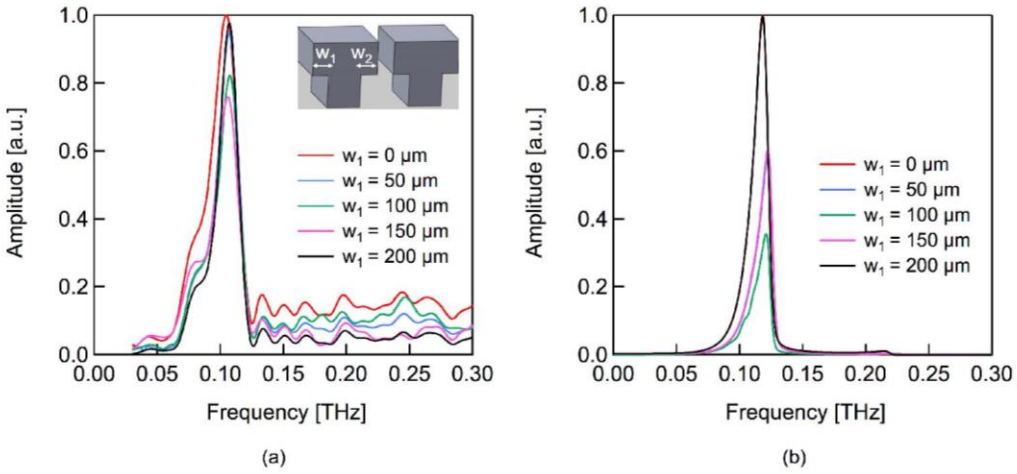

Fig. 2. Experimentally measured and numerically simulated waveguide transmission spectra for 7 cm long devices as a function of asymmetry. In both sets of data, the parameters w_1 and w_2 were varied, while $w = w_1 + w_2 = 200$ μm was kept constant. The other device parameters, $h_1 = h_2 = 150$ μm, $g = 200$ μm, $L = 800$ μm and $p = 500$ μm were also kept constant (a) Experimentally measured spectra. (Inset) Schematic diagram of the T-shaped structures with the relevant parameter shown for both sets of data. (b) Numerically simulated spectra.

In Fig. 2(b), we show the numerically simulated transmission spectra for the exact same waveguide parameters. There are some similarities and differences between these two sets of spectra. First of all, in the numerical simulations, there are no obvious dips on the high frequency side of each resonance. We have previously observed this in simulations related to other guided-wave devices [16]. Nevertheless, the experimentally determined frequencies corresponding to the sharp dips and the frequencies corresponding to extrapolation of the trailing edge of each resonance (0.129 THz) in the simulated data match extremely well. Furthermore, in the simulated data, different waveguide parameters lead to different resonance amplitudes. For example, waveguides with $w_1 = 0$ μm and $w_1 = 200$ μm not only have the highest amplitude, but also have the same amplitude, as would be expected by

symmetry; waveguides with w_1 = 50 μm and w_1 = 150 μm have the next lower amplitude, while devices with w_1 = 100 μm (the symmetric case) have the lowest amplitude. The waveguides with w_1 = 0 μm and w_1 = 200 μm may exhibit the highest amplitudes because they have been predicted to have the highest lateral confinement, which may lead to higher overall confinement [22]. Although there is some variation in the resonance amplitudes in the experimental data, there is no equivalent pattern. Finally, based on the periodicity of the structures, p = 500 μm, the Bragg frequency is given by $\nu_B = c/2p$ = 0.3 THz, where c is the speed of light in vacuum. Any propagating mode with a transverse wave number beyond the first Brillouin zone would exhibit high propagation loss and, therefore, would not be evident in the measured spectral detection window.

Next, we consider the role of structure height in determining the guided-wave properties. In Fig. 3(a), we show the experimentally measured transmission spectra for five separate 7 cm long waveguides, in which the values of h_1 and h_2 were varied, but where $h = h_1 + h_2$ = 400 μm was kept constant. As with the earlier devices, the other parameters – g = 200 μm, $w_1 = w_2$ = 100 μm, p = 500 μm, L = 800 μm – were constant across all five devices. We used a somewhat larger value of h here than was used for the devices in Fig. 1. The primary reason for this was to increase the number of variants (values of h_1) that we could fabricate. Since the symmetric T-shaped structures used here are larger than those used for Fig. 1, the high frequency side minima occurred at a slightly lower frequency, ~0.105 THz. In Fig. 3(b), we show the numerically simulated transmission spectra for the exact same waveguide parameters. Here, the frequencies corresponding to extrapolation of the trailing edge of each resonance in the simulated data occur at ~0.11 THz, which is in good agreement with the experimental data. Finally, we note that the resonance amplitudes are all approximately similar in the simulated spectra, but show somewhat greater variation in the experimental spectra.

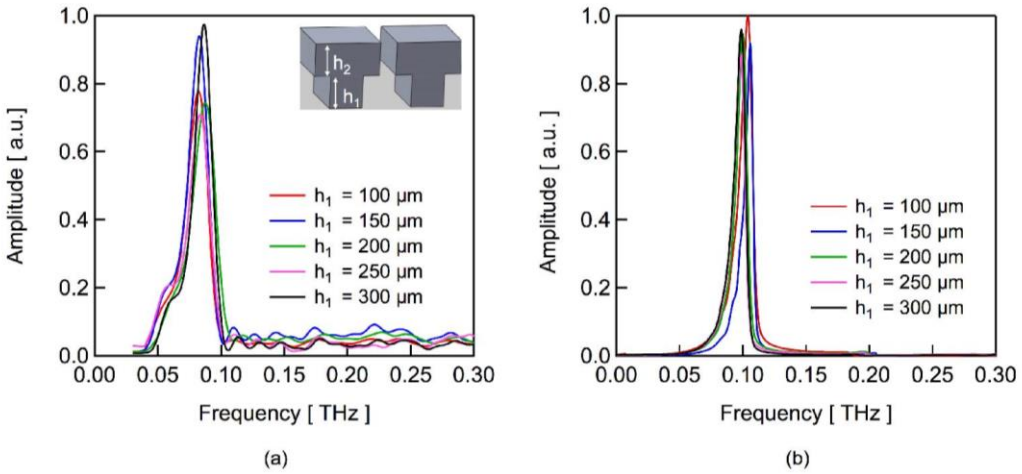

Fig. 3. Experimentally measured and numerically simulated waveguide transmission spectra for 7 cm long devices as a function of asymmetry. In both sets of data, the parameter h_1 was varied, while $h = h_1 + h_2$ = 400 μm was kept constant. The other device parameters, $w_1 = w_2$ = 100 μm (i.e. symmetric T structure), g = 200 μm, L = 800 μm and p = 500 μm were also kept constant (a) Experimentally measured spectra. (Inset) Schematic diagram of the T-shaped structures with the relevant parameter shown for both sets of data. (b) Numerically simulated spectra.

We now consider the role of periodicity in determining the guided-wave transmission properties. In Fig. 4(a), we show the experimentally measured transmission spectra for four separate 7 cm long waveguides, in which the value of p was varied between 500 μm and 800 μm. As with the earlier devices, the other parameters – g = 200 μm, $w_1 = w_2$ = 100 μm, $h_1 = h_2$ = 100 μm and L = 800 μm – were constant across all four devices. In addition, we once again used a different value of h. Aside from the issue of fabricating a wide enough range of

devices (i.e. sufficient variation in a geometrical parameter), using different values of h was necessary to develop a model for the resonance frequencies, as discussed below. Since the symmetric T-shaped structures used here are smaller (lower value of h) than for the waveguides used for Figs. 1 and 2, the high frequency side minima occur at a slightly higher frequency, ~0.165 THz. However, there is some spread in the location of the frequency minimum (~0.008 THz between the four devices). In Fig. 3(b), we show the numerically simulated transmission spectra for the exact same waveguide parameters. Here, the frequencies corresponding to extrapolation of the trailing edge of each resonance in the simulated data occur at ~0.169 THz and, although there is also some variation in this frequency, it is in good agreement with the value found from the experimentally measured spectra. These data demonstrate that the dependence upon the periodicity, p, is weak.

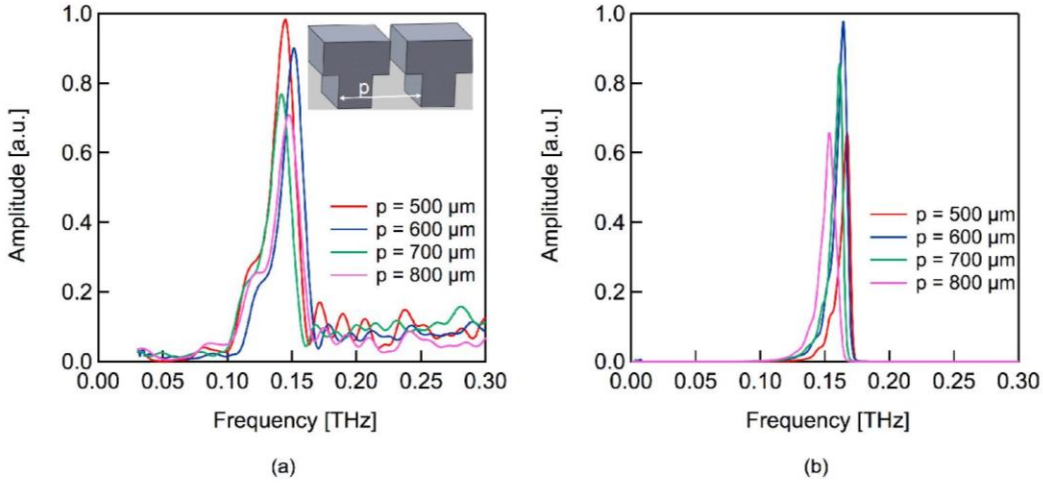

Fig. 4. Experimentally measured and numerically simulated waveguide transmission spectra for 7 cm long devices as a function of the periodicity, p. The other device parameters, $h_1 = h_2 =$ 100 µm, $w_1 = w_2 =$ 100 µm (i.e. symmetric T structure), g = 200 µm, and L = 800 µm were kept constant (a) Experimentally measured spectra. (Inset) Schematic diagram of the T-shaped structures with the relevant parameter shown for both sets of data. (b) Numerically simulated spectra.

Finally, we consider the dependence on L, the structure width. In Fig. 5(a), we show the experimentally measured transmission spectra for four separate 7 cm long waveguides, in which the value of L was varied between 200 µm and 800 µm. As with the earlier devices, the other parameters – g = 200 µm, $w_1 = w_2 =$ 100 µm, $h_1 = h_2 =$ 100 µm and p = 500 µm – were kept constant across all four devices. Here, the values of h, w, g and p are identical to those for the previous set of spectra. We find that the frequency associated with the high frequency side minima all occur at 0.165 THz, with minimal variation. This is consistent with earlier theoretical predictions with so-called domino [20] and inverted-L [22] based waveguides that showed that the transmission spectrum is essentially independent of the lateral width, L. In Fig. 5(b), we show the numerically simulated transmission spectra for the exact same waveguide parameters. Here, the frequencies corresponding to extrapolation of the trailing edge of each resonance in the simulated data occur at ~0.170 THz. Again, we observe excellent agreement between experimental and simulation results.

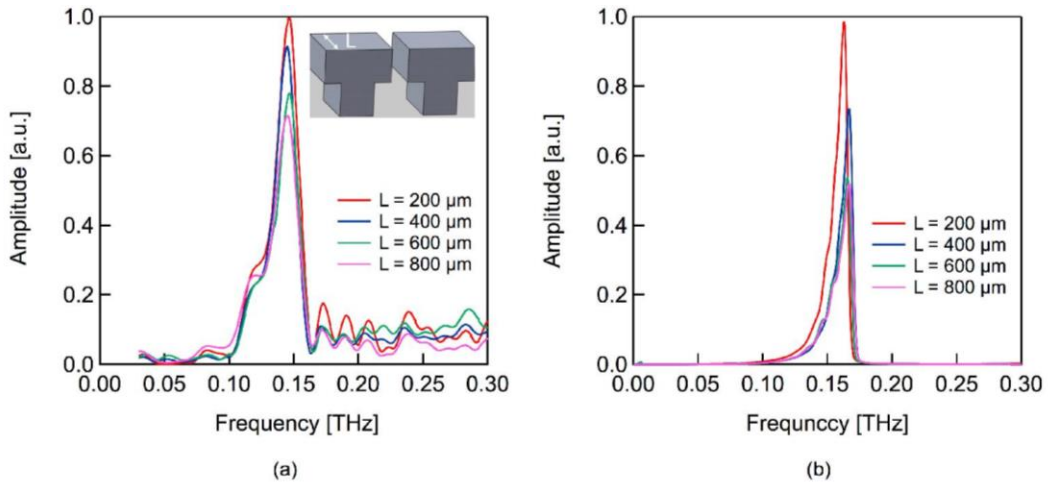

Fig. 5. Experimentally measured and numerically simulated waveguide transmission spectra for 7 cm long devices as a function of the structure width, L. The other device parameters, h_1 = h_2 = 100 µm, w_1 = w_2 = 100 µm (i.e. symmetric T structure), g = 200 µm, and p = 500 µm were kept constant (a) Experimentally measured spectra. (Inset) Schematic diagram of the T-shaped structures with the relevant parameter shown for both sets of data. (b) Numerically simulated spectra.

Given the wide variation in the parameters used to fabricate the waveguides, it is useful at this point to summarize the basic results. In Table 1, we list the device parameters that were varied along with the corresponding frequencies associated with the resonance minima.

Table 1. Waveguide Parameters and Corresponding Resonance Minima Frequencies (g = 200 µm in all cases) from Experimental Results, Simulation Results and the Model (Eq. (1))

Parameter Varied	h_1 (µm)	h_2 (µm)	w_1 (µm)	w_2 (µm)	L (µm)	p (µm)	Exp. ν_m (THz)	Sim. ν_m (THz)	Model ν_m (THz)
w	150	150	0	200	800	500	0.127	0.129	0.133
	150	150	50	150	800	500	0.126	0.129	0.133
	150	150	100	100	800	500	0.126	0.129	0.133
	150	150	150	50	800	500	0.125	0.129	0.133
	150	150	200	0	800	500	0.126	0.129	0.133
h	100	300	100	100	800	500	0.103	0.118	0.111
	150	250	100	100	800	500	0.102	0.112	0.111
	200	200	100	100	800	500	0.108	0.109	0.111
	250	150	100	100	800	500	0.104	0.107	0.111
	300	100	100	100	800	500	0.106	0.107	0.111
p	100	100	100	100	800	500	0.163	0.173	0.167
	100	100	100	100	800	600	0.170	0.171	0.167
	100	100	100	100	800	700	0.161	0.169	0.167
	100	100	100	100	800	800	0.167	0.165	0.167
L	100	100	100	100	200	500	0.165	0.170	0.167
	100	100	100	100	400	500	0.164	0.173	0.167
	100	100	100	100	600	500	0.165	0.172	0.167
	100	100	100	100	800	500	0.165	0.173	0.167

Based on the experimental and simulated resonance minima frequencies, we find that a very simple phenomenological approximation relating the frequency of the transmission minimum on the high frequency side of each resonance with the geometrical parameters of the devices is given by

$$\nu_m \approx \frac{c}{4.5(h+w)}. \quad (1)$$

It is interesting to note that Eq. (1) is approximately similar to that given in [22], where the authors theoretically examined waveguides based on inverted-L structures and found that the resonance frequency was approximately given by $\nu_m \cong c / [4 (h_1 + w + g)]$, using our notation. The sum of the geometrical parameters in this equation is slightly larger than that in Eq. (1) and likely offsets the fact that we use a slightly larger non-integer multiplier in the denominator (4.5 versus 4). Another possible explanation for the use of a non-integer value in Eq. (1) may arise from the fact that the top of the T-shaped structures is open (i.e. there is a gap between structures), while the bottom surface is entirely metalized. We have previously shown that small offsets from integer value indexes were necessary to characterize the resonance properties of waveguides based on blind holes [16,26], which are metalized on the bottom and open on top. The physical basis for this relation arises from the fact that the space between the structures appears to create a groove that has an effective depth given by (h + w), corresponding to a resonance frequency of c/[4.5(h + w)] [22].

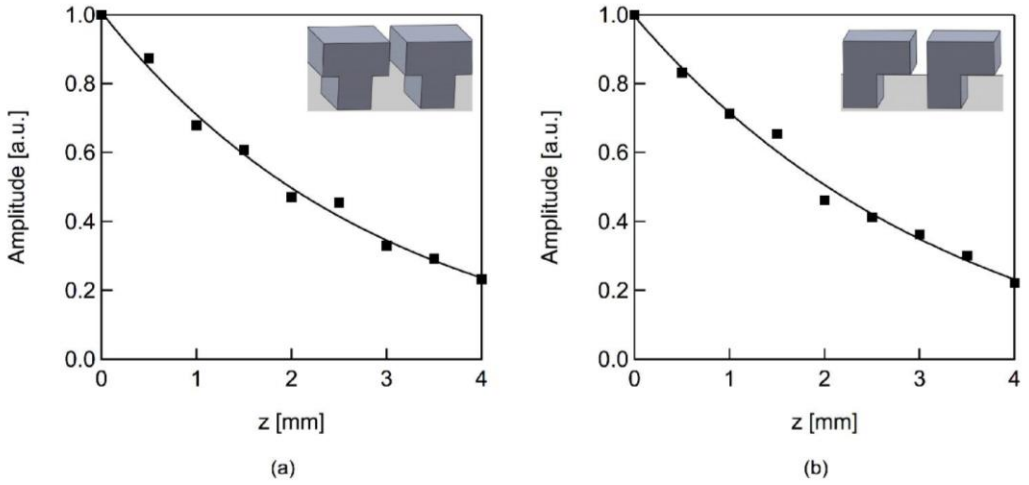

Fig. 6. The $|E_z|$ component of the electric field measured along the z-axis at different heights above the sample surface for the (a) symmetric T-shaped structure: $h_1 = h_2 = 100$ μm, $w_1 = w_2 = 100$ μm, $g = 200$ μm, $L = 800$ μm and $p = 500$ μm (b) asymmetric inverted-L structure: $h_1 = h_2 = 100$ μm, $w_1 = 200$ μm, $w_2 = 0$ μm, $g = 200$ μm, $L = 800$ μm and $p = 500$ μm.

In addition to understanding the guided-wave spectral properties of these devices, it is important to know how tightly bound the propagating wave is along the two transverse dimensions. If we first consider the out-of-plane extent of the bound propagating wave, its spatial properties can be measured by simply moving the optical probe beam along the z-axis and recording the magnitude of the E_z component of the electric field at the resonance peak frequency. In Fig. 6, we show the measured electric field amplitude as a function of distance above the waveguide surface (i.e. along the z-axis) for the symmetric (T-shaped) and completely asymmetric (inverted-L shaped) structures. The 1/e out-of-plane decay length is ~3 mm in the former case and ~3.4 mm in the latter case. Since a number of different waveguide geometries have been investigated experimentally, with different resonance properties, it is useful to compare these values in terms of the corresponding wavelength. Thus, for example, in earlier work for waveguides fabricated using rectangular holes in a thick metal film [12], we found that the 1/e out-of-plane spatial extent was ~1.69 mm at a resonant wavelength of ~1 mm, corresponding to a out-of-plane decay length of ~1.7 λ. For the two waveguides discussed here (Fig. 6), the resonant wavelength is ~1.75 mm and the corresponding out-of-plane decay length is ~1.7 λ (symmetric case) and ~1.9 λ (asymmetric case). Thus, waveguides, based on depressions (holes) and protrusions (T-shaped structures)

appear to behave very much the same in this respect. Next, we consider the propagation properties along the x-axis for the lowest order mode. In Fig. 7, we show the loss properties for propagation along the waveguide for the same two waveguides. An exponential fit to the data for both waveguides yields a loss parameter of ~0.18 cm^{-1}, corresponding to 1/e propagation lengths of ~5.6 (symmetric T) and ~5.5 cm (inverted-L) for the two waveguides. In comparison to the waveguides fabricated in stainless steel [12], where the 1/e propagation length was ~8 cm, the waveguides described here exhibit somewhat greater loss.

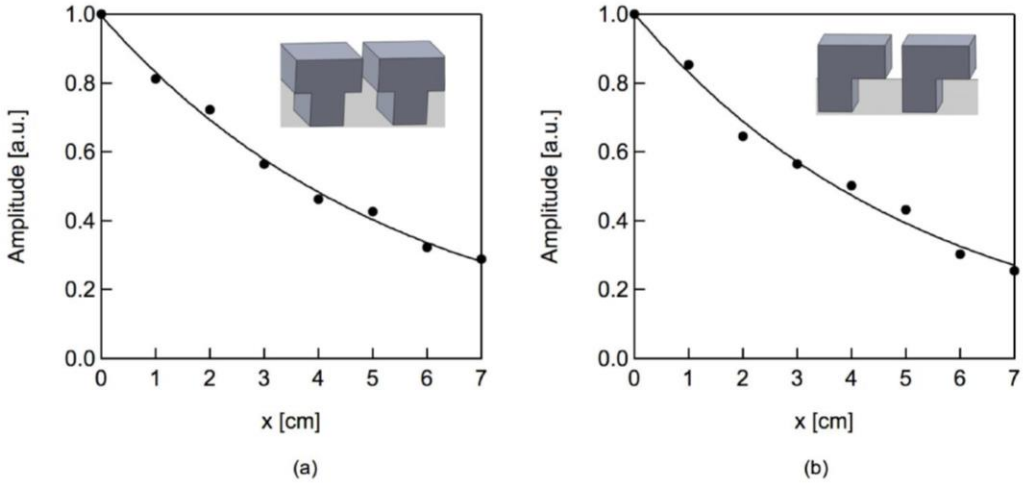

Fig. 7. The $|E_z|$ component of the electric field measured along the x-axis for the (a) symmetric T-shaped structure: $h_1 = h_2 = 100$ µm, $w_1 = w_2 = 100$ µm, $g = 200$ µm, $L = 800$ µm and $p = 500$ µm (b) asymmetric inverted-L structure: $h_1 = h_2 = 100$ µm, $w_1 = 200$ µm, $w_2 = 0$ µm, $g = 200$ µm, $L = 800$ µm and $p = 500$ µm. The 1/e propagation lengths are 5.6 cm for (a) and 5.5 cm for (b).

While the last two sets of data give information about the mode properties, it is helpful if they can be visualized in a slightly different manner. In Figs. 8(a) and 8(b), we show snapshots of the magnitude of the electric field in the xz plane for the symmetric T and asymmetric inverted L based waveguides. In both cases, the measurement was taken at the center (laterally) of the structures, assuming an input frequency that corresponded to the resonance peak for each device. In Figs. 8(c) and 8(d), we show snapshots of the magnitude of the electric field in the xy plane for both waveguides immediately above the upper surface of the structures. It is interesting to note that the field distributions for the two waveguides are similar in nature and the xy distributions look nearly identical, though they exhibit slightly different magnitudes. It is also worth noting that the field decays very rapidly along the y-axis and beyond the structures, for snapshots in Figs. 8(c) and 8(d). While the lateral width of the structures was L = 800 µm for both sets of simulations, we observed nearly identical mode properties as L decreased. This observation, which is consistent with earlier theoretical calculations [22], is the basis for assuming that a tapered waveguide would allow for concentration of the guided-wave mode. Figure 8(e) shows the color coding applied to all four snapshots.

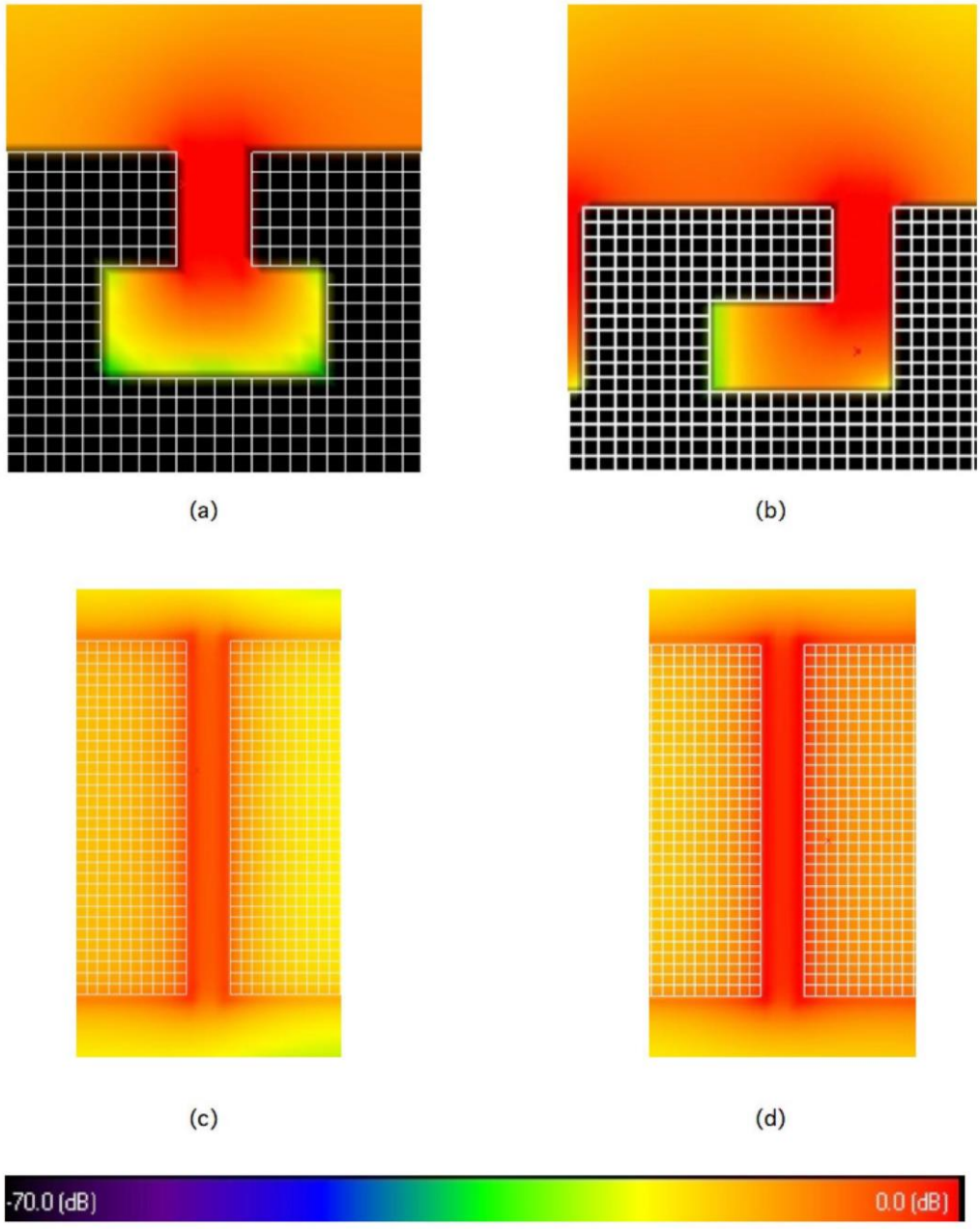

Fig. 8. Snapshots of the magnitude of the electric field for the (a) symmetric T-shaped structures in the xz plane (b) asymmetric inverted L-shaped structures in the xz plane (c) symmetric T-shaped structures in the xy plane immediately above the structure surface (d) asymmetric inverted L-shaped structures in the xy plane immediately above the structure surface (e) Color code that applies to all four snapshots.

With these measurements and simulations in mind, we now address whether or not a tapered waveguide can concentrate the guided-wave mode as well as has been predicted [22]. In order to accomplish this, we need to measure the mode profile along the y-axis of a tapered device. We fabricated a single waveguide in which the width L linearly decreased from L = 800 μm on the input side to L = 100 μm on the output side over a length of 7 cm. Since there appeared to be relatively little variation in the guided-wave properties between devices with different structures (symmetric T to inverted L), we used symmetric T-shaped structures with

$h_1 = h_2 = 100$ μm, $w_1 = w_2 = 100$ μm, $g = 200$ μm and $p = 500$ μm. In Fig. 9(a), we show an image of the laterally tapered device. The corresponding guided-wave transmission spectrum associated with the full device is shown in Fig. 9(b). Although the experimental and simulated resonance peak frequencies do not match, the frequencies associated with the resonance dips are the same and are consistent with the spectra in Fig. 5. In order to measure the guided-wave width, we simply moved the probe beam along the y-axis and recorded the magnitude of the E_z component of the THz electric field at the resonance peak frequency at 4 different positions along the waveguide. These positions corresponded to structure widths of L = 700 μm (1 cm from the input), L = 500 μm (3 cm from the input), L = 300 μm (5 cm from the input), and L = 100 μm (end of waveguide). In Fig. 9(c), we show the measured y-dependence for each of the positions along with a Gaussian fit to the data. The width of the lowest order guided-wave mode, Γ (full-width at half maximum (FWHM) of the fit) is: Γ = 4.8 mm for L = 700 μm, Γ = 4.4 mm for L = 500 μm, Γ = 4.0 mm for L = 300 μm, and Γ = 3.7 mm for L = 100 μm. Thus, for the peak frequency of 0.151 THz (λ = 2 mm), the widths are 2.4 λ (L = 700 μm), 2.2 λ (L = 500 μm), 2 λ (L = 300 μm) and ~1.85 λ (L = 100 μm). Interestingly, Γ does not vary appreciably, even as the structure width is reduced by a factor of 8. If we once again compare to waveguides based on rectangular holes in a thick metal film [12], the FWHM beam width was ~2.2 mm at a resonant wavelength of ~1 mm (corresponding to a FWHM beam width of 2.2 λ). Thus, there appears to be little difference between these different types of waveguides in this regard also. These results are in stark contrast to the theoretical [22] and simulation results. We attribute the wider than expected guided-wave mode width to the fact that real metals exhibit loss. Such losses not only increase the resonance linewidth, but also reduce the level of mode confinement possible in a waveguide. This is consistent with earlier set of waveguides, in which higher losses corresponded to a lower level of confinement for the guided-wave mode [16,26]. Thus, the assumption of lossless metals in theoretical models can lead to significant deviations when considering mode confinement.

(a)

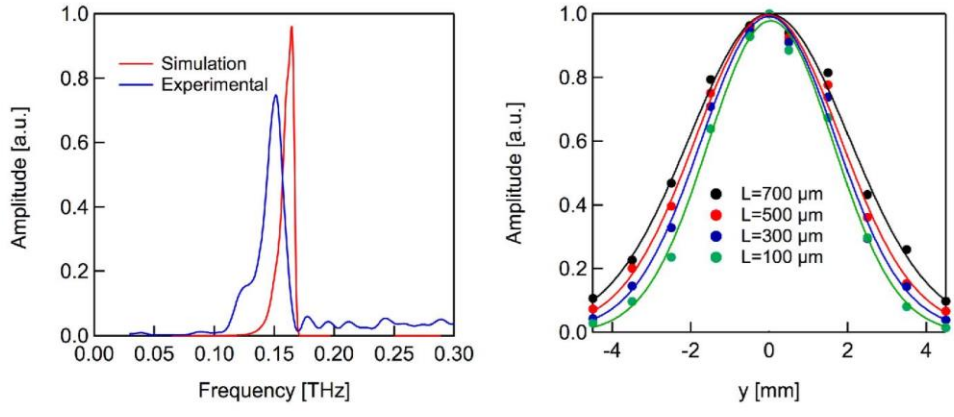

(b) (c)

Fig. 9. Guided-wave properties of a tapered waveguide based on symmetric T-shaped structures. (c) Image of the 7 cm long tapered waveguide with dimensions: $w_1 = w_2 = 100$ μm, $h_1 = h_2 = 100$ μm, $g = 200$ μm and $p = 500$ μm. The lateral width L decreases linearly from L = 800 μm at the input to L = 100 μm at the output. (b) Experimental and numerically simulated guided-wave transmission spectrum. (c) The |Ez| field amplitude measured along the y-axis at four different positions along the waveguide where L = 700μm, L = 500μm, L = 300μm, L = 100μm. y = 0 corresponds to the center of the waveguide. Each of the data sets is fit to a Gaussian function and is color-coded to the data.

4. Conclusion

In conclusion, we have designed, fabricated and characterized THz waveguides based on a one-dimensional array of symmetric and asymmetric T-shaped structures. The devices were fabricated using conventional 3D printing and then sputter coated with ~500 nm of Au. We have measured the guided-wave transmission properties of these devices as a function of the structure asymmetry, height, width and periodicity and found that the frequency of the lowest order resonance was determined primarily by the sum of the height and the length of the overhang ($w_1 + w_2$). However, the resonance properties appear to be independent of the level of asymmetry in the T-shaped structure. We also measured the properties of the lowest order mode along both transverse axes of the waveguide. We found that the 1/e out-of-plane decay length was ~1.8 λ and varied slightly with geometrical changes. Similarly, we found that the mode profile along the y-axis appears Gaussian in shape, as is true of many other waveguide geometries, and has a FWHM width ~2 λ. Finally, we fabricated a tapered waveguide and found that the propagating mode does not become tightly focused, as the structure width becomes much smaller than a wavelength. We attribute this to the fact that metal losses lead to reduced confinement of the guided-wave mode. Aside from the details of the experimental results described here, the excellent agreement between the experimental and simulation results among all of the different devices demonstrates the high level of reproducibility in the 3D printing process for THz device fabrication and suggests exciting new possibilities for device development.

Acknowledgments

This work was supported by the NSF MRSEC program at the University of Utah under grant # DMR 1121252.

CHAPTER 6

BISTABLE PHYSICAL GEOMETRIES FOR TERAHERTZ PLASMONIC STRUCTURES USING SHAPE MEMORY ALLOYS

Reprinted with permission from [Barun Gupta, Shashank Pandey, Anjali Nahata and Ajay Nahata, "Bistable physical geometries for terahertz plasmonic structures using shape memory alloys," Advanced Optical Materials (2017, 1601008).

ADVANCED SCIENCE NEWS
www.advancedsciencenews.com

ADVANCED OPTICAL MATERIALS
www.advopticalmat.de

Bistable Physical Geometries for Terahertz Plasmonic Structures Using Shape Memory Alloys

*Barun Gupta, Shashank Pandey, Anjali Nahata, Ting Zhang, and Ajay Nahata**

Shape memory alloy foils that are appropriately patterned are cycled between two different metal foil geometries resulting in two different terahertz (THz) plasmonic responses. This is accomplished by using patterned foils of a nickel–titanium alloy (Nitinol) that switches between the martensite phase below 31 °C, yielding one physical geometry, and the austenite phase, when the foil is heated above 51 °C, yielding a second physical geometry. In order to enable this reproducible switching, the sample is initially put through a two-way training procedure, through which the two different desired physical geometries are imprinted. Specifically, the metal foils are trained to switch between a sinusoidal corrugation, either 1D or 2D, at close to room temperature and a flat metal sheet above the austenite phase transition temperature. The foils are found to switch reproducibly between geometries over at least 100 thermal cycles. Using THz time-domain spectroscopy, the transmission properties of the foils are measured as a function of incident polarization and foil geometry. The changes in spectrum are explained qualitatively and through numerical simulation.

1. Introduction

Over the last two decades, there has been enormous interest in the field of plasmonics, which involves the excitation and control of surface plasmon-polaritons (SPPs) at metal–dielectric interfaces. By appropriately structuring these metals, a wide range of unique capabilities have been demonstrated, including subwavelength concentration of radiation,[1] enhanced nonlinear optical interactions,[2] and guided-wave propagation.[3] While much of the focus of this topic has been on passive implementations, there is great interest in developing active devices that can modulate or switch the electromagnetic response. Indeed, a wide range of innovative approaches have already been developed utilizing a variety of materials including liquid crystals,[4] semiconductors,[5,6] liquid metals,[7] photochromic[8] and electrochromic[9] molecules, and phase-change materials. Superconductors are one example of phase change materials that are extremely promising.[10] However, a more heavily studied phase change medium for active plasmonic and metamaterial device implementations is vanadium dioxide, VO_2, which undergoes a thermally driven metal–insulator transition near room temperature associated with a structural change in its crystal symmetry.[11,12] The phase transition in these oxides can be extremely fast[13] and has been shown to be induced thermally,[11] optically,[14] and electrically.[15,16]

Phase transitions can lead to a variety of different macroscopic effects, which may be useful for active optical applications. As an example, shape memory alloys (SMAs) can be thermally cycled between different physical geometries.[17] In the case of Nitinol, a nickel–titanium alloy developed at the Naval Ordnance Laboratory, this change has been shown to be associated with a transformation between the martensite phase below the transition temperature and the austenite phase above the transition temperature.[18,19] The two most commonly used approaches to control these transitions are referred to as one-way memory and two-way memory. In the former approach, an SMA that has been deformed returns to its original shape after being heated. This is most commonly demonstrated using wires, though numerous applications utilizing thin metal foils have also been shown. Two-way memory requires that the SMA undergo specific thermomechanical treatments, commonly referred to as training procedures, in order to thermally cycle between two different alloy geometries.[20]

In this submission, we demonstrate that SMAs are an extremely attractive material system for terahertz (THz) plasmonics that allows for switching between different physical geometries corresponding to different electromagnetic responses. We use Nitinol, a metal alloy of nickel and titanium composed of approximately equal atomic percentages, as the SMA medium that is structured to give the desired electromagnetic response. Nitinol has a DC conductivity of $\approx 1.25 \times 10^6$ S m^{-1} for both phases,[21] which is similar to the value for stainless steel, making it well suited for THz plasmonic applications.[22] As an SMA, it undergoes a structural transition between the martensite phase to the austentite phase that is bistable and reproducible at temperatures that are only slightly above room temperature. Using a two-way training protocol that we developed, we created samples that transition between either a 1D or 2D sinusoidally corrugated geometry and a flat substrate. In order to observe a plasmonic response, the foils are patterned either with a periodic array of subwavelength

B. Gupta, S. Pandey, A. Nahata,
T. Zhang, Prof. A. Nahata
Department of Electrical and Computer Engineering
University of Utah
50 S. Central Campus Dr., Salt Lake City, UT 84112, USA
E-mail: nahata@ece.utah.edu

DOI: 10.1002/adom.201601008

ADVANCED OPTICAL MATERIALS
www.advopticalmat.de

ADVANCED SCIENCE NEWS
www.advancedsciencenews.com

apertures or a single aperture and their transmission properties are measured using THz time-domain spectroscopy.

2. Results and Discussion

We used Nitinol foils that were composed of 55.75% nickel and 44.25% titanium as the metallic medium for the THz plasmonic sample. The shape memory effect observed in such alloys exhibit a martensitic (diffusionless) transformation. The crystal structures of the austenitic and martensitic phases are ordered. The martensitic phase is thermoelastic and its formation is crystallographically reversible (i.e., the steps involved in the reversal of martensite plates back to austenite upon heating is the inverse of the formation process and is crystallographically reversible). In **Figure 1**a, we show the small hysteresis in the austenitic/martensite transformation as the sample is cooled and heated. Upon cooling below M_f (martensitic finish temperature), the martensite phase is formed. Deformation by the application of stress results in elastic strain in the martensite phase followed by strain due to reorientation of (martensitic phase) twins, which involves growth of favorably oriented twins at the expense of unfavorably oriented twins. This results in a large shape change. Upon the removal of the stress, the elastic strain is recovered and when heated above A_f (austenitic finish temperature), a reverse transformation to the austenite phase takes place with the material following a crystallographically reversed sequence. Such a reversal is made possible by the ordered structures of parent and product phases. This is referred to as one-way shape memory. After repeating this cycle a certain number of times, commonly referred to as a training procedure, a material shape change can be effected by simply changing the temperature between values below M_f to values above A_f and vice versa. Such a procedure forces the martensitic twin formation, twin reorientation, and reversal processes to take place in a specific reversible sequence, corresponding to two-way shape memory, allowing for switching between two different alloy geometries through thermal cycling.[20]

Two separate sets of sample were used. The first consisted of a 30 cm × 5 cm × 127 µm thick free standing SMA foil used to measure the dielectric constant of the Nitinol. This foil remained flat independent of its temperature. The second set of samples consisted of SMA foils that were perforated with either a periodic array of subwavelength apertures or a single aperture fabricated via laser ablation. These latter samples were then conditioned using a two-way training protocol, as shown schematically in Figure 1b.[20] In this approach, the sample was first heated just above A_f, then cooled below M_f. It was then loaded into a mold with the desired cold state geometry and deformed to conform to the mold with desired geometry. This was followed by the complete removal of applied load. The sample was then heated above A_f. This cycle was repeated 30 times to ensure that the two-way memory effect, shown in Figure 1c, did not decrease with thermal cycling.

The perforated samples were fabricated using 5 cm × 5 cm × 127 µm free standing Nitinol foils that consisted of 300 µm diameter circular apertures periodically spaced by 600 µm on a square lattice. Each sample underwent the same two-way training procedure. At temperatures above 51 °C, the foils were trained to be planar (**Figure 2**a), while at temperatures below 31 °C, the foils were trained to be sinusoidally corrugated with an amplitude of h and periodicity of p (Figure 2b). Different samples were fabricated to

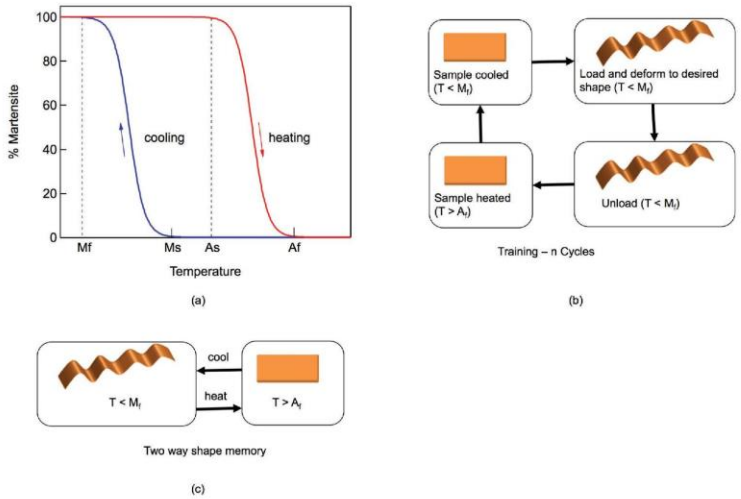

Figure 1. Phase transition properties and two-way training procedure for shape memory alloys. a) Thermal hysteresis in the phase transition properties of Nitinol. b) Schematic diagram showing the two-way training procedure. In this approach, the sample is first heated just above A_f, then cooled below M_f. It is then loaded into a mold with the desired cold state geometry and deformed to conform to the mold with desired geometry. This is followed by the complete removal of applied load. The sample is then heated above A_f. This cycle is repeated 30 times to ensure that the two-way memory effect was fully imprinted. c) Schematic drawing showing thermal cycling between the two physical geometries.

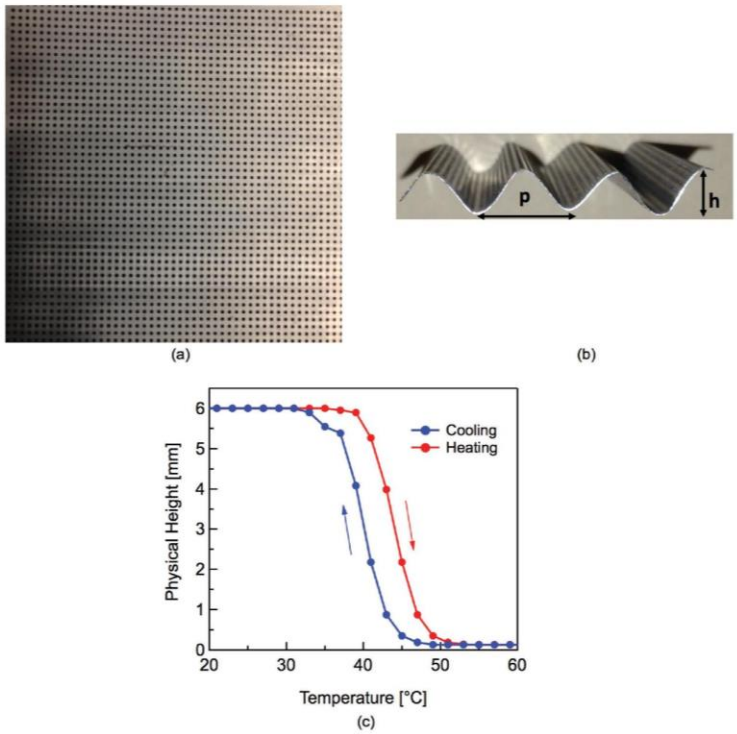

Figure 2. Thermal switching with a 1D corrugation. a) Photograph of hole array aperture fabricated in a 5 cm × 5 cm × 127 µm thick free-standing shape memory alloy (Nitinol) foil when heated above A_f. The circular aperture diameter was 300 µm and the periodicity of 600 µm. b) Side view of the aperture array when cooled below M_f, showing the cross-section of the corrugated sinusoidal structure. h varied from 0.5 to 6 mm, while the periodicity, p, was kept constant at 10 mm. c) Experimentally measured thermal hysteresis in the phase transition properties of Nitinol, where $M_f = 31$ °C and $A_f = 51$ °C (see Figure 1a).

allow for sinusoidal corrugations of different depths (h = 0.5, 2, 3, 4, and 6 mm), though all of the samples were designed to have the same periodicity (p = 10 mm). The measured phase transition properties as a function of temperature for these foils are shown in Figure 2c, which are consistent with the general behavior shown in Figure 1a. For the composition of Nitinol used M_f was 31 °C and A_f was 51 °C.

We used a variation of THz time-domain spectroscopy[23] to measure the THz dielectric properties of the planar Nitinol foil in both the martensite and austenite phases (this foil did not undergo any training procedure and, thus, remained flat over a wide temperature range). The measurement technique is described in detail elsewhere, thus only a brief description is given here. Normally incident broadband THz radiation was coupled to a bound surface propagating waves on the Nitinol foil using a groove fabricated into an adjacent metal slab. Electro-optic sampling was then used to measure the time-domain properties of the surface waves at a variety of different distances and positions along the SMA foil. In **Figure 3**, we show the extracted complex dielectric constants of the Nitinol foil in both the martensite and austenite phases. These values are similar to the measured THz dielectric properties of stainless steel,[23,24] which is consistent with the fact that their DC conductivities are similar. We separately measured the $1/e$ decay length, both along the propagation direction and normal to the metal surface, and found that they are fully self-consistent with predictions based on the dielectric constant measurements (see Supporting Information). Given that this parameter is complex across the THz range of interest here (i.e., it is not a perfect conductor), we utilize an SPP description to analyze the subsequent transmission measurements below, which has previously been used to accurately model the properties of metallic aperture arrays.[22,25,26]

Next, we measured the transmission properties of these structures as a function of both geometry and polarization. In **Figure 4**, we show the terahertz transmission measurement through the perforated structure in both the planar and corrugated geometry as a function of polarization. For the planar geometry (h = 0 mm), obtained for temperatures above 51 °C, the spectrum exhibits three distinct resonances characterized by sharp

ADVANCED OPTICAL MATERIALS
www.advopticalmat.de

ADVANCED SCIENCE NEWS
www.advancedsciencenews.com

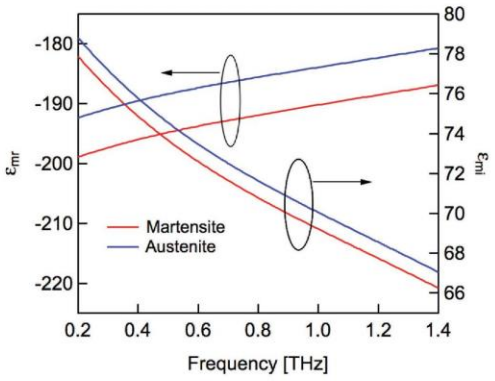

Figure 3. Measured values of the real (ε_{mr}) and imaginary (ε_{mi}) dielectric constants for Nitinol.

dips on the high frequency sides of each resonance, as shown in Figure 4a. These dips occur at 0.50, 0.71, and 1.00 THz, which can be accurately predicted from a commonly used momentum matching condition.[27] We have previously shown that the frequencies resulting from this equation correspond to the resonance dips and not to the resonance peaks.[25] The three lowest order resonances are designated as the (±1, 0), (±1, ±1), and (±2, 0) resonances, respectively, where the integers correspond to Bragg indices.[27] While the location of the frequency dips are determined by the periodicity, the frequency associated with the resonance peak can shift with variations in the aperture diameter or substrate properties.[26] The measured spectrum in this configuration is identical for the orthogonal polarization.

In Figure 4b, we show the spectrum for the corrugated sample for both polarizations, obtained for temperatures below 31 °C, with h = 0.5 mm. Simply by heating or cooling the sample, it is possible to switch between the two physical geometries and obtain their corresponding transmission properties. In order to examine the thermal cycling reproducibility, we first estimate the magnitude of the (±1, 0) resonance amplitude by finding the difference between the peak amplitude of the lowest order resonance and the average high frequency response (slightly beyond 1 THz–not shown). These data are shown for only the polarization perpendicular to the troughs, in Figure 4c, for 100 thermal cycles. It is apparent that there is no significant variation in the THz response over the entire range.

In **Figure 5**, we show the THz transmission properties for all of the different samples (i.e., different values of h) as a function of polarization. In Figure 5a, we show the measured transmission spectra for THz radiation polarized parallel to the troughs. There are several noteworthy points regarding these spectra. First, all of the resonance amplitudes decrease with

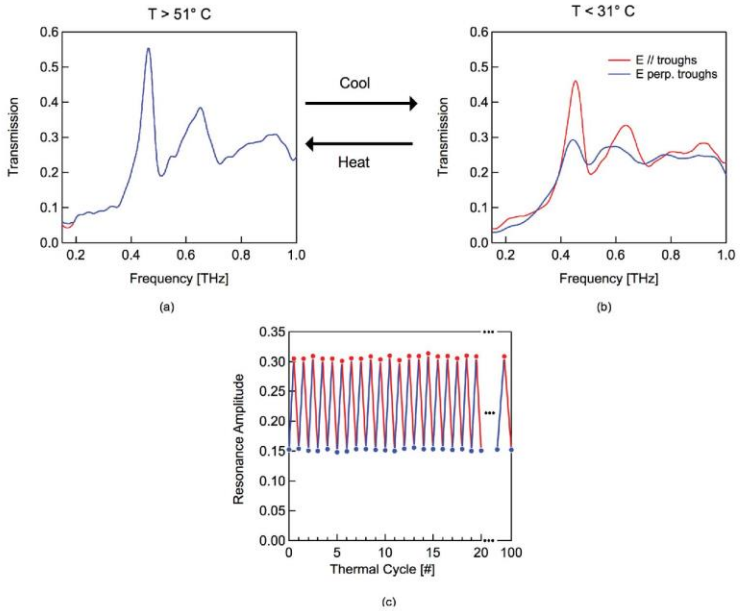

Figure 4. THz transmission properties for the 1D corrugated foil for h = 0 mm and h = 0.5 mm. a) THz transmission spectra measured for incident radiation is polarized parallel to the foil corrugation troughs. The red and blue traces correspond to the two orthogonal polarizations. b) THz transmission spectra measured for incident radiation is parallel and perpendicular to the foil corrugation troughs. e) Amplitude of the lowest order resonance measured for THz radiation polarized perpendicular to the foil corrugation troughs as a function of thermal cycling between h = 0 (T > 51 °C) and h = 0.5 mm (T < 31 °C).

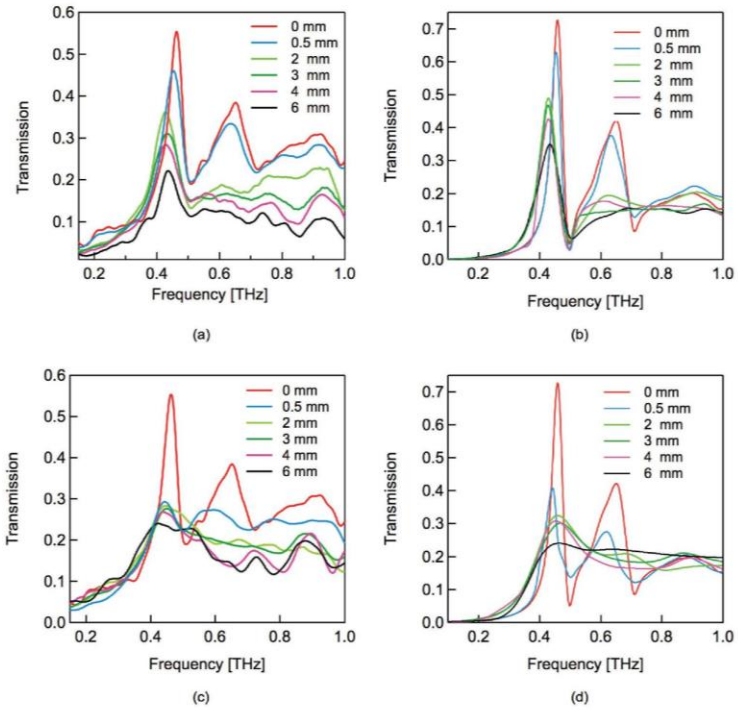

Figure 5. THz transmission properties for the 1D corrugated foil. a) Measured and b) simulated THz transmission spectra for incident radiation polarized parallel to the foil corrugation troughs. c) Measured and d) simulated THz transmission spectra for incident radiation perpendicular to the foil corrugation troughs.

increasing corrugation height. The peak of the lowest order resonance also shifts in frequency slightly with changes in the corrugation amplitude. Finally, the (±1, ±1) resonance effectively disappears for corrugation heights greater than 0.5 mm, while the (±2,0) is evident in all of the samples. The reduction in the resonance amplitudes can be understood by considering the relationship between the indices and the array geometry. The (±1, 0) resonance is associated with SPPs that propagate parallel to the foil troughs and peaks. As the corrugation amplitude increases, we would expect radiative losses for the SPPs to increase somewhat due to the curved nature of the metal foil along the propagation direction. Similarly, the (±2, 0) resonance is associated with SPPs propagating along the same path, so we would expect similar loss characteristics with changes in the corrugation. However, these losses are not expected to be so large as to completely suppress the resonances. On the other hand, the (±1, ±1) resonance is associated with SPPs propagating at 45° with respect to the troughs and peaks for a square lattice. For even relatively small amplitude corrugations, SPPs would experience much higher losses because of the strong bend losses along the propagation path. Thus, this resonance would be expected to be increasingly suppressed with increasing corrugation amplitude, which is consistent with our observations, as shown in Figure 5a.

A full analytical description of the transmission spectra through an aperture array on a corrugated foil would require taking into account that the THz radiation is incident on different apertures at different angles, SPP propagation on curves surfaces, and the diffraction effects of THz radiation transmitted by the array. All of these effects are taken into account in finite-difference time-domain numerical simulations (Lumerical). In Figure 5b, we show the simulated transmission spectra for THz radiation polarized parallel to the troughs, where the dielectric properties of the metal are taken from Figure 3. These spectra reproduce the essential features of the measurements, including the frequency shift in the lowest order resonance peak. It should be noted that the simulated spectra exhibit fewer high frequency oscillations than the measured spectra, especially for samples with larger corrugations. The source of these small oscillations in the measurements is not clear.

In Figure 5c, we show transmission properties for the corrugated aperture array as a function of the corrugation height for THz radiation polarized perpendicular to the corrugation. In contrast to the earlier results, all of the resonances become strongly suppressed for even relatively small corrugation heights. This is because SPPs encounter very few holes along the relevant propagation directions before they become strongly

ADVANCED OPTICAL MATERIALS
www.advopticalmat.de

ADVANCED SCIENCE NEWS
www.advancedsciencenews.com

damped from bending losses. In Figure 5d, we show the corresponding simulated spectra. Once again, the simulations reproduce the essential features of the experimental data. The lowest order resonance is strongly suppressed for corrugation heights of 2 mm or more, while the (±1, ±1) effectively disappears. Interestingly, the (±2, 0) resonance is evident for the $h = 3$ mm and $h = 4$ mm, but not for the $h = 2$ mm and $h = 6$ mm samples. This may be associated with diffraction effects for those specific samples. Here again, the simulated spectra exhibit fewer high frequency oscillations than the measured spectra, especially for samples with larger corrugations.

Up to this point, the corrugation has only been along one dimension. In **Figure 6**, we summarize our results in achieving two-way training for a metal foil that switches between a 2D sinusoidal corrugation at temperatures below 31 °C and a flat foil at temperatures above 51 °C. In Figure 6a, we show an image of the corrugated foil that includes a single 500 µm diameter subwavelength aperture at the center (i.e., a bullseye structure[28]). The corrugation periodicity is 3 mm and the peak-to-peak corrugation height is 200 µm. This corrugation height was chosen based on earlier measurements made with bullseye structures.[29] Using THz time-domain spectroscopy,[30] we measured the transmitted time-domain waveforms in the far-field. When the foil was heated above 51 °C, causing it to become flat, we observed only a single cycle THz pulse in transmission, as shown in Figure 6b. This corresponds to only the incident THz pulse propagating through the aperture. After cooling the sample to room temperature, when the sample switches to the bullseye pattern, the measured THz waveform consists not only of the single cycle pulse, but also 10 time-delayed oscillations (one per corrugation), as is also shown in Figure 6b. We have previously shown that with bullseye samples, the additional oscillations arise because each individual corrugation acts as an excitation site for a THz SPP. The time delay between any individual oscillation and the initial THz pulse is related to both the propagation speed for SPPs at the metal–air interface (approximately the speed of light in vacuum) and the distance between the corrugation and the central aperture. In Figure 6c, we show the corresponding amplitude spectra, consistent with earlier THz measurements using bullseye structures. The resonance peak at 0.1 THz for the bullseye pattern corresponds to the 3 mm corrugation periodicity.

In the present experimental embodiment, thermal switching is accomplished by attaching thin film heaters to the edges

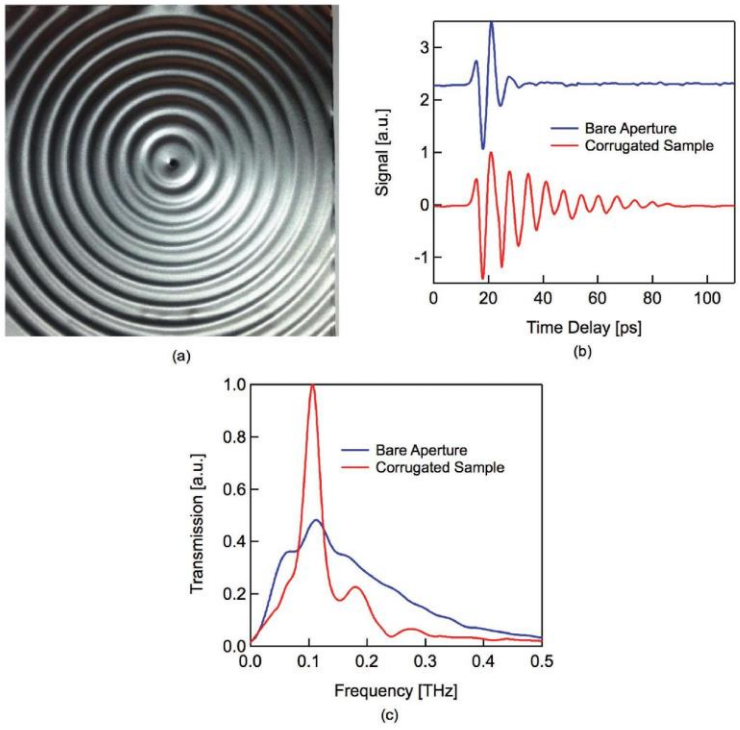

Figure 6. THz transmission properties for the 2D corrugated foil. a) Image of the 2D corrugated sample which resulted when the foil was cooled below 31 °C. b) Time domain waveforms measured for transmission through a bare aperture (blue trace) and the bullseye structure (red trace). c) Amplitude spectra for the two structures using the data in (b).

of the foils, with no active cooling mechanism. Thus, heating the sample by 20 °C (from 31 to 51 °C) can be effected within several seconds, while convection cooling takes considerably longer. It is worth noting that the thermal conductivity of Nitinol is 18 W (m K)$^{-1}$ for the austenite phase and 8.6 W (m K)$^{-1}$ for the martensite phase,[31] while the thermal conductivity of vanadium oxide is only ≈6 W (m K)$^{-1}$.[32] Similarly, the specific heat for Nitinol is 0.83 J (g °C)$^{-1}$,[31] while the specific heat for vanadium oxide is 0.66–0.83 J (g °C)$^{-1}$.[32] Thus, for equivalent samples, we would expect slightly faster switching for Nitinol than for VO_2. Nevertheless, the large thermal mass of the foils leads to the relatively slow switching times. This issue can be improved through the use of thinner films, as has been shown using microelectromechanical systems (MEMS)-based devices in other applications.[33] In such devices, heating times of less than 50 ms have been shown,[34] though sample cooling is still occurred via convection, resulting in slower cooling times.

3. Conclusion

In conclusion, we have demonstrated that shape memory alloys are attractive materials for active THz plasmonic device applications. Using Nitinol, a nickel–titanium alloy, we developed a two-way training procedure that allowed free-standing metal foils to switch between a corrugated geometry at temperatures below 31 °C and a flat geometry at temperatures above 51 °C. This was shown for both 1D and 2D corrugations. By perforating the metal foils with either a single aperture or an array of apertures, we demonstrated switching between two different THz plasmonic responses and discussed why the response changed in the way that it did. Importantly, these switching characteristics have been found to be fully reproducible over at least 100 cycles.

4. Experimental Section

Characterization of Transmission Properties: An amplified ultrafast Ti:sapphire laser was used as the optical source for all of the THz time-domain spectroscopy measurements. The output of the laser was split 80:20 to yield the optical pump and probe beams, respectively. Broadband THz radiation was generated using a 1 mm thick ⟨110⟩ ZnTe crystal. An off-axis paraboloidal mirror was used to collect and collimate the THz radiation as it propagated from the emitter to the sample, resulting in a beam that was normally incident onto the printed sample. A second off-axis paraboloidal mirror was used to refocus the transmitted THz radiation onto a 1 mm thick ⟨110⟩ ZnTe detection crystal, which allowed for coherent detection of the radiation via electro-optic sampling.[35]

Supporting Information

Supporting Information is available from the Wiley Online Library or from the author.

Acknowledgements

This work was supported by the NSF MRSEC program at the University of Utah under Grant No. DMR 1121252.

Received: December 1, 2016
Revised: January 8, 2017
Published online:

[1] J. A. Schuller, E. S. Barnard, W. Cai, Y. C. Jun, J. S. White, M. L. Brongersma, *Nat. Mater.* **2010**, *9*, 193.
[2] M. Kauranen, A. V. Zayats, *Nat. Photonics* **2012**, *6*, 737.
[3] H. A. Atwater, S. Maier, A. Polman, J. A. Dionne, L. Sweatlock, *MRS Bull.* **2005**, *30*, 385.
[4] P. A. Kossyrev, A. Yin, S. G. Cloutier, D. A. Cardimona, D. Huang, P. M. Alsing, J. M. Xu, *Nano Lett.* **2005**, *5*, 1978.
[5] J. G. Rivas, P. H. Bolivar, H. Kurz, *Opt. Lett.* **2004**, *29*, 1680.
[6] J. A. Dionne, K. Diest, L. A. Sweatlock, H. A. Atwater, *Nano Lett.* **2009**, *9*, 897.
[7] J. Wang, S. Liu, Z. V. Vardeny, A. Nahata, *Opt. Express* **2012**, *20*, 2346.
[8] R. A. Pala, K. T. Shimizu, N. A. Melosh, M. L. Brongersma, *Nano Lett.* **2008**, *8*, 1506.
[9] A. Agrawal, C. Susut, G. Stafford, U. Bertocci, B. McMorran, H. J. Lezec, A. A. Talin, *Nano Lett.* **2011**, *11*, 2774.
[10] R. Singh, N. Zheludev, *Nat. Photonics* **2014**, *8*, 679.
[11] F. J. Morin, *Phys. Rev. Lett.* **1959**, *3*, 34.
[12] J. B. Goodenough, *J. Solid State Chem.* **1971**, *3*, 490.
[13] A. Cavalleri, T. Dekorsy, H. H. W. Chong, J. C. Kieffer, R. W. Schoenlein, *Phys. Rev. B* **2004**, *70*, 161102.
[14] A. Cavalleri, C. Tóth, C. W. Siders, J. A. Squier, F. Ráksi, P. Forget, J. C. Kieffer, *Phys. Rev. Lett.* **2001**, *87*, 237401.
[15] G. Stefanovich, A. Pergament, D. Stefanovich, *J. Phys.: Condens. Matter* **2000**, *12*, 8837.
[16] T. Driscoll, H.-T. Kim, B.-G. Chae, B.-J. Kim, Y.-W. Lee, N. M. Jokerst, S. Palit, D. R. Smith, M. D. Ventra, D. N. Basov, *Science* **2009**, *325*, 1518.
[17] *Engineering Aspects of Shape Memory Alloys* (Eds: K. N. Melton, D. Stöckel, C. M. Wayman), Butterworth-Heinemann, Oxford, UK **1990**.
[18] W. J. Buehler, J. V. Gilfrich, R. C. Wiley, *J. Appl. Phys.* **1963**, *34*, 1475.
[19] F. E. Wang, W. J. Buehler, S. J. Pickart, *J. Appl. Phys.* **1965**, *36*, 3232.
[20] H. Y. Luo, E. W. Abel, *Smart Mater. Struct.* **2007**, *16*, 2543.
[21] J. Mohd Jani, M. Leary, A. Subic, M. A. Gibson, *Mater. Design* **2014**, *56*, 1078.
[22] H. Cao, A. Nahata, *Opt. Express* **2004**, *12*, 1004.
[23] S. Pandey, S. Liu, B. Gupta, A. Nahata, *Photonics Res.* **2013**, *1*, 148.
[24] S. Pandey, B. Gupta, A. Chanana, A. Nahata, *Adv. Phys.: X* **2016**, *1*, 176.
[25] T. Matsui, A. Agrawal, A. Nahata, Z. V. Vardeny, *Nature* **2007**, *446*, 517.
[26] A. Agrawal, Z. V. Vardeny, A. Nahata, *Opt. Express* **2008**, *16*, 9601.
[27] T. W. Ebbesen, H. J. Lezec, H. F. Ghaemi, T. Thio, P. A. Wolff, *Nature* **1998**, *391*, 667.
[28] T. Thio, K. M. Pellerin, R. A. Linke, H. J. Lezec, T. W. Ebbesen, *Opt. Lett.* **2001**, *26*, 1972.
[29] A. Agrawal, H. Cao, A. Nahata, *New J. Phys.* **2005**, *7*, 249.
[30] D. Grischkowsky, S. Keiding, M. van Exter, C. Fattinger, *J. Opt. Soc. Am. B* **1990**, *7*, 2006.
[31] C. M. Jackson, R. J. Wasilewski, H. J. Wagner, *55-Nitinol–The Alloy with a Memory: Its Physical Metallurgy, Properties, and Applications: A Report*, Technology Utilization Office, NASA, Washington, DC **1972**.
[32] D.-W. Oh, C. Ko, S. Ramanathan, D. G. Cahill, *Appl. Phys. Lett.* **2010**, *96*, 151906.
[33] P. Krulevitch, A. P. Lee, P. B. Ramsey, J. C. Trevino, J. Hamilton, M. A. Northrup, *J. Microelectromech. Syst.* **1996**, *5*, 270.
[34] D. Grant, V. Hayward, *IEEE Control Syst. Mag.* **1997**, *17*, 80.
[35] A. Nahata, A. S. Weling, T. F. Heinz, *Appl. Phys. Lett.* **1996**, *69*, 2321.

Supplementary Information

Title: Bistable physical geometries for terahertz plasmonic structures using shape memory alloys

*Barun Gupta, Shashank Pandey, Anjali Nahata, Sivaraman Guruswamy, and Ajay Nahata**

I. Background

The dispersion relation for SPP waves propagating along the interface between a planar metal film and a dielectric is given by [S1]

$$k_x = k_{xr} + ik_{xi} = \frac{\omega}{c}\left(\frac{\varepsilon_d \varepsilon_m}{\varepsilon_d + \varepsilon_d}\right)^{1/2} = \frac{\omega}{c} n_{SPP}, \quad (1)$$

where $k_x = k_{xr} + i\, k_{xi}$ is the complex propagation constant of the SPP wave parallel to the propagation direction, ω is the radial frequency of the electromagnetic radiation, c is the speed of light in vacuum, ε_d is the dielectric constant of the dielectric interface medium and ε_m is the dielectric constant of the metal. We assume that ε_d is purely real and that only the metal is characterized by a complex dielectric constant, expressed as $\varepsilon_m = \varepsilon_{mr} + i\, \varepsilon_{mi}$, where ε_{mr} and ε_{mi} are the real and imaginary components of the dielectric constant of the metal, respectively. The complex refractive index associated with the SPP propagation is given by $n_{SPP} = n + i\kappa$.

The electric field associated with SPPs propagating along a smooth surface decreases as $\exp[-k_{xi} x]$. Thus, the 1/e attenuation length, L_x, along the propagation axis is given by

$$L_x = \frac{1}{|k_{xi}|}. \quad (2)$$

The propagation constant along the z-axis within the dielectric medium and can be written as [S1]

$$k_z = k_{zr} + ik_{zi} = \left[\varepsilon_d \left(\frac{\omega}{c} \right)^2 - k_x^2 \right]^{1/2} \quad (3)$$

Here, the attenuation is defined in terms of the electric field decay normal to the surface into the dielectric (□exp[-|k_{zi}| |z|]). Thus the 1/e attenuation length into the dielectric, L_z, can be expressed as

$$L_z = \frac{1}{|k_{zi}|} \quad (4)$$

The exponential decay away from the metal surface arises from the fact that SPPs are electromagnetic waves bound to the metal-dielectric interface and, therefore, take on their maximum amplitude at the interface and decay as one moves away from the surface.

II. Measurement of the Dielectric Properties of Nitinol [S2]

Broadband THz radiation was generated using a 1 mm thick <110> ZnTe crystal and then collected and collimated using an off-axis paraboloidal mirror. The radiation was focused using a 150 mm TPX lens onto a straight 300 μm wide by 100 μm deep rectangular cross-section groove that was 2 cm in length and fabricated in a 400 μm thick stainless steel metal foil. The groove acted as a coupler by scattering a fraction of the incident radiation into SPPs [S3]. This input coupler was physically abutted to the Nitinol foil. The small separation between the two pieces, coupler and sample, had minimal effect on the propagation properties of the coupled SPPs. The time-domain properties of the z-component of the propagating THz electric field were measured using a second <110> ZnTe detection crystal via electro-optic sampling [S4]. The temporal resolution available with our apparatus was 6.66 fs. This crystal could be freely moved about the surface of the sample, as well along the z-axis, allowing for the electric field in the half-space above the metal surface to be completely mapped.

III. SPP Decay Properties

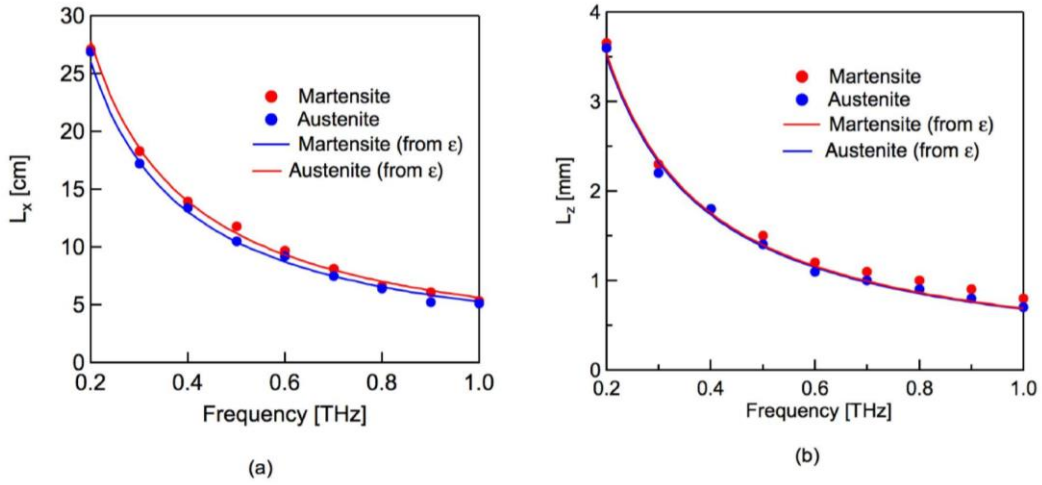

Figure S1. (a) Comparison between the 1/e propagation length along the propagation axis computed from ε_m with $\varepsilon_d = 1$ (solid line) and values obtained by taking measurements along the propagation axis. (b) Comparison between the 1/e decay length along the surface normal computed from ε_m with $\varepsilon_d = 1$ (solid line) and values obtained by taking measurements along the surface normal.

References

[S1] H. Raether, *Surface Plasmons on Smooth and Rough Surfaces and on Gratings*, Springer-Verlag, Berlin, **1988**.

[S2] S. Pandey, S. Liu, B. Gupta, A. Nahata, *Photon. Res.* **2013**, *1*, 148.

[S3] W. Zhu, A. Agrawal, A. Nahata, *Opt. Express* **2008**, *16*, 6216.

[S4] A. Nahata, A. S. Weling, T. F. Heinz, *Appl. Phys. Lett.* **1996**, *69*, 2321.

CHAPTER 7

DIRECT OBSERVATION OF ANDERSON LOCALIZATION IN PLASMONICS TERAHERTZ DEVICES

Reprinted with permission from [Shashank Pandey, Barun Gupta, Sushil Majumdar and Ajay Nahata, “Direct observation of Anderson localization in plasmonic terahertz devices", Light Science and Applications, 2016, DOI: 10.1038/lsa.2016.232.

Direct Observation of Anderson Localization in Plasmonic Terahertz Devices

Shashank Pandey,[1] Barun Gupta,[1] Sushil Mujumdar[2] and Ajay Nahata[1]

[1]*Department of Electrical and Computer Engineering, University of Utah, Salt Lake City, Utah 84112, USA*

[2]*Tata Institute for Fundamental Research, Mumbai, India*

Running title: Localization in Plasmonic Terahertz Devices

Abstract:

We present the first experimental observation of Anderson localization in the terahertz frequency range using plasmonic structures. To accomplish this goal, we designed THz waveguides consisting of a one-dimensional array of rectangular apertures that were fabricated in a freestanding metal foil. Disorder is introduced into the waveguide by offsetting the position of each aperture by a random distance within a prescribed range. For example, for a waveguide with apertures spaced by 250 μm in a periodic waveguide, 10% disorder would correspond to the apertures being shifted by a random value ±25 μm along the waveguide axis. We find that for disorder levels below 25%, there is only an increase in the propagation loss along the device. However, for two specific waveguides with 25% disorder, we observe a spatially localized mode that lies just within the stop band of the device and exhibits a double-sided exponential spatial decay away from the maximum.

Keywords: Anderson localization; disordered medium; time domain spectroscopy; terahertz plasmonics; terahertz waveguides; 1D aperiodic lattice.

Introduction

The Anderson localization of waves is an exotic phenomenon in which a propagating wave is spatially localized purely by structural disorder, thereby inhibiting its transport across the system [1-19]. Although the generality of this wave phenomenon has been proven by its demonstration in acoustic waves [5], matter waves [6] and electromagnetic waves over different frequency ranges [7-17], it has remained elusive in the terahertz domain. Here, we describe the direct observation of Anderson localization in the THz spectral range using THz plasmonic waveguides. These devices are built using periodically spaced structures fabricated into a metal foil, thus allowing surface-bound guided-wave modes below the Bragg frequency. We find that in the presence of appropriate positional disorder, a localized mode beyond the Bragg frequency becomes evident and exhibits a double-sided exponential spatial decay of the THz electric field. These results dramatically expand the spectral range, types of materials and types of applications in which localization may play an important role.

The experimental demonstration of the mesoscopic electromagnetic phenomenon of Anderson localization is known to be challenging, particularly in three-dimensional systems, wherein a critical degree of disorder is required to manifest localization [17]. In lower dimensions, the fact that all states are localized favors the experimental observation of disorder-induced localization, as long as an appropriate sample size is employed [16]. Even in low dimensions, a 'terahertz gap' remains in the literature on localization because dielectric materials, which are commonly

employed in such demonstrations, are lossy in this spectral range [20,21], creating a situation whereby the absorption length may be shorter than the localization length. Metals, by contrast, are characterized by high conductivity and enable the low-loss propagation of surface plasmon polaritons (SPPs) [22-24]. In this study, we employ metal foils that are periodically structured, which have been shown to support the low-loss propagation of narrowband THz guided-wave SPP modes [25-27]. In the simplest embodiment, we have shown that rectangular apertures that fully [25] or partially [27] perforate the metal foil can guide multiple narrowband sets of frequencies. Here, the in-plane length of the aperture orthogonal to the propagation direction determines the frequency of the lowest-order propagation mode, whereas the higher-order modes can be modeled as cavity modes of the aperture, assuming an effective depth [25]. The aperture spacing along the waveguide axis determines the Bragg frequency of the periodic structure, which creates an effective band-edge for the system. Only modes that are characterized by frequencies below the Bragg frequency are observed as propagating modes.

MATERIALS AND METHODS

In this investigation, we examine the guided-wave properties of THz waveguides in which disorder is introduced in the position of the apertures along the propagation direction. The propagating THz electric field is characterized using THz time-domain spectroscopy, which yields both amplitude and phase information. Broadband THz radiation extending from ~0.1 to 1.5 THz is coupled to the waveguide using a single groove etched into the metal foil. The time-domain propagation properties of the coupled THz electric field can be measured at any point on or above the metal surface via electro-optic sampling by simply moving the detection crystal and the optical probe beam [28]. When <110> ZnTe is used as the detection medium, we only

measure the z-component (normal to the metal surface) of the electric field, although other probe beam polarizations and crystal orientations can be used to measure the other electric field vector components [28,29].

In Fig. 1a, we show a schematic of the plasmonic waveguide, in which the apertures are periodically spaced, along with the experimental excitation and measurement geometry. Disorder is introduced into these waveguides by randomly varying the positions of each aperture by a fractional amount, σ, along the propagation direction. For example, in the periodic waveguides discussed below, the aperture spacing was set to 250 μm. Thus, a waveguide with σ = 10% disorder means that each aperture would be shifted by a randomly determined distance of ±25 μm from its original position in the periodic array. A schematic diagram for a waveguide with σ = 25% is shown in Fig. 1b. Because Anderson localization is a stochastic process, we designed eight different waveguide samples for each of nine levels of disorder, σ, varying between 0% and 25%. All of the waveguides were fabricated via laser ablation in 750-μm-thick stainless steel foils. The measured position tolerance for the apertures was less than 5 μm. The THz time-domain signal was initially measured every 5 mm along each waveguide, with smaller measurement increments for the samples that showed evidence of localization. Detailed information about the fabrication of the waveguides and the measurement scheme is presented in the S.I.

RESULTS AND DISCUSSION

Figure 2 presents our measurement of THz wave propagation through the waveguides with varying degrees of disorder. In Fig. 2a, the red profile shows the transmission spectrum

measured at the 8 cm terminus from the waveguide input for the periodic sample. The spectrum illustrates three dominant modes, where the lowest-order mode is determined by the fundamental resonance of the subwavelength aperture, $\nu = c/2s = 0.3$ THz, and the next two higher-order modes are related to Fabry-Perot resonances within the apertures [24]. Transmission through the waveguide arises from coupling of the THz electric field between sub-wavelength apertures. The manifestation of other modes associated with higher-order resonances is forbidden by the band-edge. The corresponding Bragg frequency, in our case, is given by $c/2d = 0.6$ THz, beyond which no transmittance is seen to occur, despite the significant power beyond 0.6 THz in the input pulse shown in S.I. Figure 2(a) also depicts configurationally averaged transmittance spectra for $\sigma = 3\%$ through $\sigma = 25\%$. In these data, the spectrum for $\sigma = 25\%$ is averaged over 6 devices, and the rest are averaged over all 8 devices. These additional spectral measurements demonstrate that the introduction of disorder does not alter the spectral properties of the guided-wave modes for almost all of the waveguides and, in particular, does not necessarily remove the frequency constraints imposed by the Bragg frequency.

For planar (unperforated) stainless steel metal foils, we have previously found that the 1/e THz electric field decay length for SPPs along the surface of the metal is 21 cm at 0.3 THz (12.6 cm at 0.5 THz and 6.3 cm at 1 THz) [24]. Perforating the metal foil to create a waveguide based on periodically spaced apertures creates an additional loss mechanism. In Fig. 2b, we show the magnitude of the THz electric field measured for waveguides with periodically spaced apertures ($\sigma = 0\%$) at the peak of the lowest-order resonance (0.3 THz). The corresponding 1/e propagation length is 8.2 cm, which is still longer than the device length used in this study. Figure 2b also shows the electric field attenuation for two other sets of waveguides with

increased disorder. The corresponding 1/e decay lengths for each value of σ are shown in Fig. 2c, which appears to follow an approximately exponential dependence for reasons hitherto unknown to us. For each waveguide, we can model the amplitude at any given frequency using an exponential decay of the form $E_z(x) = E_o \exp\left[-x / \ell_T\right]$, where x is the coordinate along the length of the waveguide, and ℓ_T is the 1/e decay length. For σ = 25%, ℓ_T for the lowest-order mode corresponds to ~34λ (3.5 cm). Assuming that $\ell_T^{-1} = \ell_{per}^{-1} + \ell_{dis}^{-1}$, where ℓ_{per} is the decay length in a periodic waveguide (8.2 cm) and ℓ_{dis} is the decay length associated with the disorder, we obtain the disorder-induced decay length ℓ_{dis} = 6.1 cm, which is still comparable to the sample length for σ = 25%. If we consider the next two higher-order modes for the same disordered waveguides (σ = 25%), ℓ_T is ~38λ for both resonances at 0.34 THz and 0.49 THz.

As noted above, we only showed the spectra and spatial decay properties for six of the eight waveguides with σ = 25%. The remaining two waveguides exhibited an additional resonance just beyond the Bragg frequency in the effective bandgap region. In Fig. 3a, we show the spectra for one of the two waveguides (because they exhibit very similar spectral properties) as a function of the spatial coordinate. For both of these waveguides, the spectral properties of the three propagating modes are nearly identical to the spectral properties of the other six waveguides with σ = 25%, as are the spatial decay properties for the lowest-order mode. However, the decay properties for the additional mode at ~0.62 THz differ dramatically. In Fig. 3b, we show the spatial properties of this new mode for both waveguides, which is clearly seen to peak in the middle of the samples away from the edges and is strongly localized over approximately 100 apertures. We fit the spatial decay properties of this mode in both waveguides at 0.62 THz to a

double-sided exponential decay of the form $E_z(x) = E_o \exp\left[-\left|x - x_o\right| / \xi\right]$, where x_o is the peak position of the mode and ξ is the 1/e decay length. In both cases, we find that ξ is ~8 mm (~16λ at 0.62 THz), which is much smaller than both ℓ_T and ℓ_{dis}.

The introduction of disorder is known to create new states inside the bandgap. For weak disorder, these states tend to be in close proximity to the band edge, as shown in work involving photonic crystals [11] and slow light [16] waveguides. In the case of photonic crystals, it has been reported that at the band edge, the Bloch wavenumber is given by $k_{Bloch} = 0$; we have shown a similar behavior in the case of plasmonic waveguides [27]. Using the analysis in [19], we find that the product $\Delta k_{Bloch} * \xi \sim 0.83$, which is less than 1 and is a signature of Anderson or strong localization. A detailed explanation of this calculation is given in the S.I. The lowest-frequency resonance inside the bandgap occurs with a resonance peak at ~0.62 THz associated with a TM [201] mode [25], which depends on only the aperture dimensions and not the aperture spacing, which is why the isolated modes in these two waveguides have the same resonance frequency even though they arise from waveguides with different spatial aperture patterns, albeit with identical levels of disorder. By further increasing the level of disorder ($\sigma > 25\%$), it may be possible to realize modes deeper inside the bandgap, corresponding to larger frequencies in the input spectrum.

CONCLUSION

In summary, we have observed clear signatures of strong localization in the THz spectral range by using THz waveguides created by perforating a metal foil and introducing positional disorder into the perforations. In contrast to work performed at optical or microwave frequencies, for

which low-loss materials are readily available, the relative lack of low-loss media in the far-infrared makes such observations challenging. Thus, we only observed localization with a relatively high degree of disorder. We believe that this work will encourage further investigations of localization, both theoretically and experimentally, in regimes where losses are often inherently larger than have been encountered in earlier work (e.g., in the microwave and visible frequency ranges). In such cases, the dissipation length would be an important parameter in the analysis.

ACKNOWLEDGMENTS

This work was supported by the NSF MRSEC program at the University of Utah under grant # DMR 1121252. We thank Shayan Mookherjea and Mikhail Raikh for helpful discussions.

References

1. Anderson PW. Absence of diffusion in certain random lattices. *Phys Rev* 1958; **109**: 1492-1505.
2. John S. Electromagnetic absorption in a disordered medium near a photon mobility edge. *Phys Rev Lett* 1984; **53**: 2169-2172.
3. Pendry JB. Symmetry and transport of waves in one-dimensional disordered systems. *Adv Phys* 1994; **43**: 461-542.
4. Segev M, Silberberg Y, Christodoulides DN. Anderson localization of light. *Nat Photonics* 2013; **7**: 197-204.
5. Weaver RL. Anderson localization of ultrasound. *Wave Motion* 1990; **12**: 129-142.
6. Billy J, Josse V, Zuo ZC, Bernard A, Hambrecht B *et al*. Direct observation of Anderson localization of matter waves in a controlled disorder. *Nature* 2008; **453**: 891-894.
7. Garcia N, Genack AZ. Anomalous photon diffusion at the threshold of the Anderson localization transition. *Phys Rev Lett* 1991; **66**: 1850-1853.
8. Dalichaouch R, Armstrong JP, Schultz S, Platzman PM, McCall SL. Microwave localization by two-dimensional random scattering. *Nature* 1991; **354**: 53-55.
9. Wiersma DS, Bartolini P, Lagendijk A, Righini R. Localization of light in a disordered medium. *Nature* 1997; **390**: 671-673.
10. Grésillon S, Aigouy L, Boccara AC, Rivoal JC, Quelin X *et al*. Experimental observation of localized optical excitations in random metal-dielectric films. *Phys Rev Lett* 1999; **82**: 4520-4523.
11. Topolancik J, Ilic B, Vollmer F. Experimental observation of strong photon localization in disordered photonic crystal waveguides. *Phys Rev Lett* 2007; **99**: 253901.

12. Schwartz T, Bartal G, Fishman S, Segev M. Transport and Anderson localization in disordered two-dimensional photonic lattices. *Nature* 2007; **446**: 52-55.

13. Lahini Y, Avidan A, Pozzi F, Sorel M, Morandotti R *et al*. Anderson localization and nonlinearity in one-dimensional disordered photonic lattices. *Phys Rev Lett* 2008; **100**: 013906.

14. Naether U, Kartashov YV, Vysloukh VA, Nolte S, Tünnermann A *et al*. Observation of the gradual transition from one-dimensional to two-dimensional Anderson localization. *Opt Lett* 2012; **37**: 593-595.

15. García PD, Smolka S, Stobbe S, Lodahl P. Density of states controls Anderson localization in disordered photonic crystal waveguides. *Phys Rev B* 2010; **82**: 165103.

16. Mookherjea S, Park JS, Yang SH, Bandaru PR. Localization in silicon nanophotonic slow-light waveguides. *Nat Photonics* 2008; **2**: 90-93.

17. Strudley T, Zehender T, Blejean C, Bakkers EPAM, Muskens OL. Mesoscopic light transport by very strong collective multiple scattering in nanowire mats. *Nat Photonics* 2013 **7**: 413-418.

18. Bertolotti J, Gottardo S, Wiersma DS, Ghulinyan M, Pavesi L. Optical necklace states in Anderson localized 1D systems. *Phys Rev Lett* 2005; **94**: 113903.

19. Mookherjea S, Ong JR, Luo X, Guo-Qiang L. Electronic control of optical Anderson localization modes. *Nat Nanotech* 2014; **9**: 365-371.

20. Grischkowsky D, Keiding S, van Exter M, Fattinger C. Far-infrared time-domain spectroscopy with terahertz beams of dielectrics and semiconductors. *J Opt Soc Am B* 1990; **7**: 2006-2015.

21. Jin YS, Kim GJ, Jeon SG. Terahertz dielectric properties of polymers. *J Korean Phys Soc* 2006; **49**: 513-517.

22. Wang KL, Mittleman DM. Metal wires for terahertz wave guiding. *Nature* 2004; **432**: 376-379.

23. Jeon TI, Grischkowsky D. THz Zenneck surface wave (THz surface plasmon) propagation on a metal sheet. *Appl Phys Lett* 2006; **88**: 061113.

24. Pandey S, Liu SC, Gupta B, Nahata A. Self-referenced measurements of the dielectric properties of metals using terahertz time-domain spectroscopy via the excitation of surface plasmon-polaritons. *Photonics Res* 2013; **1**: 148-153.

25. Zhu WQ, Agrawal A, Nahata A. Planar plasmonic terahertz guided-wave devices. *Opt Express* 2008; **16**: 6216-6226.

26. Fernández-Domínguez AI, Moreno E, Martin-Moreno L, García-Vidal FJ. Terahertz wedge plasmon polaritons. *Opt Lett* 2009; **34**: 2063-2065.

27. Kumar G, Pandey S, Cui A, Nahata A. Planar plasmonic terahertz waveguides based on periodically corrugated metal films. *New J Phys* 2011; **13**: 033024.

28. Zhu WQ, Nahata A. Electric field vector characterization of terahertz surface plasmons. *Opt Express* 2007; **15**: 5616-5624.

29. van der Valk NCJ, Wenckebach T, Planken PCM. Full mathematical description of electro-optic detection in optically isotropic crystals. *J Opt Soc Am B* 2004; **21**: 622-631.

Figure Captions

Figure 1 | Schematic diagram of the THz waveguide, including the excitation and detection scheme. **a**, Broadband THz radiation is normally incident on a 2-cm-long rectangular cross-section groove, 300 μm wide by 100 μm deep. The groove is used to couple the normally incident freely propagating broadband THz radiation into SPP waves that propagate along the sample surface. The 8 cm long waveguide consists of periodically spaced (σ = 0%) rectangular apertures with the following dimensions: s = 500 μm, a = 150 μm, h = 750 μm and d = 250 μm. A <110> ZnTe crystal that can be freely positioned anywhere above the sample surface is used to measure the z-component of the THz electric field via electro-optic sampling. **b**, Waveguide with identical aperture dimensions and σ = 25%.

Figure 2 | Propagation properties of the waveguides. **a**, Experimentally measured transmission spectra for waveguides with disorder values ranging from σ =0% to σ = 25 % at a distance of 2 cm from the input groove. The spectra are the averages for all eight waveguides at each disorder level, except σ = 25%, where the spectra have been averaged for only six of the eight devices. The dashed vertical line corresponds to the Bragg frequency at 0.6 THz. **b**, Amplitude at the peak of the lowest order resonance (0.28 THz) along the length of the waveguide for σ = 0%, 10% and 25%. The data are averaged as in **a**. The lines show the least squares fits to the data. **c**, The total decay length ℓ_T for the lowest-order mode as a function of σ.

Figure 3 | Spectral and spatial properties for two waveguides with σ = 25%. **a,** Transmission spectra of one of the two waveguides at distances of 2, 4.5 and 8 cm from the start of the

waveguide. **b,** Amplitude at the peak of the mode at ~0.62 THz for both waveguides (red and black dots) measured at 2.5 mm intervals about the maximum. The lines represent the least squares fits to the data for the two waveguides.

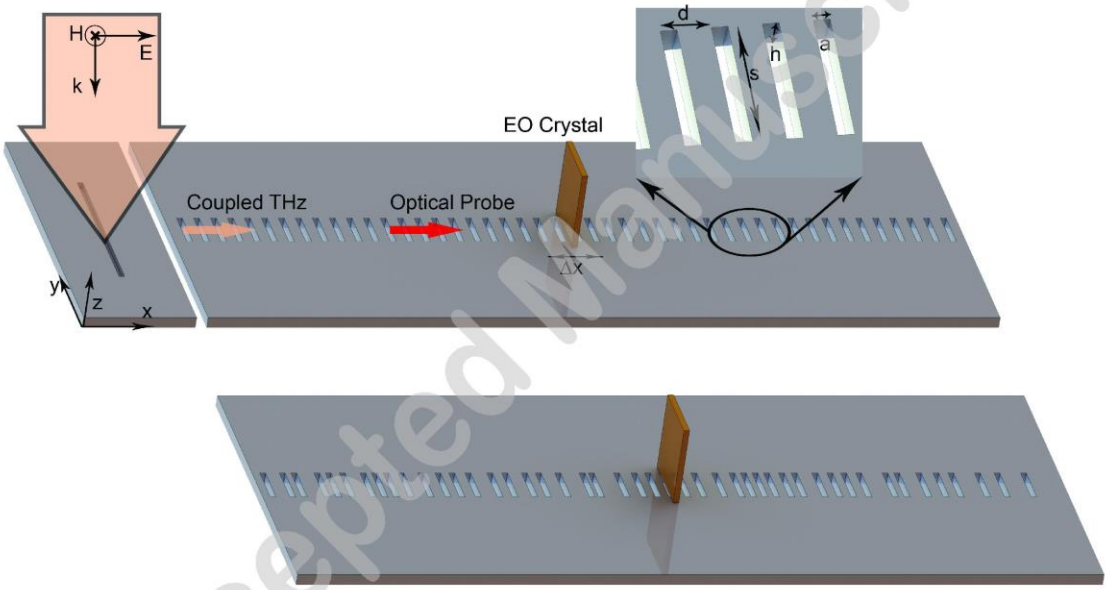

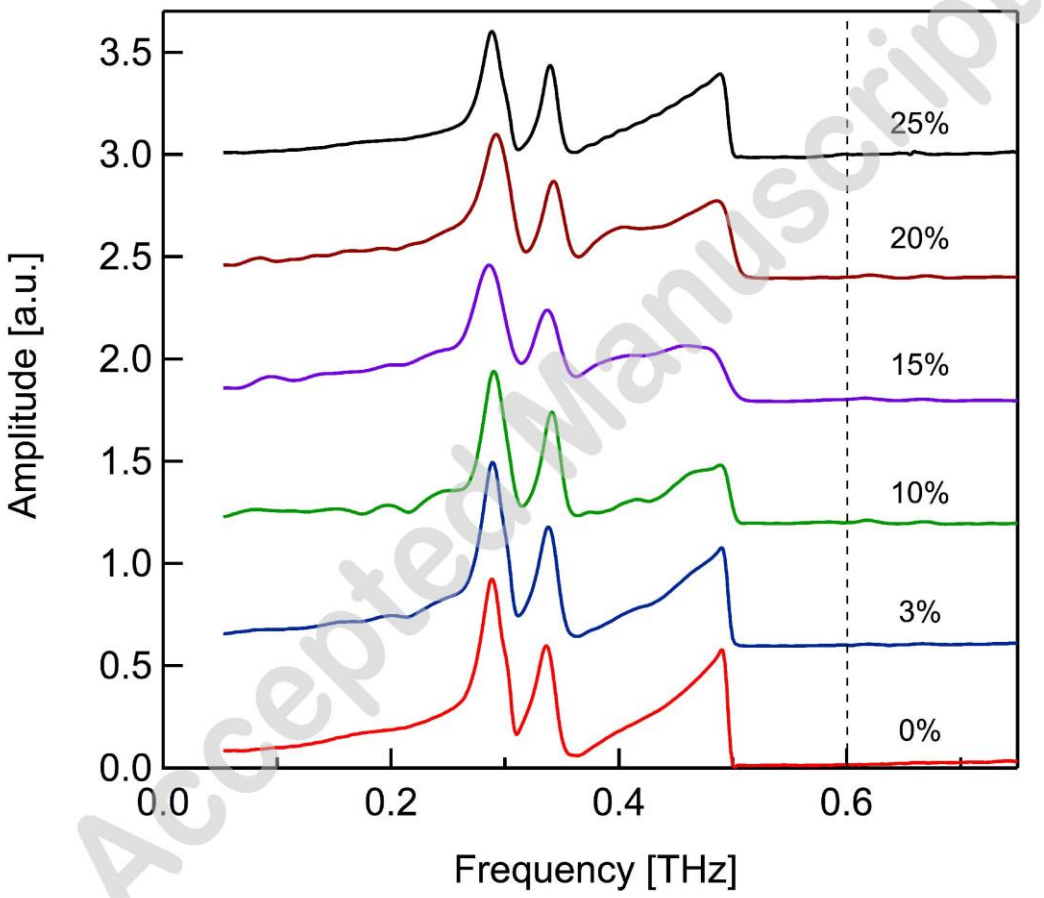

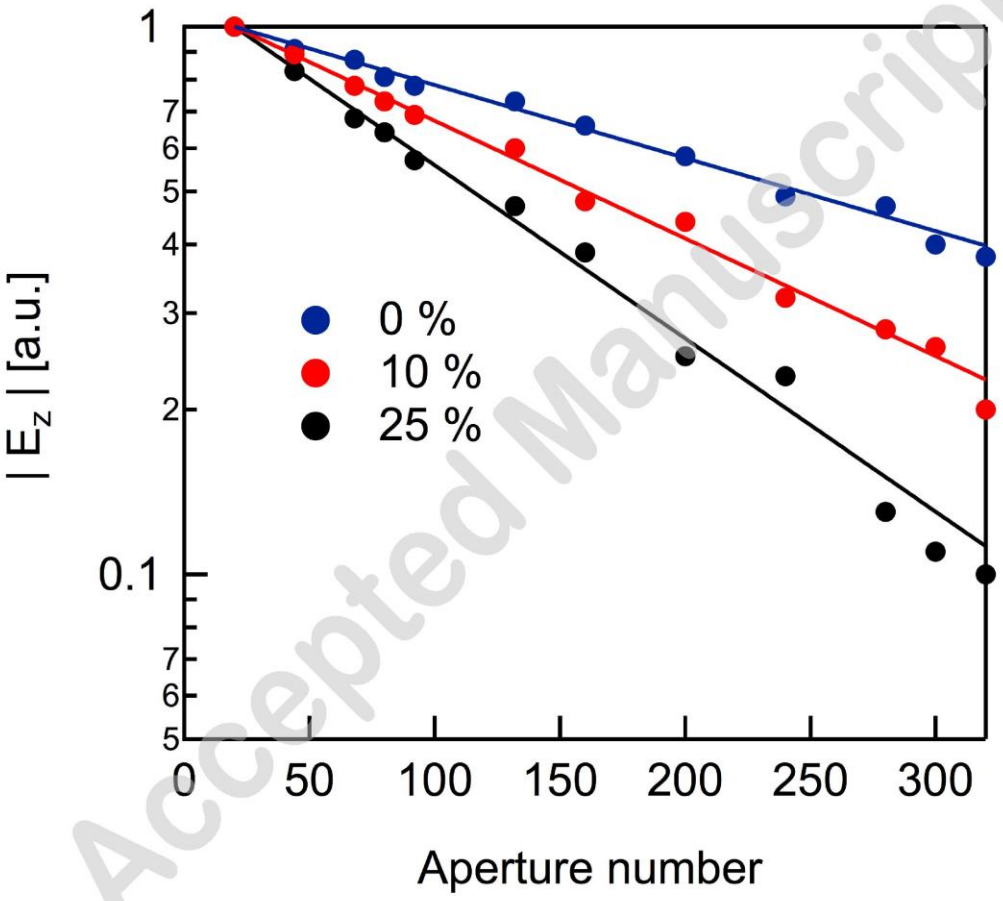

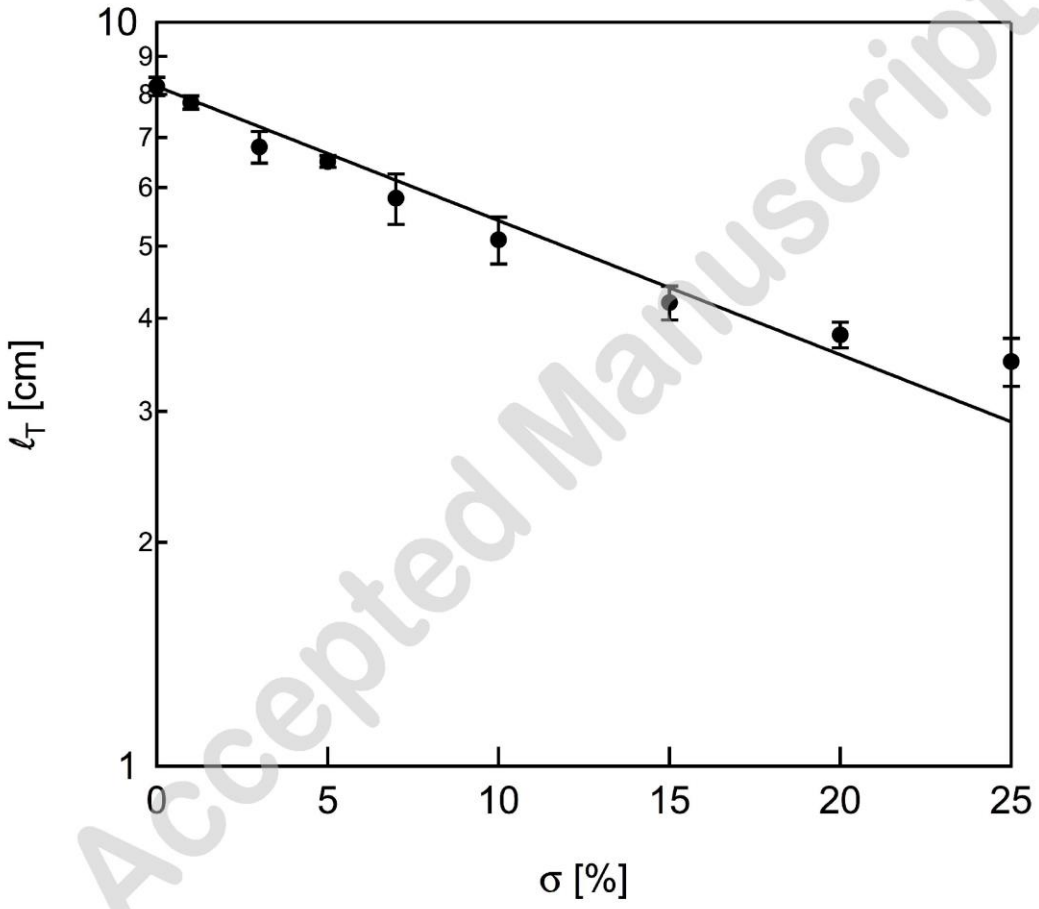

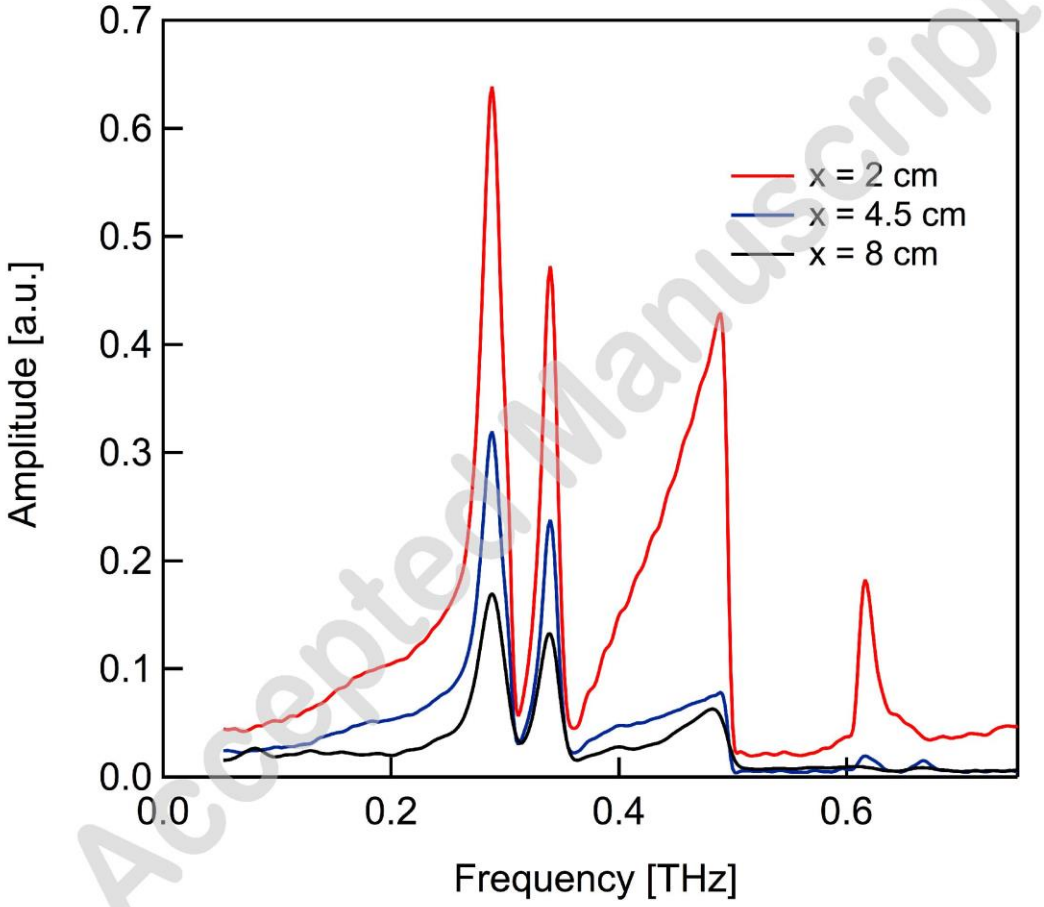

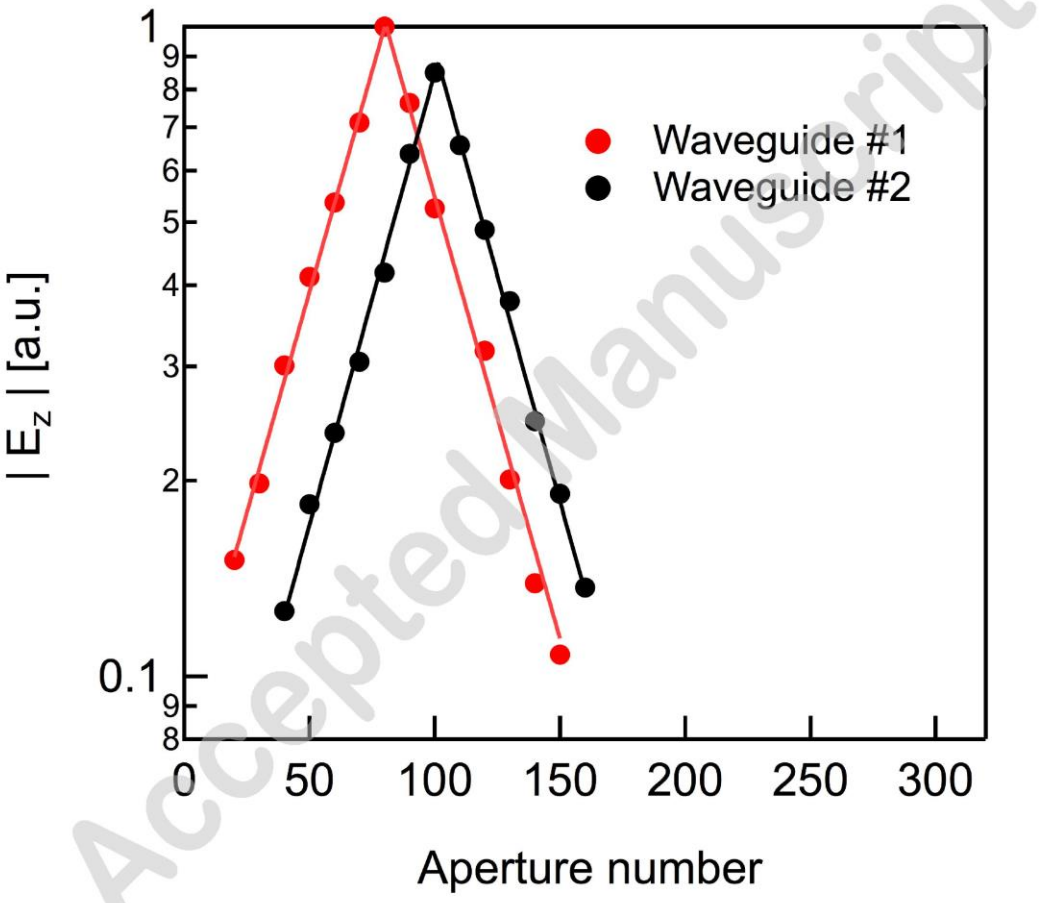

CHAPTER 8

FUTURE WORK AND CONCLUSIONS

8.1 Future Work

8.1.1 Active Terahertz Waveguide Device

So far, all the waveguide devices we have fabricated are either by using laser ablation or by using 3D printing techniques and all are passive devices. The THz plasmonic waveguides that have rectangular aperture allow multiple narrowband propagations. The locations of these multiple narrowbands are completely defined by the geometric parameters of the rectangular aperture. The magnitude of each of the propagating modes can be controlled by placing secondary waveguides next to the main waveguides, as shown in the schematic diagram in Figure 8.1. In order to make it work as an active waveguide, the rectangular apertures of the secondary waveguides are filled with an organic salt- bis2 amine hydrochloride. We measured the refractive index of organic salt at terahertz frequency. The imaginary part of refractive index 'k' gives the loss component increases by 10 factors by a moderate temperate change from 35^0 C to 95^0 C at 0.25 THz. The real part of the refractive index remains constant. In order to control one particular propagating mode, the rectangular aperture length is changed accordingly. For example, in order to suppress the resonant mode at 0.25 THz, the

secondary waveguide optical length is set at 1.6 THz.

8.1.2 Selecting the Transmitted Mode Through the Hole Array

Based on our work on enhanced transmission properties of two-dimensional periodic aperture arrays, we propose to extend the idea of selecting the transmitted mode by introducing the different phase along two directions, as shown in Figure 8.2. The schematic diagram of the proposed future work is shown in Figure 8.2. In this figure, a coupling groove having a width of 100μm and depth of 150μm is structured on a stainless metal film. On each side of the groove, periodic hole array structures are fabricated by laser ablation thickness. The distance between the centers of the groove to the center of the hole on the right side is x_1 and similarly, the distance between the centers of the groove to the center of hole in the left side is x_2. The hole diameter is 500μm and the periodicity is 1mm. The momentum matching condition for the periodic hole array without a groove gives the different resonance modes. The dominant resonance modes are [1, 0] and [1,1] modes that occur at 1mm and 0.42 THz. However, when we introduce the groove, there occurs a time delay between the transmitted THz from the right side of the hole arrays and the left side of the hole arrays. This causes a net phase difference between the transmitted THz signal from the two sides. The phase difference from the two sides can be given by $k \Delta x$.

For the phase difference, $\varphi = k \Delta x = \frac{2 \Pi \ n}{\lambda} \Delta x$. For the constructive interference, $\varphi = 2\Pi m$, where m is an integer. This gives $\Delta x = \frac{m \lambda}{n}$. For the destructive interference, $\varphi = \Pi m$, where m is an integer. This gives $\Delta x = \frac{m \lambda}{2 n}$. These two equations show that for 1mm periodicity, if we choose the path length 0.5 mm, we get destructive interference and

similarly, for the second-order mode, if we choose the path length to be 0.35 mm, we get destructive interference for the second-order mode.

8.1.3 VO_2-Based Active Terahertz Waveguide

Vanadium oxide, VO_2, is a unique complex oxide due to its enhanced electron–electron interaction, which has a major influence on the electric properties. VO_2 exhibits a sharp electronic transition from an insulating state (room temperature) to a metallic state (high temperature). When heated to just above room temperature, the electrical conductivity of vanadium dioxide (VO2) abruptly increases by a factor of 10,000. Using the laser ablation and 3D printing techniques, we have created rectangular aperture waveguides as discussed in Chapter 3 and Chapter 4. In order to make an active terahertz waveguide device, the individual rectangular apertures are filled with vanadium oxide. The entire waveguide is placed on a metal film that can be heated electrically. As we increase the temperature, the propagating mode can be thermally controlled. In fact, we can control from no propagating mode to propagating mode just by thermally heating.

8.2 Conclusions

In Chapter 3, we discussed, terahertz plasmonic structures with spatial variation of conductivity. The spatial variation of conductivity was achieved using a commercially available inkjet printer and using nano-particle inks. The spatial variation of conductivity allowed us to control the propagation properties of surface plasmon. The spatial variation of conductivity was achieved by using a commercially available inkjet printer, in which one cartridge was filled with conductive silver ink and a second cartridge was

filled with resistive carbon ink. In the printed structures, the individual printed dots had differing amounts of the two inks, thereby creating a spatial variation of the conductivity. Using a periodic array of subwavelength apertures as a test structure, patterns printed with fractional amounts of the two exhibited dramatically different enhanced optical transmission properties. These differences appeared due to changes in the propagation loss properties as a function of conductivity. These data were used to design and fabricate aperture arrays in which the conductivity varied spatially. The resulting plasmonic effect was found to dramatically alter the spatial beam profile of the transmitted THz radiation, as measured by THz imaging [1].

In Chapter 4, we discussed the ability to create complex three-dimensional (3D) THz waveguide structures using 3D printing. We demonstrated the complex 3D terahertz waveguide printed with professional-grade 3D printers using Vero White polymer, which was subsequently sputter coated with ~300 nm of gold and acts remarkably well as compared with the standard terahertz waveguide fabricated on stainless steel using the laser ablation technique. We demonstrated the capability of printing 3D terahertz complex waveguides, which was not possible using standard microfabrication technique and inkjet printing techniques [2-3].

In Chapter 5, we discussed a family of symmetric and asymmetric T-shaped structures that acted as a plasmonic THz waveguide and experimentally and numerically investigated the THz propagation properties of those devices. The waveguides were made using a commercially available professional-grade 3D printer (Object EDEN 260V), which had a printing resolution of 600 dpi in the x-y plane and 1600 dpi along the z-axis. The devices were printed using a polymer resin (Vero White) on a support

platform. After the resin solidified, the devices were detached from the support and sputter deposited the device with Au. Sputter deposition typically allows for more film thicknesses on non-planar geometries. In order to help ensure that the bottom surfaces of the T or inverted-L structures were coated with gold, we turned the samples multiple times between deposition runs. On the upper (planar) surfaces of the waveguide, the measured Au film thickness was ~500 nm. Once the deposited Au thickness was more than twice the skin depth, propagating SPP did not see the underlying substrate. Using THz time-domain spectroscopy, we measured the transmission spectrum and other guided-wave properties of the devices as a function of the structure height, lateral width, asymmetry and periodicity. We also performed numerical finite difference time-domain (FDTD) simulations and validated our observations [4-5].

In Chapter 6, we discussed how the shape memory alloys were interesting materials for (THz) plasmonics. We showed that the shape memory alloys are interesting because they allowed for thermal switching between two different physical geometries using only moderate temperature change. In this Chapter, we showed that large (5 cm x 5 cm) foils can be trained to thermally switch between a corrugated geometry (either a 1D corrugation or a 2D corrugation) simply by cycling the temperature over ~20° C range. Those two stable structures that could be thermally switched by using moderate temperatures have significant different plasmonic responses [6-9].

8.3 References

1. B. Gupta, S. Pandey, S. Guruswamy, and A. Nahata, "Terahertz plasmonic structures based on spatially varying conductivities," Advanced Optical Materials, vol. 2, no. 6, pp. 565–571, Jun. 2014.

2. S. Pandey, B. Gupta, and A. Nahata, "Terahertz plasmonic waveguides created via 3D printing," Opt. Express, vol. 21, no. 21, pp. 24422–24430, Oct. 2013.

3. B. Gupta, S. Pandey, and A. Nahata, "Plasmonic waveguides based on symmetric and asymmetric T-shaped structures," Opt. Express, vol. 22, no. 3, pp. 2868–2880, Feb. 2014.

4. S. Pandey, B. Gupta, A. Chanana, and A. Nahata, "Non-Drude like behaviour of metals in the terahertz spectral range," Advances in Physics: X, vol. 1, no. 2, pp. 176–193, Mar. 2016.

5. S. Pandey, S. Liu, B. Gupta, and A. Nahata, "Self-referenced measurements of the dielectric properties of metals using terahertz time-domain spectroscopy via the excitation of surface plasmon-polaritons," Photon. Res., vol. 1, no. 4, pp. 148–153, Dec. 2013.

6. S. Pandey, B. Gupta, B. Cui, D. Schurig, and A. Nahata, "Terahertz waveguide with a negative effective index of refraction measured using time domain techniques," in 2016 41st International Conference on Infrared, Millimeter, and Terahertz waves (IRMMW-THz), 2016, pp. 1–1.

7. B. Gupta, S. Pandey, A. Nahata, T. Zhang, and A. Nahata, "Bistable physical geometries for terahertz plasmonic structures using shape memory alloys," Advanced Optical Materials, Feb. 2017.

8. B. Gupta, S. Pandey, and A. Nahata, "An active terahertz magneto-plasmonic device based on a cobalt aperture array," in 2015 40th International Conference on Infrared, Millimeter, and Terahertz waves (IRMMW-THz), 2015, pp. 1–1.

9. S. Pandey, B. Gupta, S. Mujumdar, and A. Nahata, "Direct observation of Anderson localization in plasmonic terahertz devices," Light Sci Appl., vol. 6, no. 3, p. e16232, Mar. 2017.

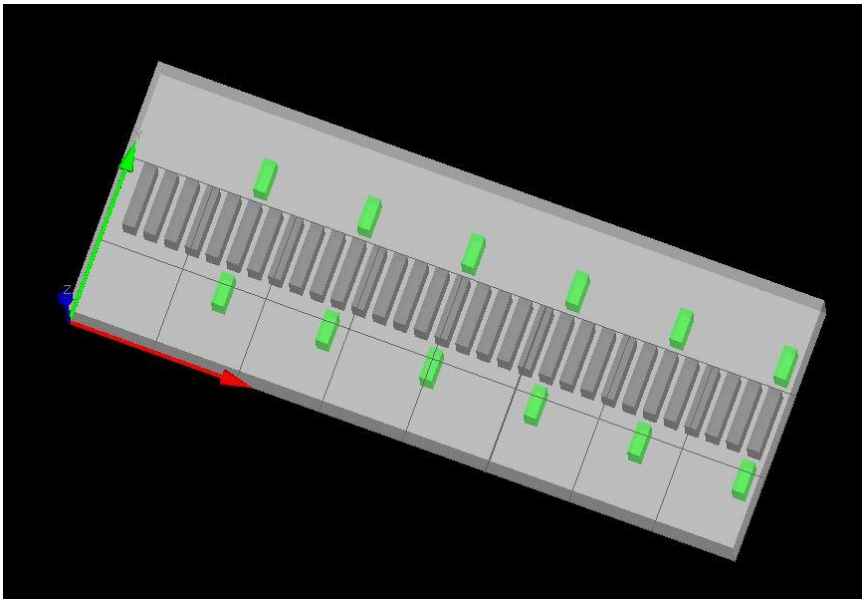

Figure 8.1. A schematic of the waveguide filled with salt. The main axis of the waveguide consists of array of rectangular holes, the adjacent holes next to the main axis of waveguide are leaky resonators, resonance adjusted to account for refractive index of the salt.

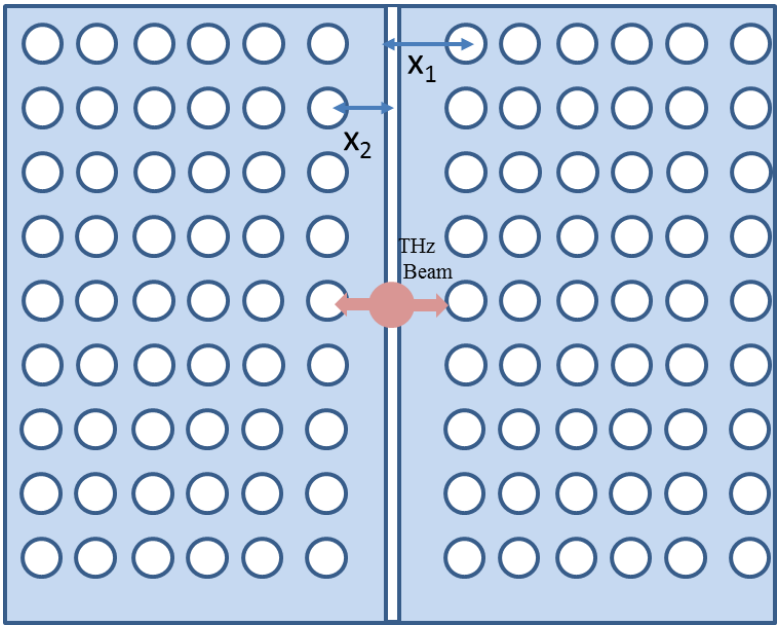

Figure 8.2: Schematic diagram of selecting modes through periodic hole array